Petrological and Geochemical Characterization of Serpentine Muds from Asút Tesoru Seamount (IODP Expedition 366)

Master Thesis

by

Thomas Hilmbauer-Hofmarcher

A thesis submitted in partial fulfillment
of the requirements for the degree of

Master of Science (MSc)

Supervisor

Univ.-Prof. Mag. Dr.rer.nat. Walter Kurz

Institute for Earth Sciences
Karl-Franzens-University Graz

Graz, 2021

Acknowledgements

Abstract

Recovered serpentine muds of Asút Tesoru seamount during IODP Expedition 366 comprise a mélange of serpentine minerals + brucite + magnetite ± iowaite ± andradite ± chlorite ± chromite. The cryptocrystalline serpentine matrix (XMg >0.9) is composed of chrysotile and lizardite. Additionally, summit site material (U1496) contain subordinate mesh-bounded antigorite, implying serpentinization temperatures of at least 300°C. Raman and microprobe analyses revealed that found bastite textures (XMg ~0.83) reflect the primordial pyroxene composition, with elevated Al and Cr concentrations. The occurrence of post-eruptive formed microcrystalline iowaite is bound on the superficial penetration depth of seawater and limited to the flank sites (U1493 to U1495). Occasional Cr zonation patterns and idiomorphic growth of granular andradite (XCa ~0.99) lead to the suggestion of multi-stage formation processes. The most probable reaction path for the initial low-temperature formation of andradite garnets is decarbonization reactions during ascent of the mud mélange, which also could lead to the formation of carbonate chimneys precipitating high-CO_2 fluids observed at Asút Tesoru seamount. It is conceivable that garnet crystal growth resumed after eruption, bound on upwelling hydrothermal fluids with changed chemical composition. Moreover, andradite acts as reliable indicator for low silica activities of the system, underpinned by the observed assemblage andradite + brucite, which suggests serpentinization temperatures below 225°C. The occurrence of magnetite (XMag >0.9) and Ni-alloys is an additional indicator for low silica activities and implies highly reducing conditions. It may be accepted that the secondary formation of magnetite is bound on the extraction from Fe-rich serpentine, following the reaction Fe-serpentine + H_2O = magnetite + $SiO_{2(aq)}$ + H_2. Relict primordial chromite exposes manifold solid solutions, mainly composed of the endmembers chromite (0.30), magnesiochromite (0.27), spinel (0.20, senso stricto), and hercynite (0.17). Signs of disintegration of chromite and zonation patterns in andradite imply a mobilization of Cr in alkaline fluids. Since previous studies (Foustoukos et al., 2011) argued for a temperature (<125°C) and pH (>10) dependency for the dissolution of Cr (Cr(III) to Cr(VI)), a late stage formation of Cr-enriched andradites can be assumed. In general, the mineral assemblage and chemical compositions reflect varying stages of the serpentinization process and the mud evolution, both pre- and post-eruptive. Analyses of major element compositions declare non-fertile mantle as most probable protolith rock, although an isochemical genesis of the mud is very unlikely.

Table of Contents

1. Introduction

1.1 Background

The Izu-Bonin-Mariana arc system represents a tectonic plate boundary, resulting from the subduction of the western Pacific plate under the eastern margin of the Philippine plate (Abers, 1996). Geological processes at the arc system are mainly related to the recycling of oceanic lithosphere in the subduction zone, involving fluid flux, geochemical cycling, tectonic compression and more (e.g. Fryer, 1992; Oakley et al. 2007; Fryer et al., 2017). As one lithospheric plate overrides another in a subduction zone, the material gets progressively altered as a result of increasing temperatures and pressures with increasing depth (Mottl et al., 2004). This leads to a variety of physical and chemical changes of the buried sediment and the oceanic lithosphere, such as compaction, dehydration and prograde metamorphism. As the downgoing plate continues to subduct beneath the forearc, formation water is released through sediment compaction (Hulme et al., 2009). The released aqueous fluids immigrate into the overriding oceanic lithosphere and trigger a partial transformation from mantle peridotite to serpentine mud (Oakley et al., 2007 and references therein). Hence, fluids play a significant role in the transfer of elements through various processes such as dissolution of material in the sediment (Benton et al., 2001), metasomatism and, at later stages, island arc magma generation (Peacock, 1990; Girardeau and Lagabrielle, 1992). With progressing subduction, prograde metamorphism induces the dehydration of clays (Mottl et al., 2004) and mafic minerals within the oceanic crust and contribute additional fluid to the forearc and subarc mantle (Domanik and Holloway, 1996). However, conjugate fractures and faults which penetrate the Mariana forearc provide a pathway for the hydrated mantle material and allows therefore a direct link between the seafloor and the serpentine muds at depth (Fryer, 1992; Fryer et al., 1995, 2006, 2017). This deep-seated gateway enables the fluid and solid reaction products to ascend from the slab (O'Hanley, 1991) and form large serpentine mud volcanoes (Oakley et al., 2007; Chapp et al., 2008). These serpentinite seamounts at the outer part of the Izu-Bonin-Mariana forearc system represent some of the first evidence for the material recycling process that takes place in subduction zones (Oakley et al., 2007). Every seamount in the system show distinctive geochemical fluid signatures, correlating with distance from the Mariana trench and an increasing depth of the subducting slab (Fryer et al., 1999; Mottl et al., 2004; Hulme et al., 2010). The seamounts are mainly composed of compacted and partly lithified serpentine muds with varying amounts of ultramafic and mafic clasts with different serpentinization grades of the matrix (Fryer et al.,

2017), representing forearc and crustal material exhumed from depths greater than 15 to 20 km (Maekawa et al., 1995; Fryer et al., 2000; Gharib, 2006; Hulme et al., 2010, Debret et al., 2018). The process of continuous fluid release with the accompanying progressive serpentinization affects the physical and mechanical properties of the forearc mantle and the subduction channel and it is assumed that the main part of the mineral transformations takes place at the so-called "serpentinization channel" along the slab-wedge boundary (Debret et al., 2018 and references therein). Serpentinites have, in addition, the potential to transport up to 13 wt.% of water in greater depths (100-200 km), where the minerals release the structural integrated water during their transformation to chlorite under prograde metamorphic conditions (e.g. Ulmer and Trommsdorff, 1995; Wunder und Schreyer, 1997). According to this insight, it is widely assumed that the grade of serpentinization of the forearc mantle wedge can exceed 50% (Bostock et al., 2002; Nagaya et al., 2016). However, the rocks involved in the aqueous alteration process of serpentinization are low-silica ultramafic rocks (e.g. harzburgites) which are composed mainly of olivine and pyroxene (e.g. Moody, 1976; Suzuki et al., 2014). The modal minerology of the protolith controls the products of the low temperature metasomatism, which are, in the Izu-Bonin-Mariana arc system, mostly serpentine minerals like chrysotile and lizardite at lower conditions and antigorite at higher conditions (Moody, 1976; O'Hanley, 1991) in conjunction with mainly brucite and minor magnetite (e.g. Janecky and Seyfried, 1986; Frost and Beard, 2007; Fryer et al., 2017). As side products of the serpentinization reaction the mud volcanoes release hydrogen and methane (Fryer et al., 1992; Kelley et al., 2001; Bach et al., 2006) and produce the most reducing, alkaline fluids found in natural environments, with pH values >10 (e.g. Moody, 1976; Fryer, 1992; Frost and Beard, 2007; Wheat et al., 2008; Suzuki et al., 2014). Although peridotite metasomatism seems to be a relatively simple process – it can be described by the $CaO-MgO-FeO-SiO_2$ system – the process of serpentinization is far more complex (Frost and Frost, 2014). For example, given a source of silica, brucite can transform to serpentine (Frost and Beard, 2007) by the following simplified reaction (1):

$$3\ Mg(OH)_2 + SiO_{2(aq)} + 2\ H_2O = Mg_3Si_2O_5(OH)_4$$

<div align="center">Brucite   Serpentine   (1)</div>
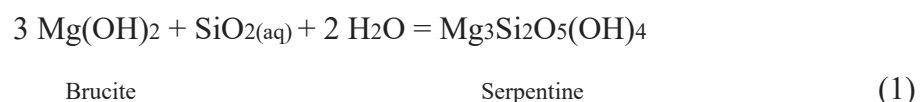
Although the progressive serpentinization of ultramafic rocks produces mainly SiO_2-undersaturated environments (Evans, 2008), the silica required for the reaction can come from

various sources such as alteration of plagioclase (e.g. from associated gabbro) or hydration of clinopyroxenes (e.g. diopside) (Frost and Frost, 2014), shown by reaction (2):

$$3 \ CaMgSi_2O_6 + 5 \ H_2O = Mg_3Si_2O_5(OH)_4 + 4 \ SiO_{2(aq)} + 3 \ Ca(OH)_2$$

Diopside   Serpentine   (2)
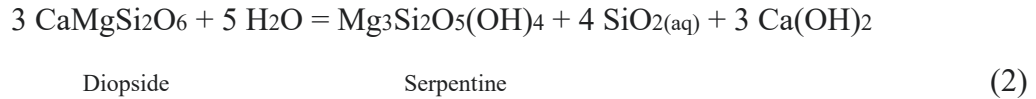
Beside the production of silica, the reaction also produces abundant calcium hydroxide, which is a strong base and a possible explanation why the hydrothermal alteration of peridotite produces highly alkaline fluids (Evans, 2008; Frost and Frost, 2014), although Mottl et al. (2004) observed strong variations in calcium content within the serpentinite mud volcanoes of the Izu-Bonin-Mariana forearc system. Alternative simulations predict that hyper-alkalinity results from OH^- production at decreasing water-rock ratios by olivine and pyroxene dissolution without a consuming reaction while reducing conditions originating in the oxidation of ferrous iron (Fe^{2+}) in minerals with formation of magnetite ($Fe^{2+}Fe_2^{3+}O_4$) (Palandri and Reed, 2003; Frost and Beard, 2007). It is assumed that alkalinity regresses by reaction of upwelling fluids with seawater within a mixing zone, results in precipitation of calcium carbonates, mainly in form of aragonite needles (Mottl, 1992; Mottl et al., 2003, 2004). In active spots where fluids are seeping directly to the seafloor, chimney structures and carbonate encrustations are commonly occurring and are filling many of the numerous cracks and fractures (Fryer, 1992; Ludwig et al., 2006). Hulme et al. (2010) recognized systematic trends in the chemical composition of the upwelling pore waters with evidence for a correlation to increasing temperature and pressure at depth. These trends comprise a constant increase of carbonate alkalinity, Fe, K, sulfate, Na/Cl, B, Mn, Co, Rb, Cs, Gd/Tb, Eu, and light REE and a decrease in Ca, Sr and Y with increasing distance from the subduction front (Hulme et al., 2010). Previous whole-rock geochemical investigations have shown that major elements (except calcium) are not significantly remobilized during the serpentinization of peridotites (Deschamps et al., 2009 and references therein).

This thesis is primary based on the IODP Expedition 366 scientific papers and should continue earlier work on serpentine mud volcanoes with a special focus on the Asút Tesoru seamount. The main goals are a contribution and enhancement of knowledge and deeper understanding of the mineralogical and geochemical transformation processes that take place at the mud volcano.

1.2 The Process of Serpentinization

Serpentinization is the hydrothermal alteration process that occurs when a fluid interacts with olivine and pyroxene-rich ultramafic rocks, typically with peridotites and pyroxenites (e.g. dunite, harzburgite, lherzolite), but also troctolite and picritic basalts to form serpentine minerals (e.g. Moody, 1976; Frost and Beard, 2007; Chavagnac et al., 2013). The most common naturally occurring minerals of the serpentine group are lizardite, chrysotile and antigorite (polymorphic, $Mg_3Si_2O_5(OH)_4$), whose individual formation is mainly controlled by temperature, pressure and water-rock ratio (Wenner and Taylor, 1971,1973; Frost and Beard, 2007). The process of serpentinization from olivine can be described by the idealized reaction (Schwarzenbach et al., 2015):

$$3\ Mg_2SiO_4 + SiO_{2(aq)} + 4\ H_2O = 2\ Mg_3Si_2O_5(OH)_4$$

$$\text{Forsterite} \qquad\qquad\qquad\qquad \text{Serpentine} \qquad\qquad (3)$$
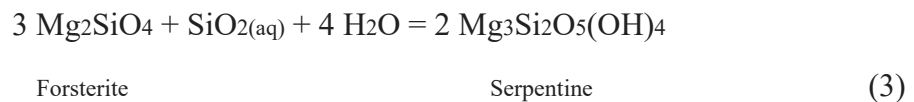
As reaction proceeds, silica activity would rapidly drop in the fluid and facilitate reaction (4) where brucite becomes stable (Frost and Beard, 2007):

$$2\ Mg_2SiO_4 + 3\ H_2O = Mg_3Si_2O_5(OH)_4 + Mg(OH)_2$$

$$\text{Forsterite} \qquad\qquad \text{Serpentine} \qquad\quad \text{Brucite} \qquad\quad (4)$$
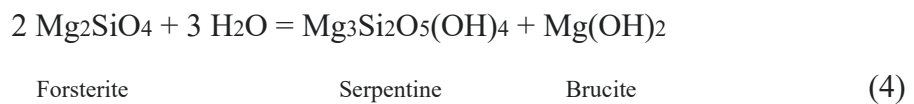
As mentioned in reaction (3) and (4), silica availability is, beside temperature and pressure conditions, a key parameter in the reaction process of serpentinization (Frost and Beard, 2007; Evans, 2008; Chavagnac et al., 2013). The free silica in the system can be provided by the above-mentioned reaction (2) or by silicate dissolution from olivine under essential influence of the aqueous cations hydrogen (H^+) or hydronium (H_3O^+), shown by reaction (5) (Pokrovsky and Schott, 2000):

$$Mg_2SiO_4 + 4\ H^+_{(aq)} = 2\ Mg^{2+}_{(aq)} + SiO_{2(aq)} + 2\ H_2O$$

$$\text{Forsterite} \qquad\qquad\qquad\qquad \text{Fluid} \qquad\qquad\quad (5)$$
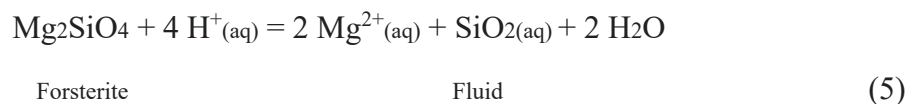
However, because of the large amount of water necessary in reaction (3) and (4), water-rock ratio can drop dramatically, and the hydrothermal environment favors alternative reaction paths which incidentally increase the pH of the remaining fluid (Palandri and Reed, 2003):

$$Mg_2SiO_4 + 2\ H_2O = 2\ Mg^{2+}_{(aq)} + SiO_{2(aq)} + 4\ OH^-$$

Forsterite   Fluid   (6)

$$MgSiO_3 + H_2O = Mg^{2+}_{(aq)} + SiO_{2(aq)} + 2\ OH^-$$

Enstatite   Fluid   (7)
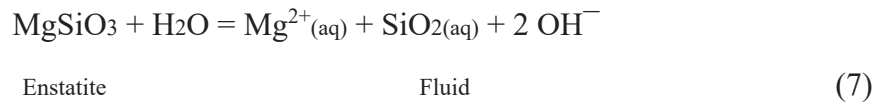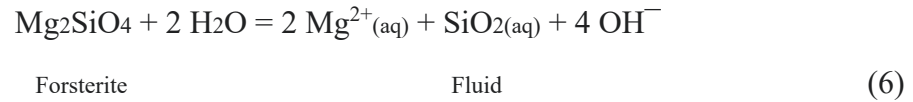
The released Mg^{2+} and OH^- from dissolution of mafic minerals can be removed by brucite precipitation, buffering the pH at around 10 and also the concentration of magnesium (Palandri and Reed, 2003), as showed by the following idealized reaction (8):

$$Mg^{2+}_{(aq)} + 2\ OH^- \rightarrow Mg(OH)_2$$

Fluid   Brucite   (8)

Hence, the equilibrium formation of brucite is mainly driven by a low silica activity and increased pH due to a low water-rock ratio, caused by a reduced fluid flux (Palandri and Reed, 2003; Frost and Beard, 2007; Frost et al., 2013). If brucite is formed during hydrothermal alteration of ultramafic rocks, the minerals contain significant quantities of iron (Moody, 1976; Sleep et al., 2004; Bach et al., 2006).

It is assumed that the hydrothermal transformation of mafic minerals to serpentine and ferroan brucite at low water-rock ratio is followed by more open-system conditions with an increased fluid flux and higher silica activities, triggering the formation of magnetite by the breakdown of ferroan brucite (reaction (9)) (Bach et al., 2006) or, less common, the oxidation of the iron component in serpentine (Reaction (10), (Frost and Beard, 2007):

$$57\ Mg_{0.75}Fe_{0.25}(OH)_2 + 30\ SiO_{2(aq)} = 15\ Mg_{2.85}Fe_{0.15}Si_2O_5(OH)_4 + 4\ Fe_3O_4 + 23\ H_2O + 4\ H_2$$

Fe-Brucite   Serpentinite   Magnetite   (9)

$$2 \ Fe_3Si_2O_5(OH)_4 + O_2 = 2 \ Fe_3O_4 + 4 \ SiO_{2(aq)} + 4 \ H_2O$$

Serpentine   Magnetite   (10)
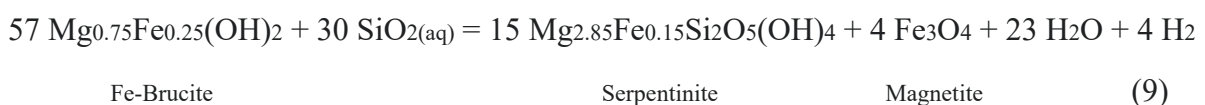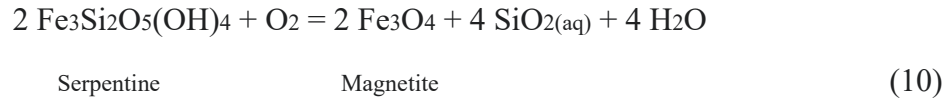
There are much more theoretical reaction paths for magnetite formation during the hydration of peridotites but the studies of Toft et al. (1990) revealed decoupled multi-stage serpentinization processes and showed that an early formation of magnetite is highly improbable. Further investigations with natural remanent magnetizations unveiled that the iron content of serpentine minerals decreases, and the formation of secondary magnetite increases with progressive serpentinization and ascends rapidly if 75% of the ultramafic rock is serpentinized (Oufi et al., 2002). The observations correspond with reported mesh rims from pseudomorphs after olivine which contain rather serpentine and ferrous brucite than magnetite, whereas the cores contain serpentine, magnesian brucite and magnetite (Bach et al., 2006). The production of hydrogen during serpentinization is coupled to the formation of magnetite, whereby the oxygen necessary for the process is extracted from decomposition of water (as shown in reaction (9)), which makes serpentinites among experts to the most reducing environments on Earth (e.g. Bach et al., 2006; Frost and Beard, 2007; Evans, 2008; Frost and Frost, 2014).

Beside reactions (6) and (7), an additional source of OH^- ions can be provided by the dissolution of the CaO component from protolith minerals (e.g. diopside, $CaMgSi_2O_6$) most likely linked to reaction (2) (Palandri and Reed, 2003; Suzuki et al., 2014):

$$CaO + 2 \ H_2O = Ca^{2+}_{(aq)} + 2 \ OH^-$$

(11)

The resulting high pH and Ca^{2+} concentration of the fluid makes calcite quite insoluble and tend to precipitate if enough CO_2 (as bicarbonate, HCO_3^-) is in the system, or alternatively Ca^{2+} is removed by upwelling fluids which can lead to the observed calcite chimneys at hydrothermal vents when mixing with cold seawater (Kelley et al., 2001). Calculations by Frost and Beard (2007) showed a strong dependency of temperature and low silica activity for the breakdown of clinopyroxenes due to the destabilization by hydrothermal fluids at decreasing temperatures. A low silica activity can be preserved by the buffering reaction (12), which forms serpentine from brucite with aqueous SiO_2 (Frost and Beard, 2007):

$$Mg_3Si_2O_5(OH)_4 + H_2O = 3\ Mg(OH)_2 + 2\ SiO_{2(aq)}$$

Serpentine   Brucite   (12)
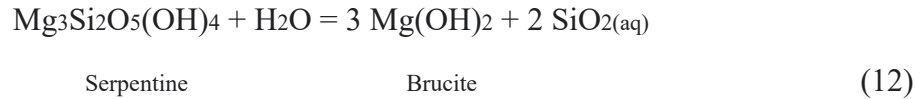
This buffering reaction causes such a low activity of aqueous silica that magnetite remains as the most stable mineral phase for iron at low temperatures (Palandri and Reed, 2003). Hematite crystallization as stable Fe-phase is reported in the upper part of serpentinite structures, reflecting the mixture of upwelling serpentinization fluids with seawater (Beard and Hopkinson, 2000).

Andradite is another serpentine-related mineral which is interpreted as a major sink for iron (Beard and Hopkinson, 2000) and calcium at low temperatures (Frost, 1985). Furthermore, andradite is a reliable indicator for low silica activities, due to its sensibility to the very same (Frost, 1985; Frost and Beard, 2007). As suggested by Taylor and Liou (1978), andradite is stable at low temperatures and pressures, if X_{CO2} remains high enough. Additionally, the garnets can show an increasing substitution of Fe^{2+} for Ca^{2+}, increasing the stability toward higher temperatures.

If andradite is abundant in bastite, it is evident that, combined with the presence of a reactive fluid (Taylor and Liou, 1978), the breakdown of clinopyroxene can lead to andradite, expressed as reaction (13) (Frost and Beard, 2007):

$$12\ CaMgSi_2O_6 + 3\ Fe_3O_4 + 8\ H_2O = 4\ Ca_3Fe_2Si_3O_{12} + 4\ Mg_3Si_2O_5(OH)_4 + Fe + 4\ SiO_{2(aq)}$$

Diopside   Magnetite   Andradite   Serpentine   (13)
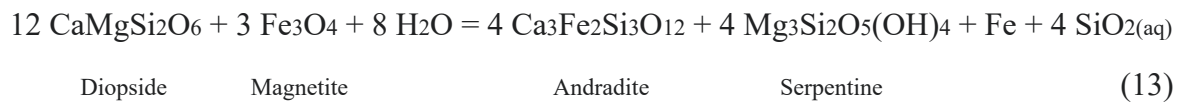
Another probable reaction path for the low temperature formation of andradite are decarbonization reactions, which signify very CO_2-rich fluids (Taylor and Liou, 1978):

$$9\ CaCO_3 + 2\ Fe_3O_4 + 9\ SiO_{2(aq)} + 0.5\ O_2 = 3\ Ca_3Fe_2Si_3O_{12} + 9\ CO_2$$

Calcite   Magnetite   Andradite   (14)
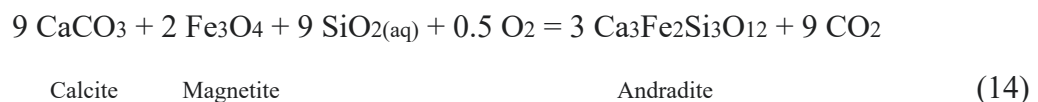
2. Location and Geological Setting

2.1 Geographic Position

The Izu-Bonin-Mariana arc system is located in the western Pacific ocean and represents an intra-oceanic convergent plate boundary (Fryer, 1996; Stern et al., 2001), ranging from Tokyo, Japan over 3,100 km southwards to the Republic of Palau and comprises the eponymous Izu and Bonin Islands, the Mariana Islands and Guam (see Fig. 1).
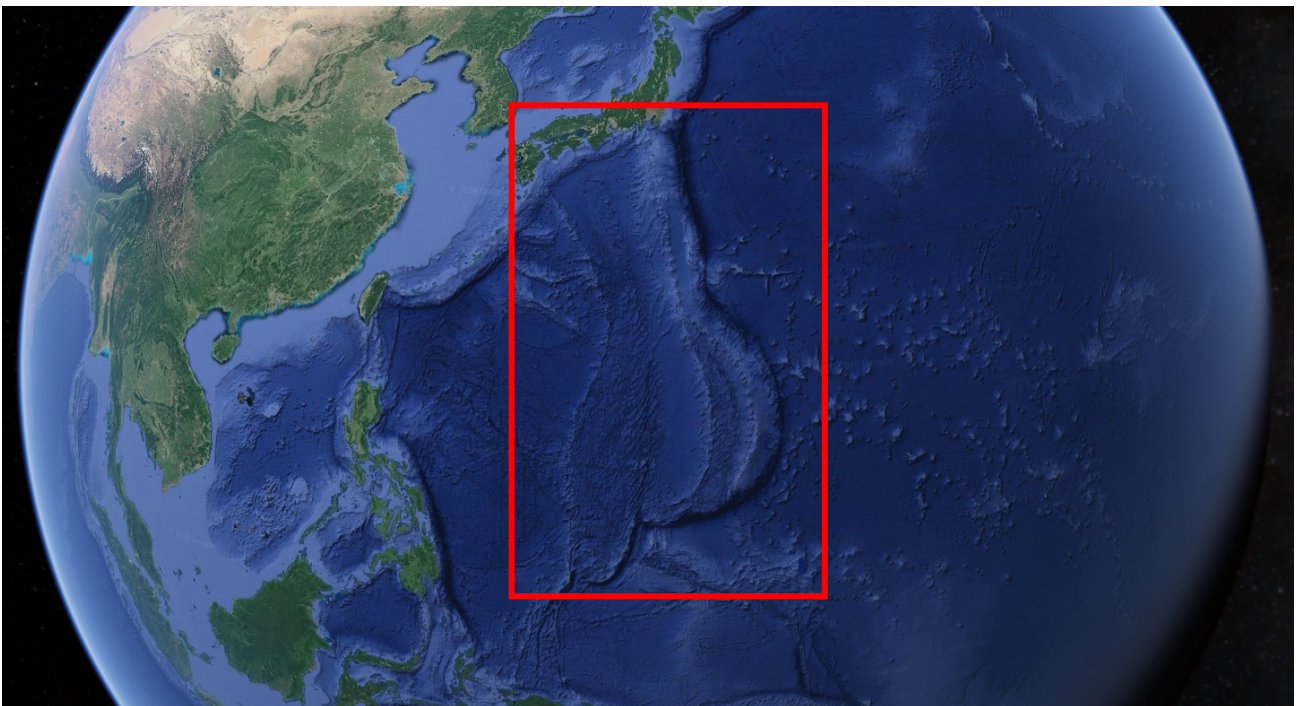
Fig. 1: Geographic position of the Izu-Bonin-Mariana arc system (Source: Google Earth, 2021).

2.2 Geological Situation

The non-accretionary Izu-Bonin-Mariana (IBM) arc system was formed as a result of the subduction of the western Pacific plate beneath the Philippine Sea plate and involves nowadays Eocene igneous basement, getting older from north to south (Stern et al., 2001). The subduction rates decrease towards the south, from ~2 cm per year up to 6 cm in the north (Klemperer, 2003 and references therein).

Since there is evidence for more recent seafloor spreading (divergent boundary) in the basin at the rear side of the volcanic arc (Karig, 1971), the so-called Mariana tough, the existence of a Mariana micro-plate as separation from the Philippine Sea plate was proposed (Bird, 2003). Eastwards, the Mariana plate is confined by the Mariana trench (see Figure 2 and 3), in which not only the deepest point on Earth is located (Cotter, 1965), it also marks the subduction front of the Pacific sea plate. Therefore, the Mariana micro-plate is lying between the Mariana trench and the Mariana trough (Bird, 2003). The forearc of the system covers the area between the trench axis and the active volcanic chain of the Mariana plate (Fryer and Mottl, 1992).
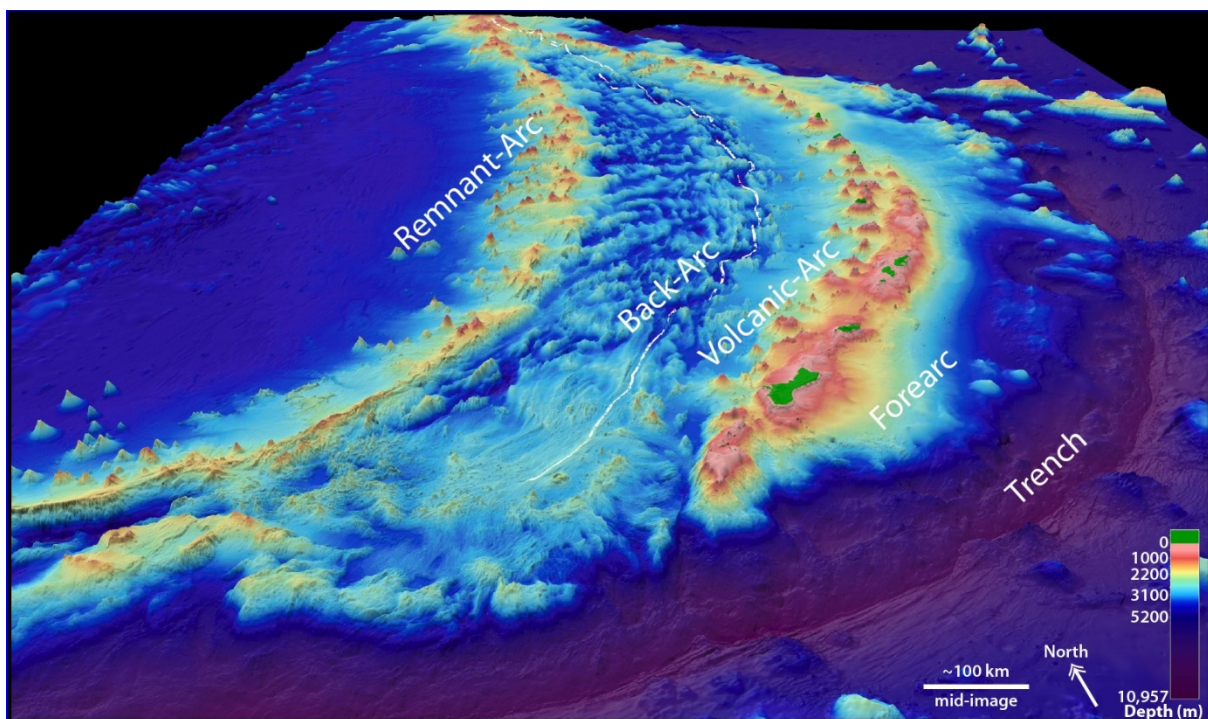
Fig. 2: Modelled view of the Mariana plate, showing the positions of Trench, Forearc, active Volcanic Arc, Back-arc (Mariana Trough) and Remnant-Arc (West Mariana Ridge). Five times vertical exaggeration, 125 m bathymetric compilation (modified after Embley et al., 2007).

Serpentinite seamounts on the Mariana forearc are common within 100 km west of the trench. By now more than 50 seamounts (Fryer and Fryer, 1987) and at least 19 active serpentinite mud volcanoes have been discovered (Fryer et al., 2017, 2018). Serpentinized muddy material and slab-derived fluids, originated from the subducted Pacific plate and the overlying oceanic

lithosphere of the Mariana plate, rise periodically through faults and fractures in the forearc region and form these massive structures (Fryer, 1992). The positions of the serpentinite mud volcanoes are related to active seeps, resulting from associated along- and across-strike faults, which penetrate the oceanic lithosphere and can reach depths up to 18 km, providing direct links to the subduction channel and different metamorphic and metasomatic conditions (Fryer et al., 2017, 2020). Previous work from Fryer et al. (1995, 2000) posited that the uplift of the Mariana forearc and the linked faulting is caused by the subduction of oceanic plateaus and seamounts from the Pacific plate. Alternatively, it is presumed that the forearcs' horst and graben structures with accompanied faults are caused by extension (Fryer et al., 1996), induced by the relatively fast subduction roll-back of the Pacific sea plate, creating the arc's characteristic shape (see Figure 2) (Harry and Ferguson, 1991). In contrast, Lallemand (2016) suspect altered relict paleo-transform faults for facilitating serpentinite diapirism.

A decrease in the degree of serpentinization of the mantle wedge beneath the forearc may limit the distance of the serpentinite seamounts from the subduction front (Stern and Smoot, 1998; Fryer et al., 2000). This assumption is supported by formerly drilled cores (IODP Leg 125) with ultramafic samples, only 10% serpentinized (Fryer et al., 2000), suggesting that the sub-forearc mantle is not entirely serpentinized (Oakley et al., 2007). Other authors assume that the forearc mantle wedge shows a much higher degree of serpentinization (>50%) (Bostock et al., 2002; Nagaya et al., 2016).

The serpentinization fluids originate from the dehydration of the downgoing slab, whereby about 30-70% of the subducted formation water is released beneath the forearc mantle and just 15-35% of the primordial water are released below volcanic fronts, causing arc magmatism (Schmidt and Poli, 1998).
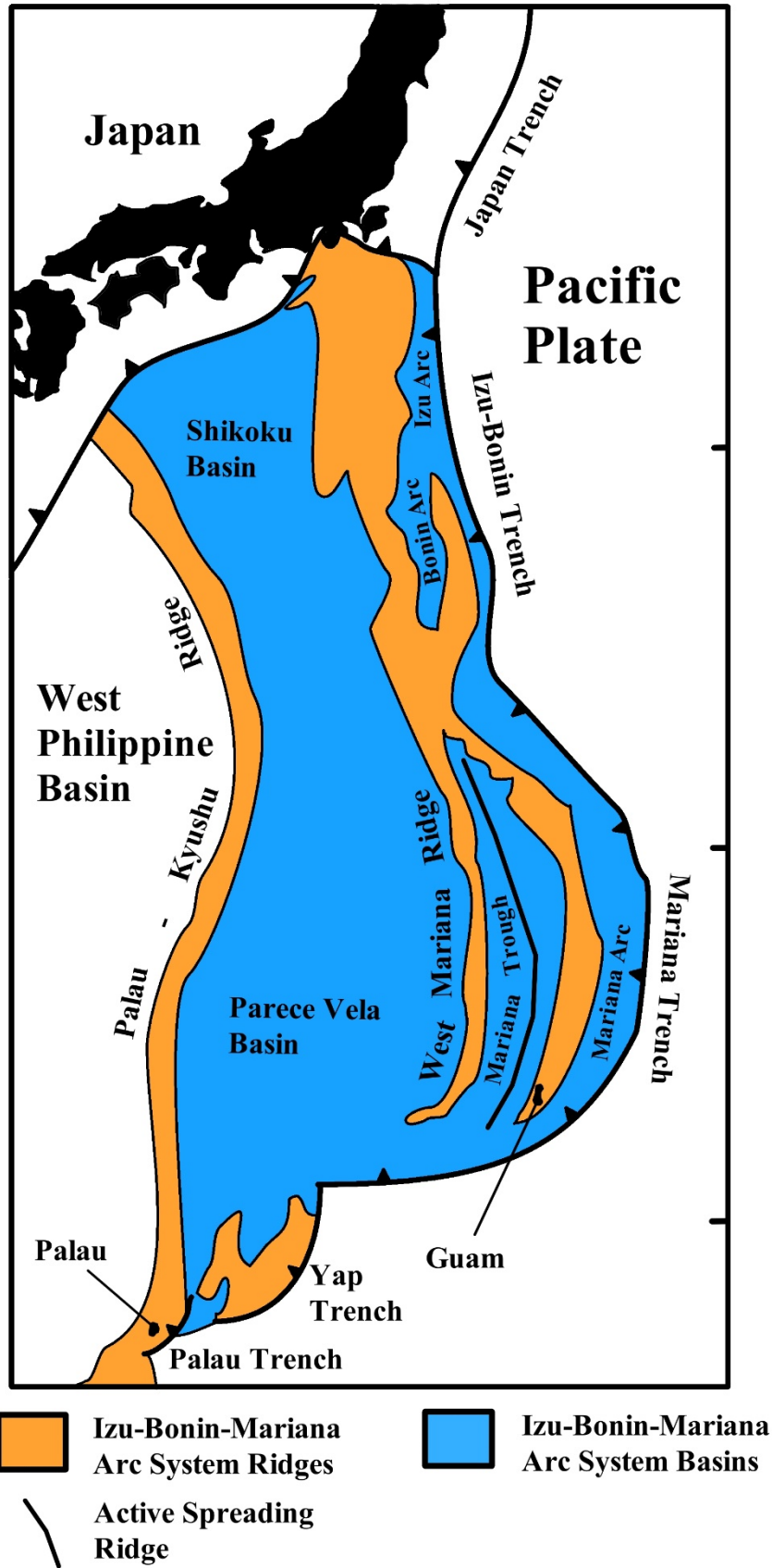
Fig. 3: Generalized tectonic map of the Izu-Bonin-Mariana arc system (after Stern et al., 2001).

Seismic profiles and bathymetric data showed that the subducting oceanic crust can reach thicknesses along the margin from 5.3 up to 7 km and is covered by 0.5 to 2 km of sediments (see Fig. 4), accompanied by several volcanic seamounts with heights around 2 to 3 km. In most of the regions the sedimentary cover was completely subducted, sporadically small accretionary prisms were formed. At the outer forearc where the serpentinite seamounts are located, the subducted Pacific plate dips 9 – 12 degrees. As apparent in Figure 4, the serpentinite mud volcanoes overlie 0.8 km sediments, 8.2 km forearc crust and 3.5 km of the mantle wedge (Oakley et al., 2008).

Furthermore, the incoming Pacific plate show extensional faulting at depth, coupled to flexural bending into the trench, whereby the largest fault offsets (0.5 – 0.7 km) occur along the trench (Ranero et al., 2003). The bending is potentially associated with a relatively fast subduction rollback of the incoming plate (Harry and Ferguson, 1991).

The sedimentary deposited siliceous ooze (Fig. 4, labelled as Chert Layer) from the subducted plate provide another possible source of silica for the serpentinization system (Albers et al., 2019), since large areas of the Pacific abyssal depths are below the carbonate compensation depth (e.g. Pytkowicz, 1970; Pälike et al., 2012).
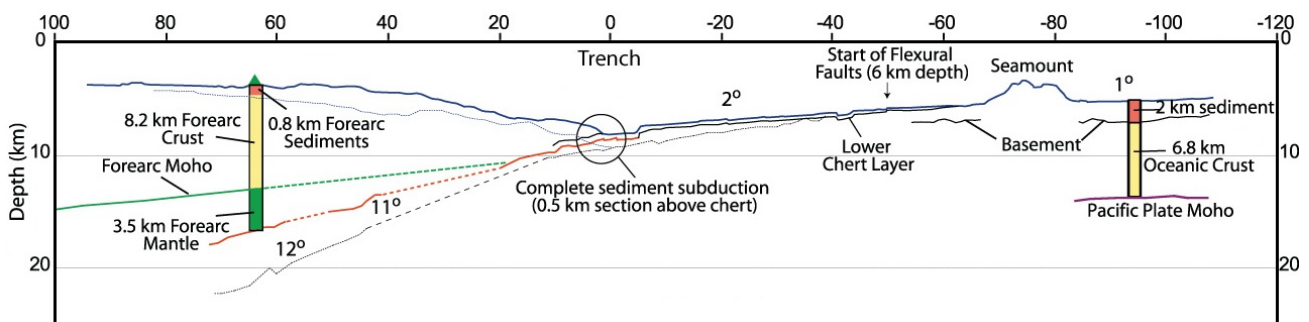
Fig. 4: Multichannel seismic reflection-based cross-section of the easternmost shallower part of the Mariana trench (~16°5'N) with sedimentary cover relations and slab dip (modified after Oakley et al., 2008).

2.3 Evolution of the Izu-Bonin-Mariana Arc System

According to scientific literature, initiation of the intra-oceanic subduction in the Izu-Bonin-Mariana convergent margin and neighboring systems is dated at Early Eocene times (e.g. Taylor, 1992; Fryer, 1996; Cosca et al., 1998). The subducting Pacific plate is Mesozoic in age (Jurassic to Cretaceous, Cosca et at., 1998) and covered by a relatively thin layer of sediments, ranging from 0.5 (subduction front) to 2 km (incoming plate) (LaTraille and Hussong, 1980; Oakley et al., 2008). It is scientifically widely proven that the subduction has been initiated at a transform fault along the margin of the Proto-Philippine basin at about 50 Ma (Hilde et al., 1977; Bloomer, 1983).

It is presumed that the earliest stages of the Philippine Sea plate evolution incept with a diffuse shortening in the region of the transform faults between the Mesozoic terranes and the Pacific plate (~60-55 Ma), followed by a localization of the deformation due to mantle convection and development into a subduction zone at around 52-50 Ma. Around 49-48 Ma, the first Boninites (named after the Izu-Bonin arc) were produced, simultaneously to the evolution of a mantle plume (Oki-Daito plume) which induced a splitting of the proto-Philippine plate into various ridges, detached by transitory oceanic basins. The subduction zone was ultimately initiated by a thrust fault along the transform boundary area, cutting through the oceanic lithosphere of the Pacific, followed by a change in motion of the plate (Hilde et al., 1977; Cosca et al., 1998; Lallemand, 2016).

The Parece-Vela basin (see Fig. 3) is an inactive arc basin and separates the relict arcs Palau-Kyushu and West Mariana Ridge (Scott and Kroenke,1980; Bloomer, 1983). Scott and Kroenke (1980) estimated the first period of back-arc seafloor spreading at the proto-Philippine plate from about 52 to 37 Ma with evidence for a second episode from 30 to 18 Ma, whereby the tholeiitic basalts of the Palau-Kyushu Ridge show ages from about 42 to 29 Ma. During the Oligocene, several million years after the spreading of the basin was firstly disrupted, intensive tholeiitic and calc-alkaline arc volcanism took place until at least of 29 – 27 Ma (Mariana) and 23 – 20 Ma (Izu-Bonin), accompanied by rifting and subsequent back-arc spreading (~25 Ma), creating the Parece-Vela and Shikoku basins and splitting the arc into an inactive western part (Palau-Kyushu Ridge) and the present active Izu-Bonin-Mariana arc (Taylor, 1992; Cosca et al., 1998; Lallemand, 2016). The West Mariana Ridge was separated from the active arc during the last seafloor spreading episode (see Fig. 5) from around 7 Ma to recent by an active back-

arc basin, the so-called Mariana Trough (Bloomer, 1983; Arculus et al., 2015; Lallemand, 2016). Today's calc-alkaline arc volcanism (e.g. Bloomer, 1983) of the Izu-Bonin-Mariana system resumed from about 15 Ma (Cosca et al., 1998).

Lallemand (1995, 2016) posited a significant tectonic erosion of the subduction front during Cenozoic times, coupled to subsidence and volcanic arc retreat (Fig. 4), evidenced by outcropping older bonitites, tholeiites and forearc basalts next to the trench. Calculations for the Izu-Bonin-Mariana system assume a mean rate of 7±3 km/Ma landward migration of the arc in Cenozoic times (Lallemand, 2016). Other authors believe that an earlier subsidence of denser lithosphere along a transform fault with accompanied strong extension led to a so-called "spontaneous subduction" (e.g. Stern and Bloomer, 1992; Arculus et al., 2015).

54 - 48 Ma

Mesozoic   Pacific Crust
Terranes   Jurassic - Cretaceous

Transform Fault

49 - 44 Ma

Boninites
                    Wedge of Pacific Crust
        TF
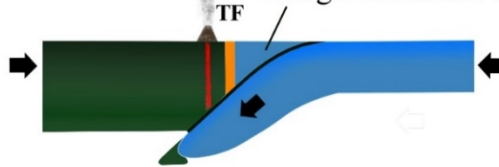
45 - 40 Ma

Tholeiites and
calc-alkaline Andesites
                 TF
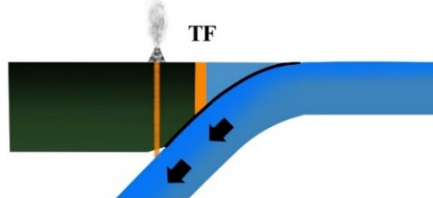
40 Ma - present

Volcanic arc retreat
                 Eroded frontal part
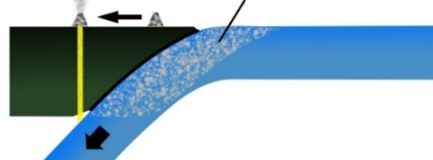
Fig. 4: Simplified illustration of the Izu-Bonin-Mariana arc system initiation and early evolution (after Lallemand, 2016).

30 - 18 Ma

Shikoku and
Parece-Vela basin
Active arc

7 Ma - present

Palau-Kyushu Ridge
West Mariana Ridge
Mariana Trough
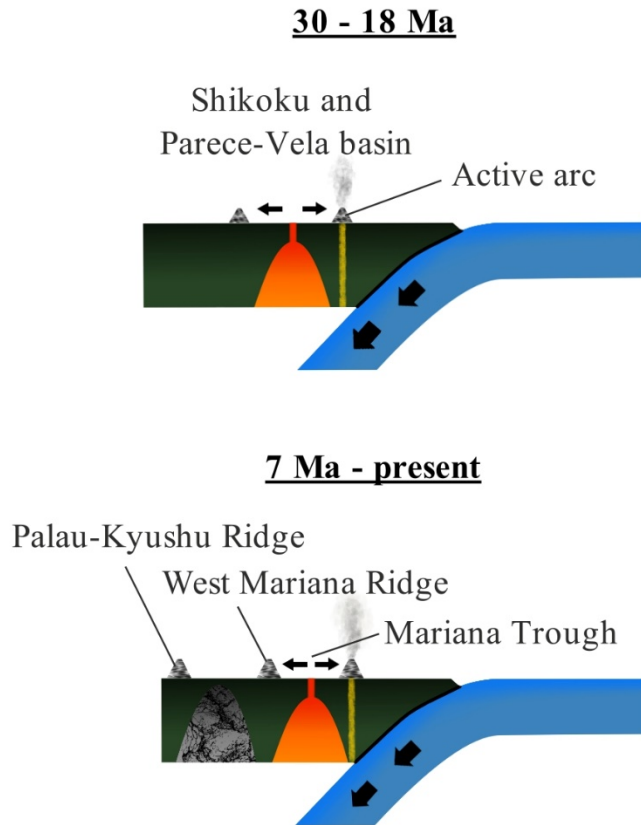
Fig. 5: Simplified back-arc extension history of the Mariana subduction system, viewed along E–W cross sections (after Taylor, 1992).

The prominent present-day eastward bowed-out shape of the Mariana arc system is caused by the back-arc extension around 30 – 18 Ma (Fig. 5), where the arc prograded simultaneously north and south (Taylor, 1992). During the second episode of seafloor spreading from around 7 Ma until present, the Mariana Trough opened and separated the Western Mariana Ridge from the active volcanic arc, thereby contributing to the progressive bending of the Mariana arc system (e.g. Fryer, 1996).

The oldest indications for serpentinization processes within the arc system were found in sediments of middle Eocene age overlying serpentinized mantle rocks (Fryer et al., 1995).

2.4 Asút Tesoru Seamount

The Asút Tesoru Seamount is a serpentinite mud volcano, located on the Mariana forearc system between 18°N and 18°10'N, around 72 km west of the trench (Hulme et al., 2010). The subducting slab is towered over by the summit of the seamount around 18 km (Oakley et al., 2007, 2008), thereby it is one of the deepest-sourced mud volcanoes at the Izu-Bonin-Mariana arc system. Asút Tesoru reaches a height of 2.4 km above seafloor with a diameter of around 50 km, which also represents the largest serpentinite seamount in the Mariana forearc (Oakley et al., 2007).
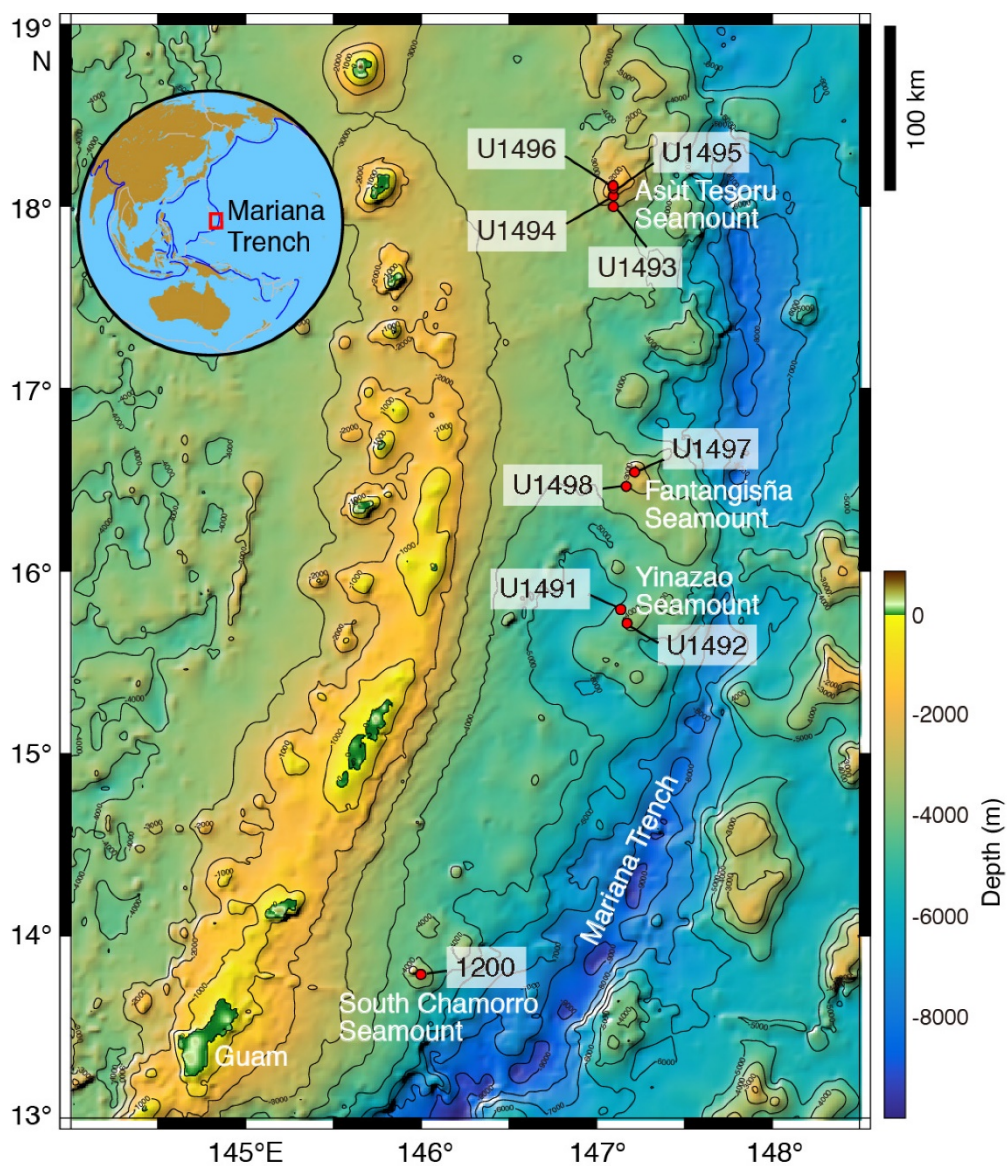
Fig. 6: Bathymetric location map of the serpentinite seamounts with the drilling sites U1491 - U1498 (IODP Expedition 366) and 1200 on South Chamorro Seamount (Fryer et al., 2018).

The surface of the seamount, especially in the peak area, can be described as irregular, most likely due to intersecting subsurface fault trends (NNE to NNW), which also controlled the accumulation of serpentinite muds and thus the growth of the mud volcano. Further expeditions recovered samples directly from the sedimentary basement beneath the seamount, analyses of the very same unveiled serpentinite contents of ~50%, suggest a possible activity of Asút Tesoru since Eocene (Fryer et al., 2017).

The summit area is dominated by a prominent conical shaped dome, partially filling a fault-bounded summit depression with an oval extent of circa 2 km x 3 km towards the northeast (Oakley et al., 2007). The center of this mound at the peak of the seamount show active fluid discharge (Fryer et al., 2017), reaching the highest flux rate (36 cm/year) among all seamounts of the Mariana forearc (Hulme et al., 2010). Furthermore, the ascending fluids at Asút Tesoru show extremely low calcium concentrations and pH values up to 12.5 (Mottl et al., 2003; Hulme et al., 2010). The temperature of the slab beneath the mud volcano is assumed ≥200°C (Hulme et al., 2010), or up to ~250°C, respectively (Fryer et al., 2018 and references therein).

2.4.1 Drilling Sites and Cores

According to the Preliminary Report from Fryer et al. (2017), the four Expedition 366 drilling Sites U1493, U1494, U1495 and U1496 form a ~14 km transect line from south to north (see Fig. 7) at the Asút Tesoru serpentine mud volcano. The drilling operations started from the southern deeper flank sites of the seamount at U1493 (3,359 mbsl) and U1494 (2,200 mbsl) in a line northbound to site U1495 (1,400 mbsl) and culminated at the summit site U1496 (1.240 mbsl). The recovered material from the flank sites (U1493, U1494, U1495) show a combined stratigraphy with little variations and reached depths of 32.6, 39.0 and 10.8 meters below the surface. The serpentine muds are mostly overlain by pelagic muds, whereby the thickness of the mud layer varies, from approximately 80 cm at site U1493 to 0 cm at site U1494. Furthermore, the deepest site's (U1493) sedimentary cover shows extensive oxidizing conditions, discernible on microfossil-bearing reddish–yellow serpentine muds, whereas upslope sites exhibit thinner oxidized zones. Since site U1496 is located at the summit and therefore in the active eruptive area of the seamount, recovered samples contain very little

pelagic sediment above the serpentine mud. In general, beside the oxidized sediments the recovered samples grade from pale green to dark blue with depth, show varying particle size and contain different amounts of serpentinized ultramafic clasts (Fryer et al., 2017, 2018).
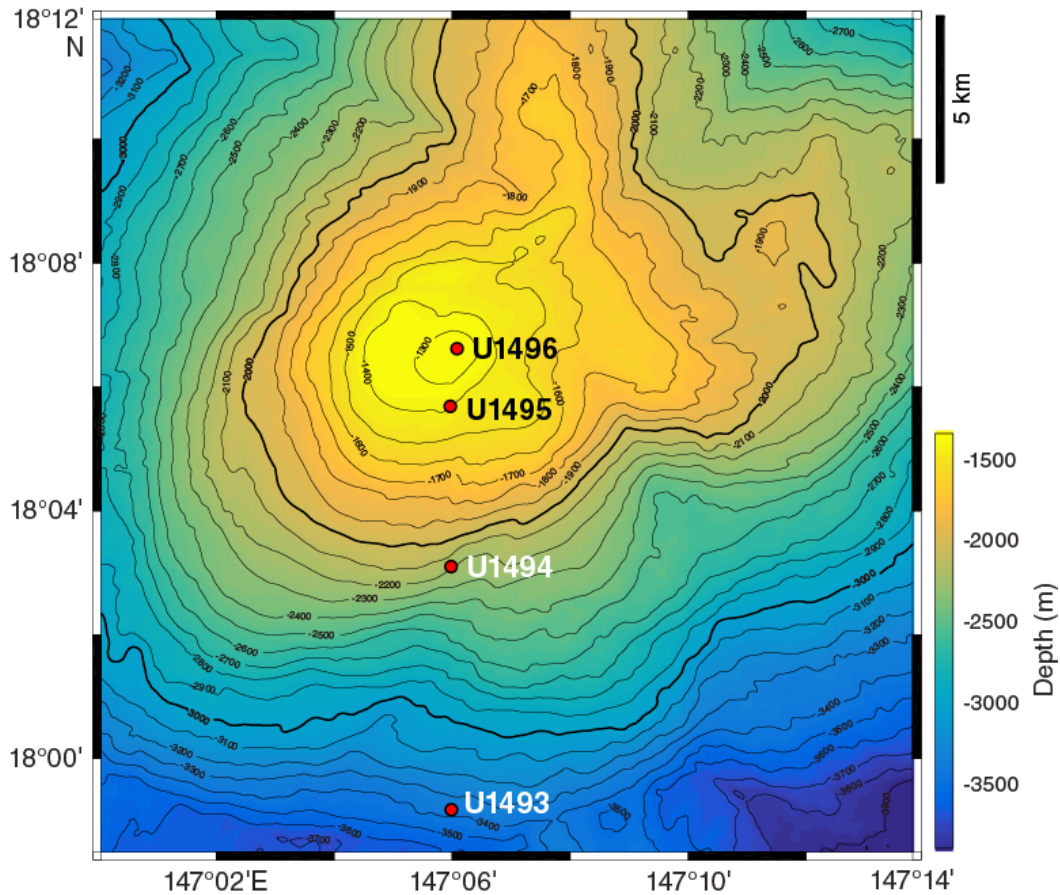
Fig. 7: Bathymetric map of the Asút Tesoru seamount with positions of Sites U1493 to U1496 (Fryer et al., 2018).

At the sites at Asút Tesoru, in total 8 holes were drilled (see Tab. 1), whereby 6 whole cores were recovered with enough material for the reconstruction of stratigraphic successions (U1493B, U1494A, U1495A/B, U1496A/B), as displayed in Figure 8. The cores were divided into lithostratigraphic units based on lithologic and mineralogic composition, oxidations state, and proportion of clasts within the matrix (Fryer et al., 2018).
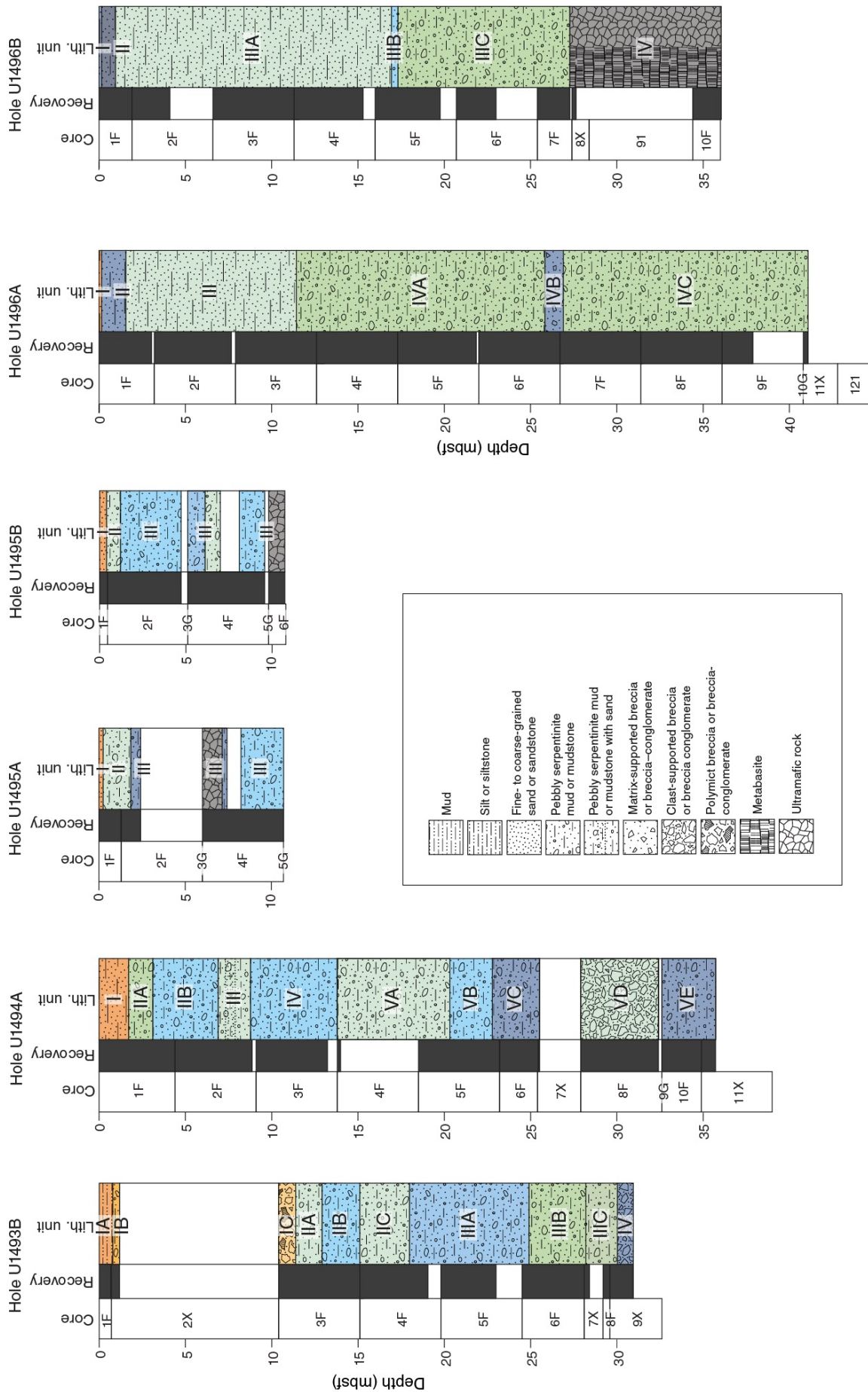
Fig. 8: Lithostratigraphy of the cored material from Asút Tesoru Seamount with depth and labelled subunits (modified after Fryer et al, 2018).

2.4.2 Samples

The drilling procedures at Asút Tesoru yielded six whole cores with enough material for further investigations (Fryer et al., 2017). The following listing shows the relevant information for all boreholes, with analyzed cores in bold type. Altogether, the investigated drill cores are composed of 45 recovered single cores (see Tab. 1), segmented and labelled as sections.

Hole	Latitude	Longitude	Water depth (mbsl)	Cores (N)	Interval Cored (m)	Core recovered (m)	Recovery (%)	Total penetration (m)
U1493A	17°59.1668'N	147°06.0057'E	3358.92	1	0.1	0.09	90	0.1
U1493B	**17°59.1665'N**	**147°06.0060'E**	**3358.92**	**9**	**32.6**	**19.03**	**58.37**	**32.6**
U1494A	**18°3.0896'N**	**147°6.0003'E**	**2199.80**	**10**	**39.0**	**27.99**	**71.77**	**39**
U1495A	18°05.6693'N	147°06.0004'E	1405.81	3	10.7	4.84	45.23	10.7
U1495B	**18°05.6788'N**	**147°05.9901'E**	**1401.89**	**4**	**10.8**	**10.18**	**94.26**	**10.8**
U1496A	**18°6.5936'N**	**147°6.0999'E**	**1243.38**	**10**	**42.8**	**38.36**	**89.63**	**44.8**
U1496B	**18°6.6205'N**	**147°6.0998'E**	**1240.18**	**9**	**30.0**	**22.08**	**73.60**	**36.0**
U1496C	18°06.6068'N	147°06.1001'E	1243.17	11	105.0	8.52	8.11	105.0

Tab. 1: Asút Tesoru hole summary, including location/GPS data and relevant drillcore information (Fryer et al., 2018).

For the purpose of this thesis, 27 samples from 5 of the drilled cores (see Tab. 2) from both flank and summit sites were investigated with different analyzing methods. The selected samples were chosen to be representative for all cored boreholes and cover the whole area of Asút Tesoru seamount, from the bottom to the top. For interpretation and more comprehensive conclusions, the results were compared with published data from literature.

Label identifier	Internal label	Position
366-U1493B-2X-1-W 19/21-KURZ1	1-1493B-56	Flank/Bottom
366-U1493B-3F-5-W 50/60-KURZ1	1-1493B-61	Flank/Bottom
366-U1493B-4F-CC-W 20/30-KURZ1	1-1493B-62	Flank/Bottom
366-U1493B-6F-3-W 25/40-KURZ1	1-1493B-63	Flank/Bottom
366-U1493B-8F-CC-W 34/44-KURZ1	1-1493B-64	Flank/Bottom
366-U1494A-1F-4-W 33/36-KURZ1	1-1494A-73	Flank
366-U1494A-1F-CC-W 5/15-KURZ1	1-1494A-74	Flank
366-U1494A-3F-4-W 50/60-KURZ1	1-1494A-78	Flank
366-U1494A-5F-2-W 5/23-KURZ1	1-1494A-79	Flank
366-U1494A-5F-2-W 71/85-KURZ1	1-1494A-80	Flank
366-U1494A-5F-3-W 98/113-KURZ1	1-1494A-81	Flank
366-U1494A-6F-2-W 15/23-KURZ1	1-1494A-82	Flank
366-U1494A-9G-1-W 30/40-KURZ1	1-1494A-83	Flank
366-U1494A-10F-1-W 32/38-KURZ1	1-1494A-84	Flank
366-U1494A-10F-2-W 46/56-KURZ1	1-1494A-85	Flank
366-U1494A-10F-2-W 100/106-KURZ1	1-1494A-86	Flank
366-U1495B-2F-CC-W 15/25-KURZ1	1-1495B-89	Next to Summit
366-U1495B-4F-3-W 70/80-KURZ1	1-1495B-95	Next to Summit
366-U1496A-4F-4-W 18/28-KURZ1	1-1496A-103	Summit
366-U1496A-5F-3-W 83/93-KURZ1	1-1496A-105	Summit
366-U1496A-6F-5-W 60/70-KURZ1	1-1496A-110	Summit
366-U1496A-8F-2-W 41/51-KURZ1	1-1496A-113	Summit
366-U1496B-3F-2-W 30/40-KURZ1	1-1496B-118	Summit
366-U1496B-5F-1-W 85/95-KURZ1	1-1496B-123	Summit
366-U1496B-6F-2-W 0/6-KURZ1	1-1496B-125	Summit
366-U1496B-6F-2-W 41/51-KURZ1	1-1496B-126	Summit
366-U1496A-2F-2-W 38/49-KURZ	1-1496A-270	Summit

Tab. 2: List of investigated samples with official IODP label, internal denotation, and relative position of sampling.

3. Methods and Procedures

The investigated material was collected by the JOIDES Resolution science party during International Ocean Discovery Program (IODP) Expedition 366, which took place from 8 December 2016 to 7 February 2017. Recovered samples from the drilling operations were firstly investigated with the shipboard available standard analyzing techniques of the shipboard laboratory, including smear slides, portable X-ray fluorescence spectrometer (pXRF) and inductively coupled plasma–atomic emission spectroscopy (ICP-AES) (Fryer et al., 2017).

Through a combination of results from former investigations and further post-expedition land-based data collection (such as this thesis), greater coherences and refined models could be provided.

All measurements and analyses were made at the Institute for Earth Sciences, NAWI Graz Geocenter (Karl-Franzens University of Graz).

3.1 Smear Slide Analysis

Since the majority of the recovered core material is typically composed of unlithified fine-grained serpentine mud, the smear slides offer a relatively quick opportunity for a first semi-quantitative identification and characterization of major and minor components, lithology and mineralogy (Kelts, 1998). First presented by Mazzullo and Graham (1988) for the purpose of core description by shipboard sedimentologists, by now it is a standard analyzing method at IODP Expeditions for visual core observations.

For a first estimation of the grain size distribution and especially for the modal minerology of the samples, smear slides were prepared. They were analyzed by using an Olympus BX50 petrographic microscope, equipped with a Zeiss Axiocam IC. For training, references and as a guideline for the optical determination of different components, the "IODP Smear Slide Digital Reference for Sediment Analysis of Marine Mud" (Part 1 and 2) from Marsaglia et al., (2013, 2015) was used.

3.2 X-Ray Powder Diffraction

For the identification of mineral phases, or rather to determine unknown mineral phases, X-ray powder diffraction (XRD) is a common geological technique and was used for the investigations. The analyzed material was finely ground with an agate mortar and homogenized before being placed on the sample holder of the diffractometer. For determining the average bulk mineralogy of the samples, a Siemens D5000 X-ray diffractometer, with a voltage of 40.0 kV and an amperage of 40 mA was used. To perform measurements, a Bragg-Brentano array with fixed sample (2-theta scale) was used, and data were collected from 4.1° to 65° by 0.02° step size with 0.1 to 0.6 sec. step time. To identify mineral phases, the resulting diffraction patterns were compared with the Department's computerized database of reference data.

3.3 X-Ray Fluorescence Analysis

For the preparation of whole rock analyses, a representative amount of the sample was taken (>50 g) and powdered with a swing mill (tungsten-carbide), before samples were placed in a compartment dryer for at least 24h at around 105°C. The Loss on Ignition (LOI) was determined by heating of circa 1 g of powdered sample material in a ceramic crucible at around 1000°C for 60 minutes, followed by cooling down for 60 minutes in a desiccator. Afterwards the loss on ignition was calculated using a formula-based Excel sheet.

The glass beads for the X-ray fluorescence analysis (XRF) were created by mixing 7 g di-Lithium-tetraborate flux additive (Fluxana FX-X100-2) and 1 g of powdered and heterogenized sample material at an accuracy of ±0.0004 g, with following fusion (Fusion Machine VAA 2M) at 1200 to 1300°C.

The bulk rock analyses were conducted with a Bruker S4 Pioneer wavelength dispersive XRF, using the ultramafic-calibrated reference standard GEOUm, suitable for mantle-derived chemical compositions. For comparison of the collected with literature data, the internet-based "Geochemical Earth Reference Model (GERM)" database was used. After recalculation of the geochemical data to a LOI free base, plots were created using Geochemical Data Toolkit (GCDKit) 6.0 in R 3.6.0 from Janoušek et al. (2006).

3.4 Raman Spectroscopy

Because the samples consist mainly of unlithified fine-grained serpentine mud, for implementation of Raman spectroscopy the material had to be prepared. For this purpose, the loose material was infused in a two-component resin (7:1 mix proportion) in the form of tablets.

The analyses were conducted with a HORIBA Jobin Yvon HR-800 Raman Microspectrometer with a CCD detector, and samples were illuminated using a 632 nm He-Ne (red) laser beam with 2x 20 to 30 sec. step time.

For calibration, a wafer of pure silicon, whose peak position of intensity is well-known (520 nm), was used. For phase identification, the resulting intensity spectra were compared with the "Spectral-ID" integrated database provided from HORIBA Scientific and with the internet-based database of the RRUFF project from Lafuente et al. (2015).

3.5 Electron Microprobe Analysis

Samples were further prepared and polished for electron microprobe analysis.

The composition of mineral phases was determined using JEOL JXA-8530FPlus HyperProbe Electron Probe Microanalyzer (EPMA), equipped with an energy-dispersive (EDX) and five wavelength-dispersive (WDX) spectrometers, reaching a precision of ±1%. Sample pictures were taken with the scanning electron microscope (BSE pictures) of the device. Before measurements, polished resin-enclosed samples were coated with carbon. Quantitative analyses were performed by using wavelength-dispersive spectrometers (WDS) with a beam diameter of 1-5 μm with an acceleration voltage of 15 kV and a beam current of 10 nA.

The proportions of the respective spinel group endmembers together with a generalized mineral formula were calculated using the application End-Members Generator (EMG) as proposed by Ferracutti et al. (2014). The garnet endmember and mineral formula were calculated using the Wolfram Mathematica script Petrological Elementary Tools (PET) from Dachs (1998).

4. Results

4.1 Petrography and Structures

The material recovered from IODP Expedition 366 consists mainly of cryptocrystalline serpentine mud with commonly occurring lithic clasts (>2 mm) in different amounts and size, with a thin cover of pelagic oxidized sediments, varying in thickness with position. The deformed, folded appearance of the samples is caused by drilling disturbance and coring, and doesn't reflect an original stratification.

4.1.1 Samples from U1493B

The bulk of the matrix from samples ranges from pale greenish over intensive dark green to dark greyish-blue serpentine mud. The only exception is sample U1493B-56, which represents the oxidized sedimentary cover with a reddish-orange to brown color and a completely different mineralogy. Optical microscopy showed that the sample is from a carbonate rich layer, mostly aragonite, discernible due to idiomorphic acicular crystals, with the grain size of sand. The reddish-brown tinge originates from Fe-rich minerals, most likely pseudomorphs of hematite after magnetite. Serpentine minerals show an elongated and fibrous shape and occur just in minor quantities, silt to clay-sized in sample U1493B-56.

The serpentine mud in sample U1493B-61 (Core 3F, Section 5) shows an intensive dark blue color with a primary clayey-sized matrix and sand-sized opaque magnetite. At smear slides, conspicuous brownish-green anhedral minerals with slight pleochroism to pale green are identifiable, certainly chlorite. Minor components in the matrix are brown organic matter, lithic clasts of various size and fragments of microfossils.

Mud samples from hole U1493B show abundant pseudomorphic serpentinized minerals in the matrix, mostly bastite (after pyroxene), recognizable on characteristic cockscomb dissolution textures and relict cleavage. In some cases, the serpentine minerals form elongated and fibrous assemblages within the matrix. As displayed in figure 9, some samples contain mesh textures (after olivine), sometimes with relict cores. The most abundant accessory mineral is isomorphic magnetite (or spinel). Also carbonates and hydrogarnet (62, 63) are identifiable.

In general, the serpentine muds from hole U1493B show a continuous transition with sampling depth (1) from dark blue towards bluish-green color, (2) from dominating clayey to sandy particle size, and (3) an increase in rock clast size.
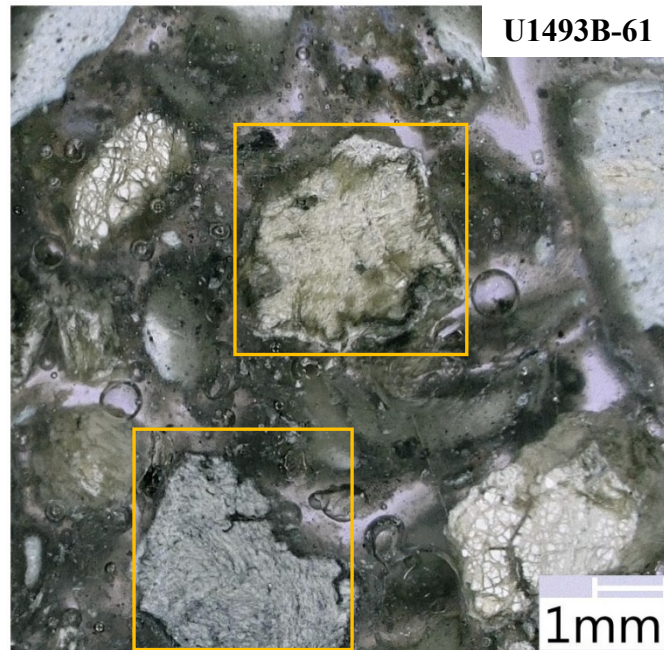
Fig. 9: Completely serpentinized pseudomorphic mineral grains.
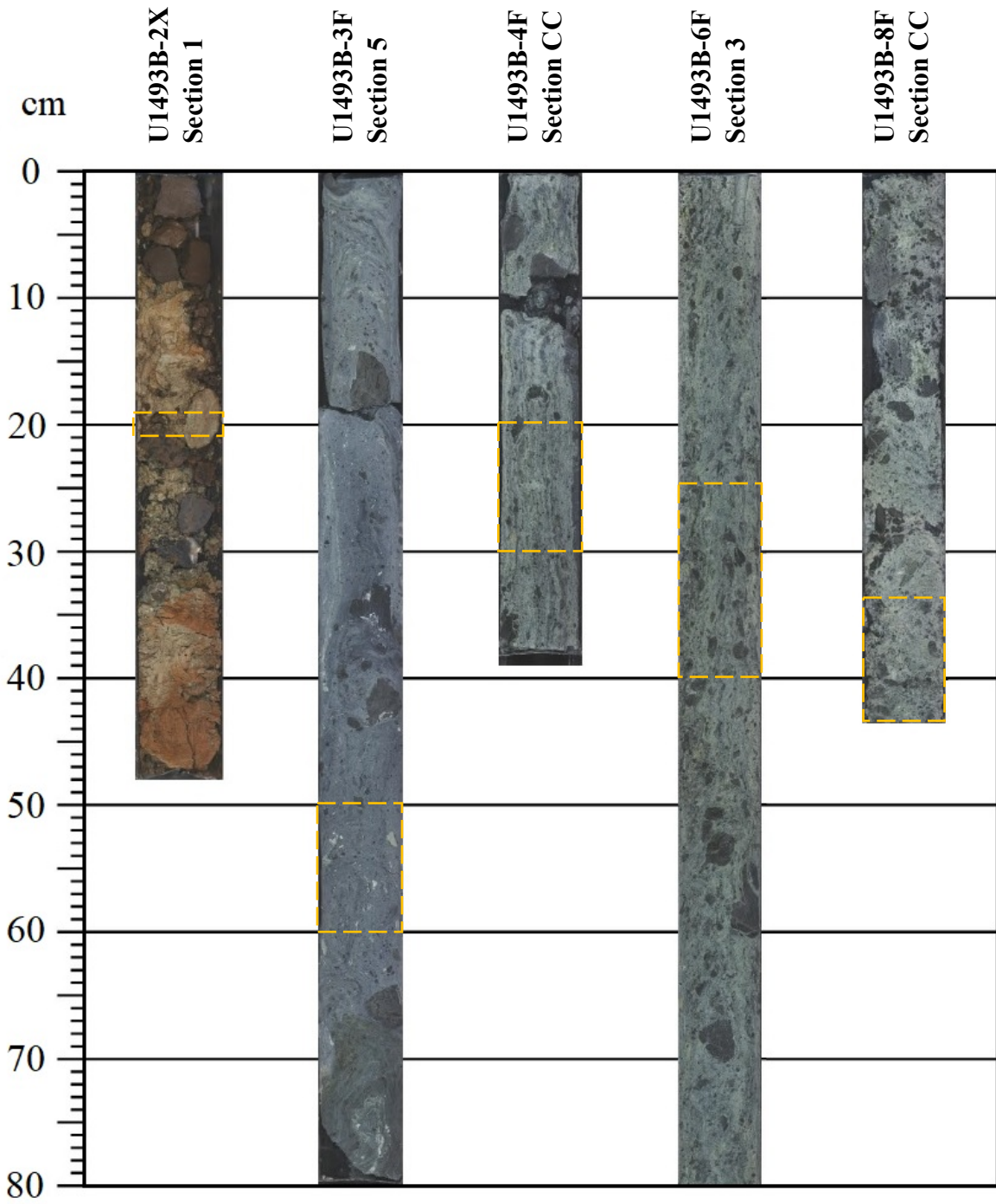
Fig. 10: Compilation of the sampled sections from borehole U1493B. Sample size shown in orange squares. Core pictures from Fryer et al. (2017).

4.1.2 Samples from U1494A

The samples are dominated by dark blue to greenish-blue serpentine muds with varying grain size and numerous rock and mineral clasts. Only in sample U1494A-74 microfossils could be found, most likely foraminifera filled with opaque pyrite, embedded in a clayey-sized serpentine mud matrix. Furthermore, intensive red mineral fragments with conchoidal fractures were found in smear slides, perhaps spinel. Silt-sized idiomorph grains of magnetite were also identified in sample U1494A-74.

Samples taken from the single cores 1F and 3F (73, 74, 78) exhibit a pale green to blue tinge with evidence for minor brucite crystals. Bastite textures are abundant, but also small relict pyroxenes with reaction rims can be recognized, most likely augite and enstatite, according to the distinct cleavage surfaces. Small anhedral greenish flakey components show weak pleochroism and may be chlorite.

Samples from deeper parts of the borehole (5F, 6F, 9G and 10F), that encloses 79, 80, 81, 82, 83, 84, 85 and 86, show a much more intensive dark blue color, partially interpenetrated by bright layers. In general, the grain size of the serpentine mud is sandy to clayey with slightly varying proportions. Abovementioned samples 79, 80, 81, 82, 83, 84 are composed of a highly serpentinized mud matrix with relict pyroxenes, minor magnetite and rarely spinel fragments.

Two samples from single core 5F (79, 80) are slightly coarser, with mainly sandy to silty-sized serpentinite muds and minor magnetite, additionally containing trace hydrogarnet. Sample 81 also shows the occurrence of hydrogarnet, but the mud matrix is finer-grained and contains infrequently intensive red idiomorphic spinel fragments.

From core 10F, samples 85 and 86 protrude due to the high content of silt-sized partially unaltered pyroxene crystals and relatively high chlorite content. Furthermore, these samples comprise minor carbonates (eventually calcite) and mesh textures after olivine (only sample 85).
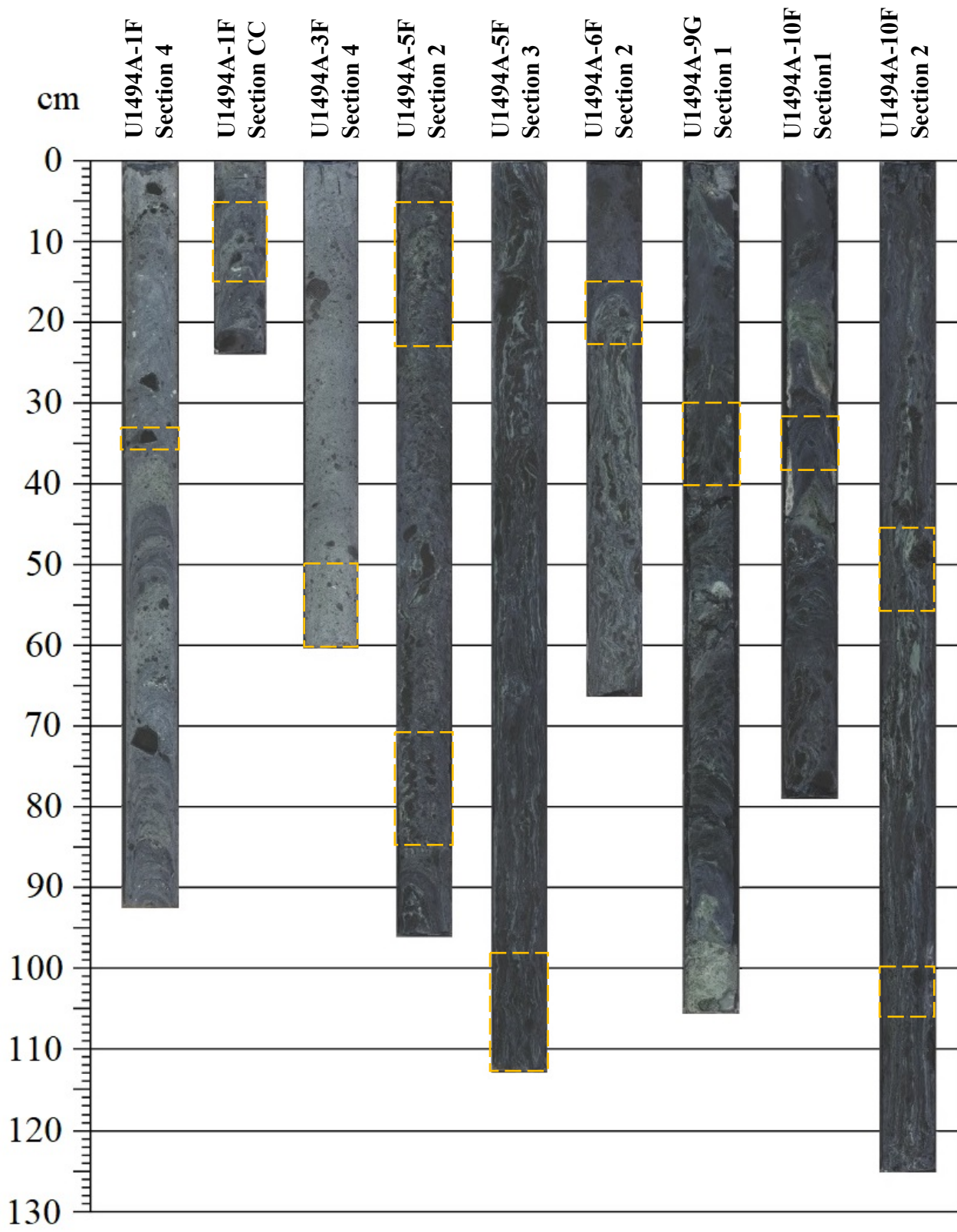
Fig. 11: Compilation of the sampled sections from borehole U1494A. Sample size shown in orange squares. Core pictures from Fryer et al. (2017).

4.1.3 Samples from U1495B
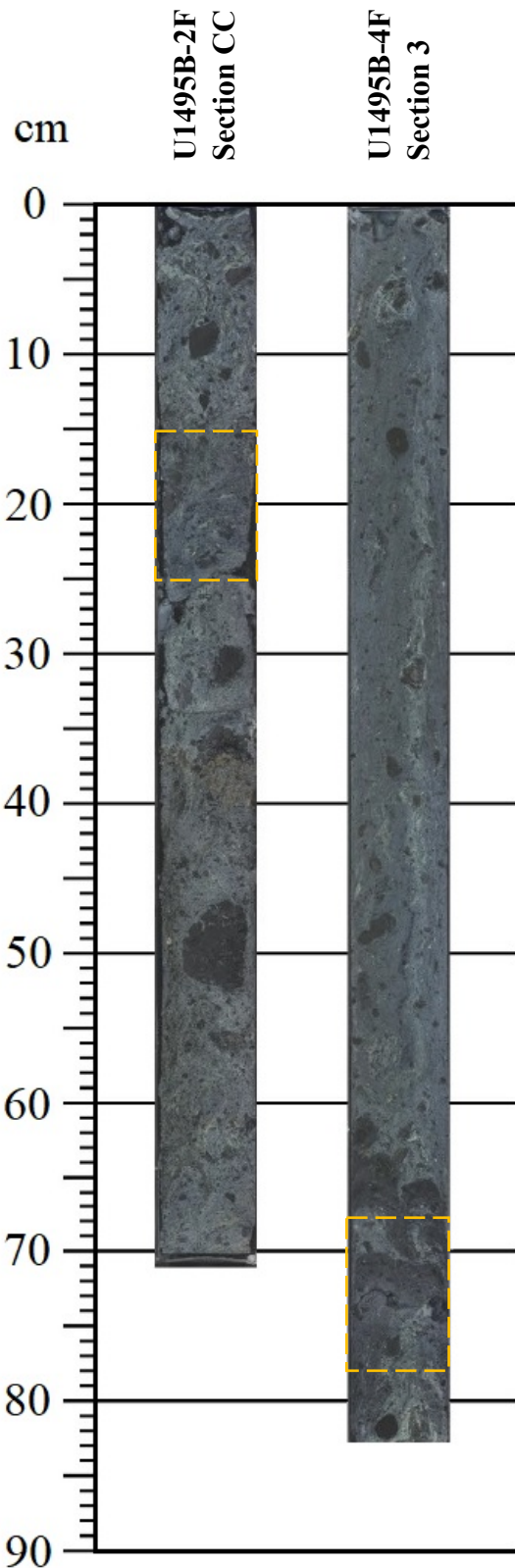
Samples taken from hole U1495 (89, 95) are composed of intensive blue to sporadically pale green colored serpentine mud with small grains or aggregates of magnetite. The general grain size of the mud is sandy to silty. Furthermore, sample 95 contains abundant fragments of lithified serpentinite silt-/sandstones, iron oxides and trace brucite. Sample 89 show plenty opaque minerals mostly magnetite, and trace calcite (debris), iron oxides and hydrogarnet, eventually chlorite.

In general, it can be said that material from U1495B is coarser and contains more ferrous phases relative to the previously described samples.

Fig. 12: Compilation of the sampled sections from borehole U1495B. Sample size shown in orange squares. Core pictures from Fryer et al. (2017).

4.1.4 Samples from U1496A and B

The cryptocrystalline serpentine matrix of investigated samples from borehole U1496A show a pale bluish color with varying amounts of lithic clasts. Sample 270 (core 2F) includes even no larger clasts and is composed of dominant clayey serpentine with subordinate brucite and traces of opaque magnetite, chlorite, hydrogarnet, relict pyroxene and reddish-brown idiomorphic spinel.

The cores from hole U1496A (2F, 4F, 5F, 6F and 8F) are mainly composed of silt- to clay-sized serpentine, with varying amounts of magnetite and brucite, and minor chlorite and fragments of carbonates. In all samples brownish-red spinel is abundant (103, 105, 110, 113), showing a variety of crystal shapes, both euhedral to anhedral. Some serpentinized mineral grains host hydrogarnets. Furthermore, bastite textures after pyroxene, affected by a brownish-green alteration, could be found.

The lithic clast content in the generally fine-grained mud matrix of hole U1496A varies considerably, from almost no clasts (core 2F, sample 270) to extremely clast-rich (core 6F-5, sample 110) with relatively unaltered rocks, showing sizes up to several centimeters. Unlike drill cores from flank or bottom sites, samples from hole U1496A displays a predominantly homogeneous mixture with no distinctive signs for stratification or drilling-related structures.

Samples of drill cores from hole U1496B vary not significantly from U1496A, since the sites lie close to each other. Most of the investigated samples (123, 125, 126) show a pale blue tinge with bulk clayey serpentine mud matrix. Sample 118 contains up to around 25% sand/silt-sized particles. All the samples comprise infrequent bastite textures after pyroxene and plenty opaque phases (most likely magnetite), combined with brownish iron oxides and minor chlorite and brucite. Furthermore, fragments of trace carbonates and spinel could be identified. Samples from cores 6F and 5F show the presence of anhedral greenish hydrothermal garnet and volcanic glass. Samples originating from core 6F (125, 126) contain minor relict pyroxenes with greenish-brown reaction rims and distinct cleavage, but without characteristic dissolutions like cockscomb textures.

Another noticeable feature of the drill core samples is the outward change of color after several days under atmospheric conditions, from the original pale blue to a yellow tinge on the surface.
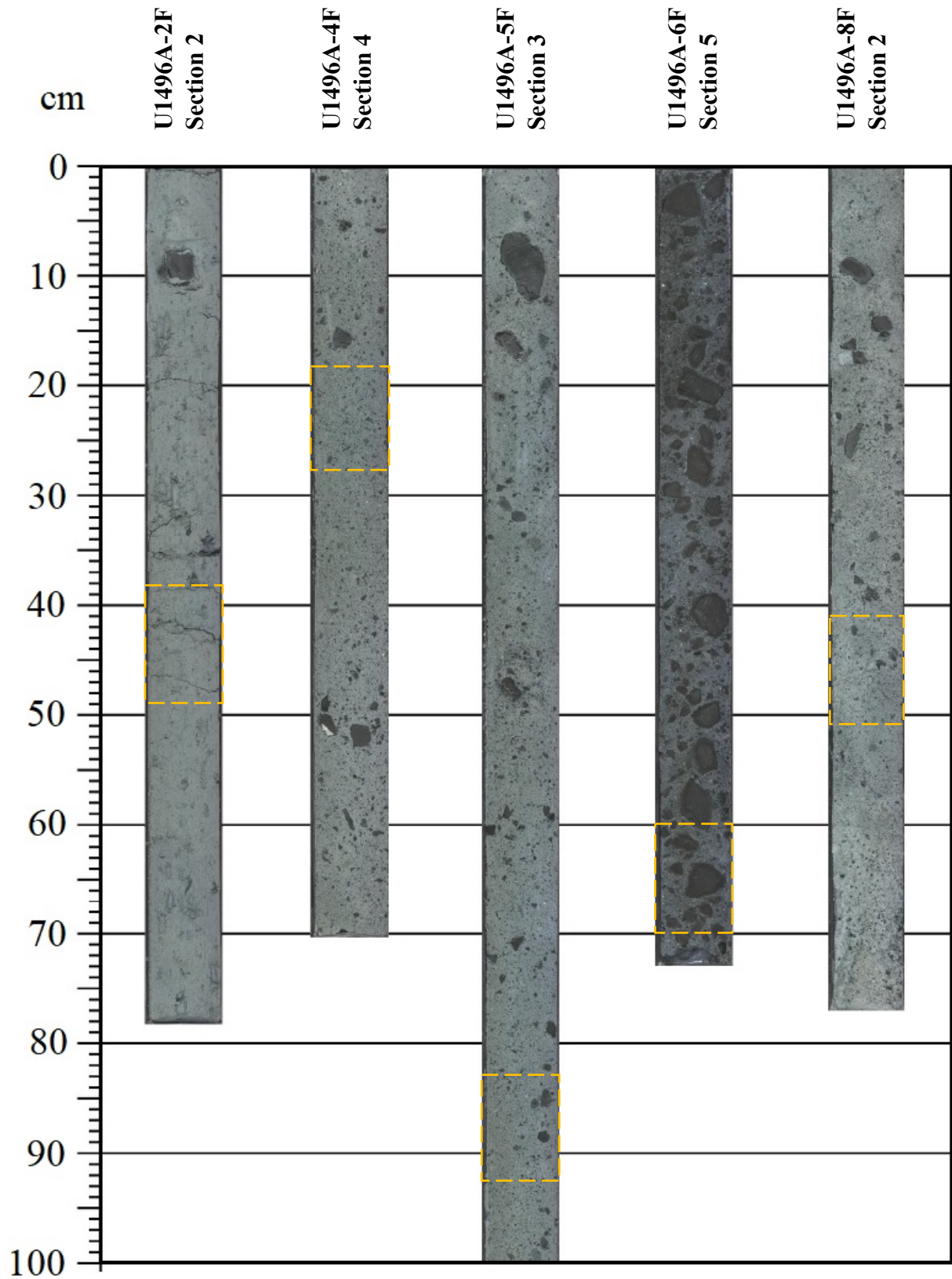
Fig. 13: Compilation of the sampled sections from borehole U1496A. Sample size shown in orange squares. Core pictures from Fryer et al. (2017).
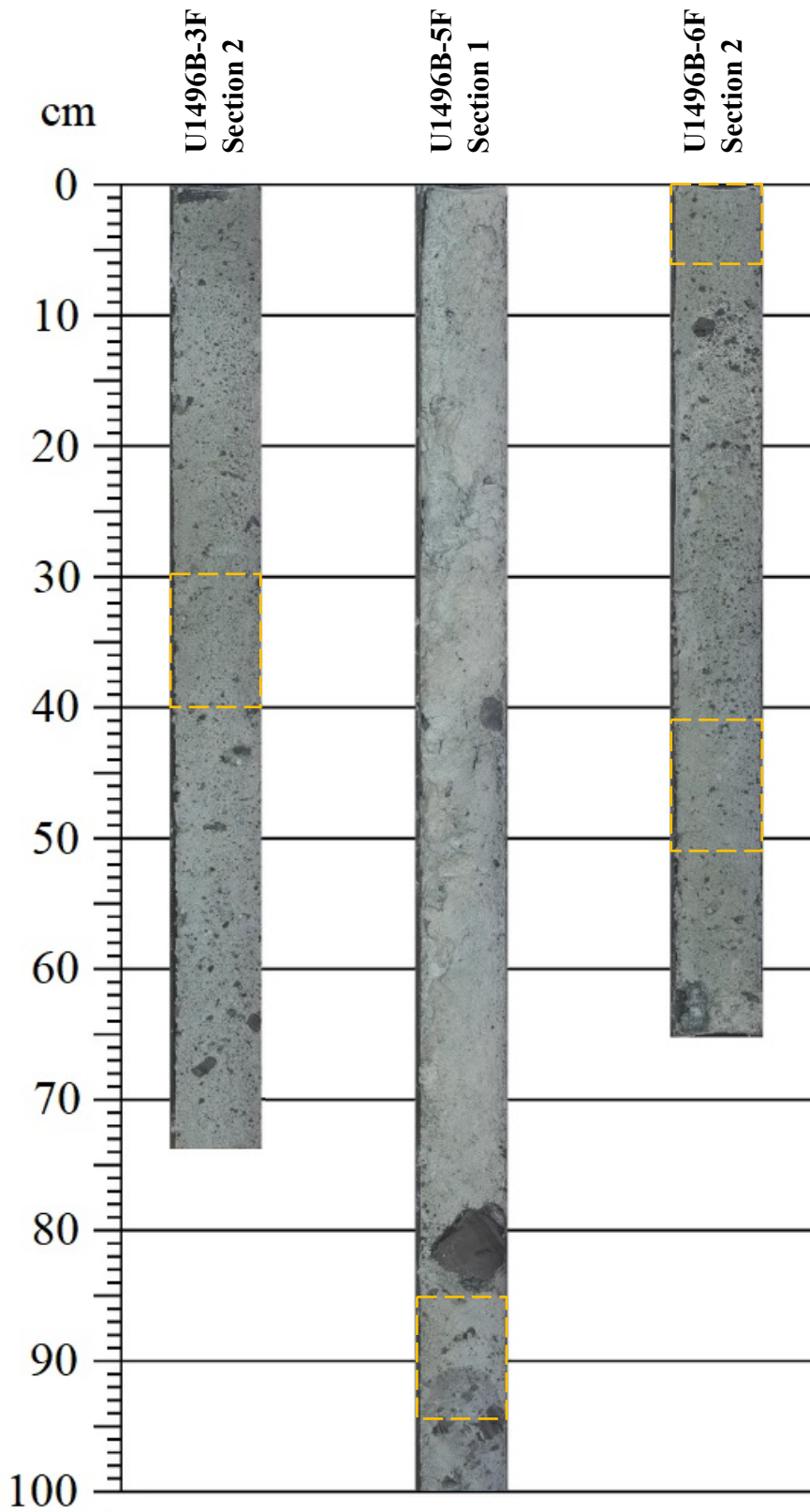
Fig. 14: Compilation of the sampled sections from borehole U1496B. Sample size shown in orange squares. Core pictures from Fryer et al. (2017).

4.2 Mineralogy

This chapter documents the mineralogical investigations and findings from Raman spectroscopy and X-ray powder diffraction (XRD) studies of the prepared serpentine mud samples from Asút Tesoru seamount. The investigations comprise data from analyses of 27 bulk XRD diffractograms and more than 310 Raman spectra from single mineral measurements.

4.2.1 Carbonates

Aragonite
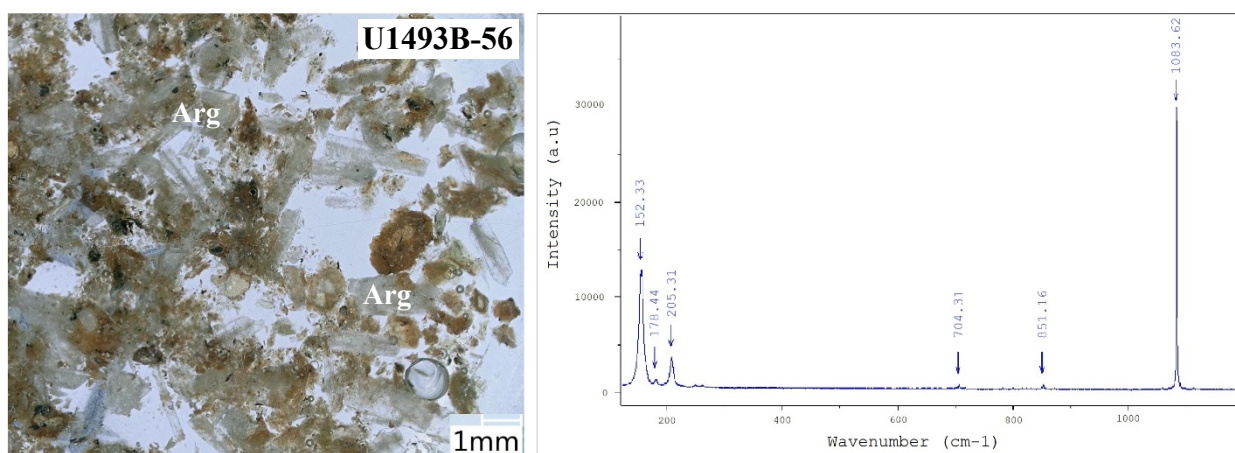
Fig. 15: Photomicrograph of Sample U1493-56 with selected Raman spectrum of an aragonite (Arg) crystal.

Sample U1493B-56 is composed of pelagic clayey serpentine mud with abundant aragonite needles, confirmed by Raman spectroscopy and XRD bulk measurements. Comparison of the Raman data with the Institute's and RRUFF project database displays distinctive peaks for aragonite at around 153, 206 and 1084. The aragonite minerals show colorless transparent to greyish-yellow color and acicular elongated prismatic crystals.

Calcite
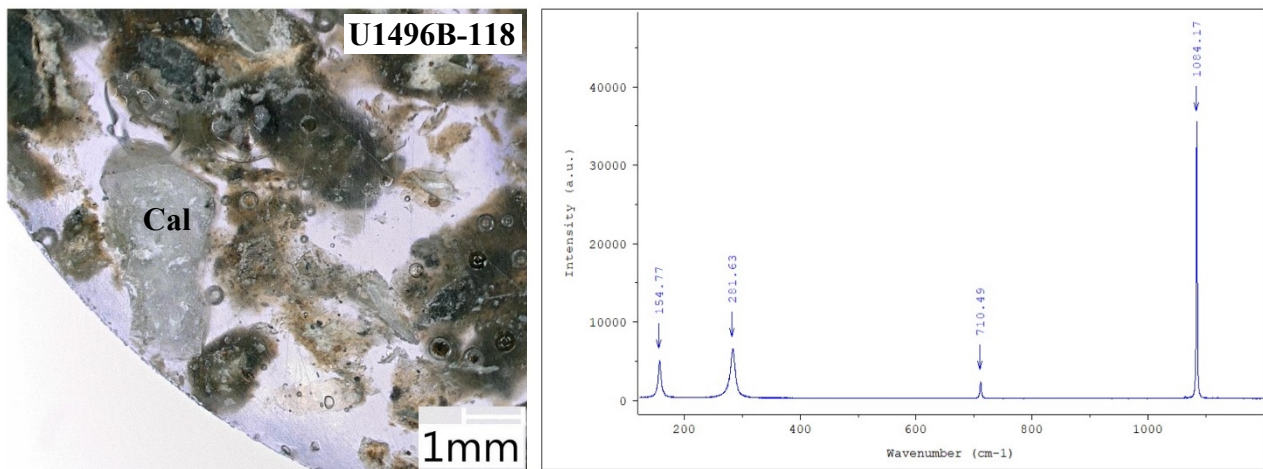
Fig. 16: Photomicrograph of Sample U1496B-118 with selected Raman spectrum of the displayed calcite (Cal) crystal.

Except for the pelagic cover (U1493B-56), only sample U1496B-118 show the presence of crystalline carbonates, or more precisely, calcite. Noticeable is the idiomorphic prismatic (or scalenohedral) crystal habit with distinct cleavage, although smear slide analysis showed mostly anhedral carbonate fragments in the mud material. The Raman spectrum displays clear peaks around 155, 202, 710 and 1084, and is thus distinguishable from aragonite. The mineral shows a milky-greyish color with a pearly luster.

4.2.2 Spinel Group Minerals

Chromite
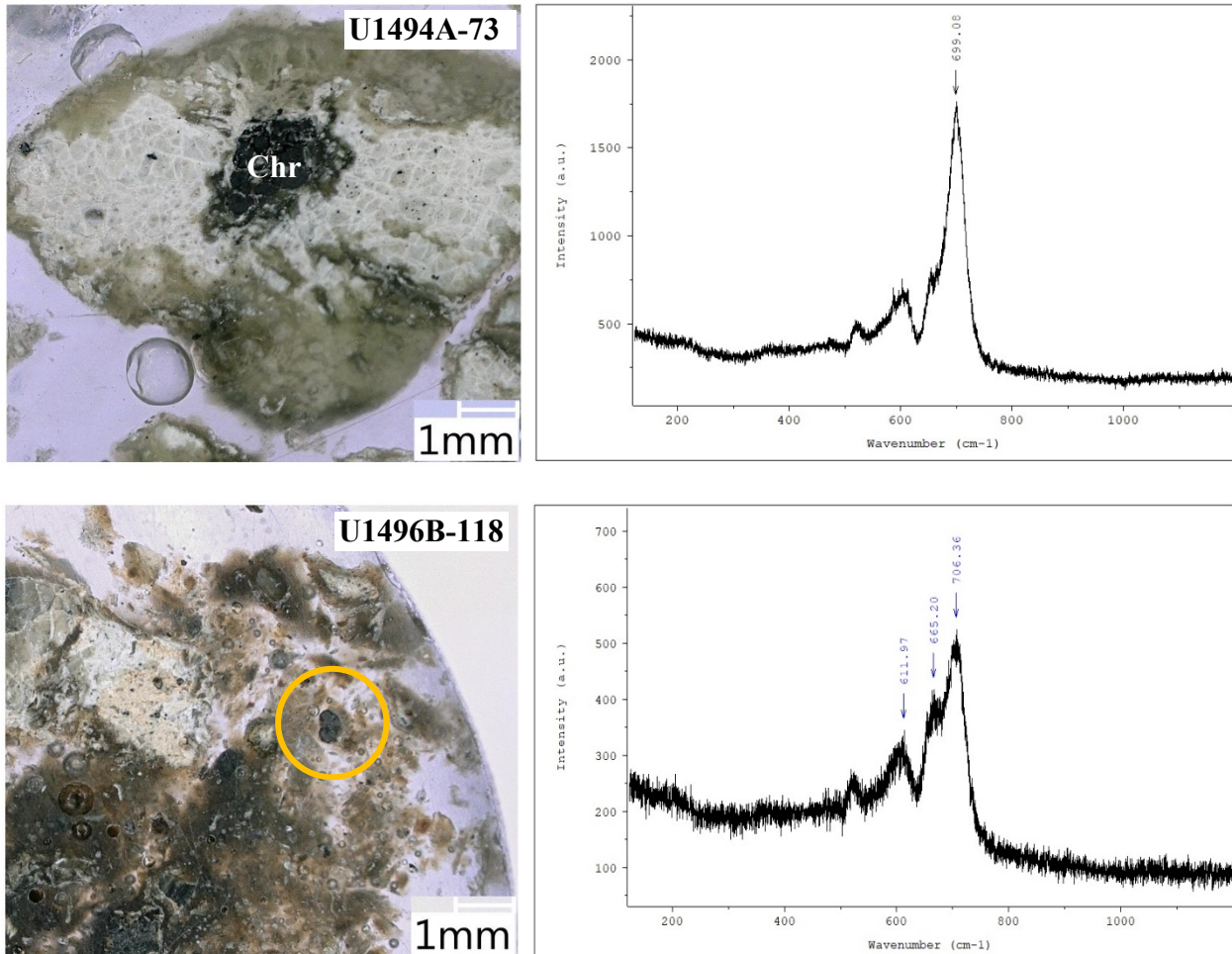
Fig. 17: Photomicrographs of Samples U1494A-73 and U1496B-118 with Raman spectra of chromite (Chr) crystals (orange circle).

Some samples show anhedral chromite, and as an alteration-resistant common mantle mineral its scattered commonness at Asút Tesoru seamount seems natural. The mineral phase was verified by Raman spectroscopy, since it is nearly indiscernible from magnetite at XRD diffractograms. The analyses indicated a main peak at about 700, with secondary peaks at around 660 and 610. Measured against comparison data (Spectral-ID, RRUFF project) showed a strong dependency of the peak positions from the chemical composition and ergo from the dominant endmember.

Same as magnetite, chromite belongs to the spinel group, which means that the minerals can form a complete solid solution series with other endmembers like spinel (sensu stricto, $MgAl_2O_4$), magnesiochromite ($MgCr_2O_4$) or hercynite ($FeAl_2O_4$) (e.g. Biagioni and Pasero, 2014).

Chromite minerals from Asút Tesoru are commonly fine granular (<2 mm) and show no cleavage or crystal face, although chromite is isostructural with magnetite. This suggests that, unlike magnetite, the chromite minerals originate from protolith mantle rocks. Most of the found grains show irregular fracturing with intergrowth of serpentine minerals. The color varies from brown to black with metallic luster.

Magnetite
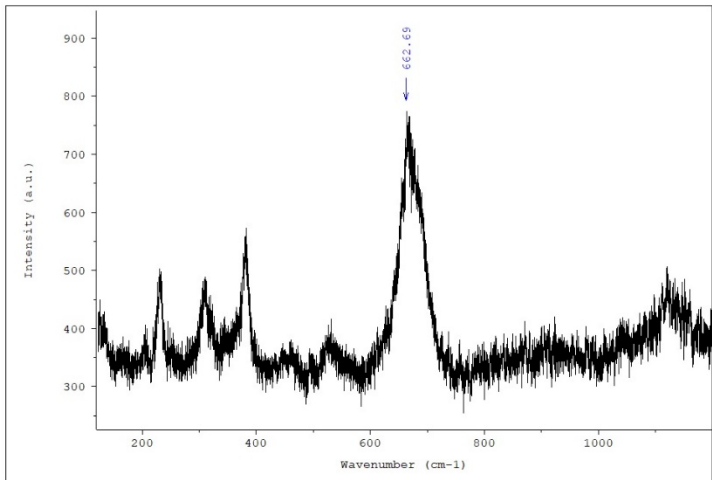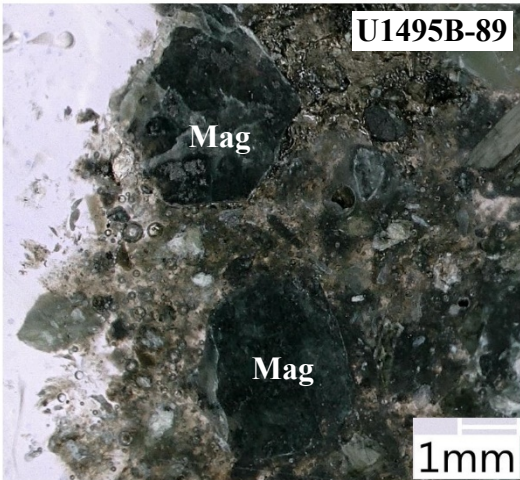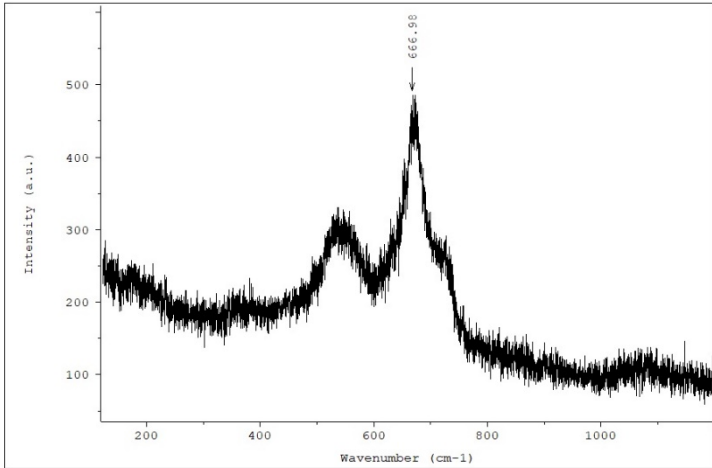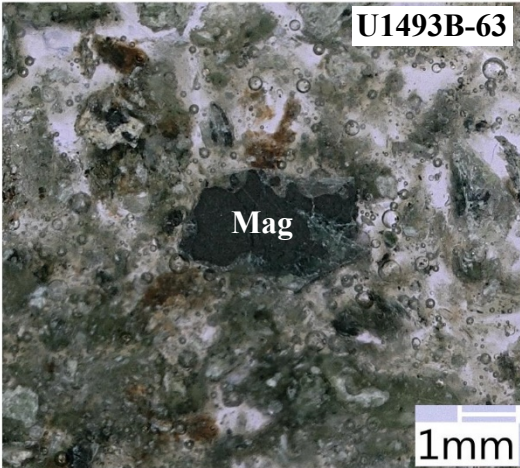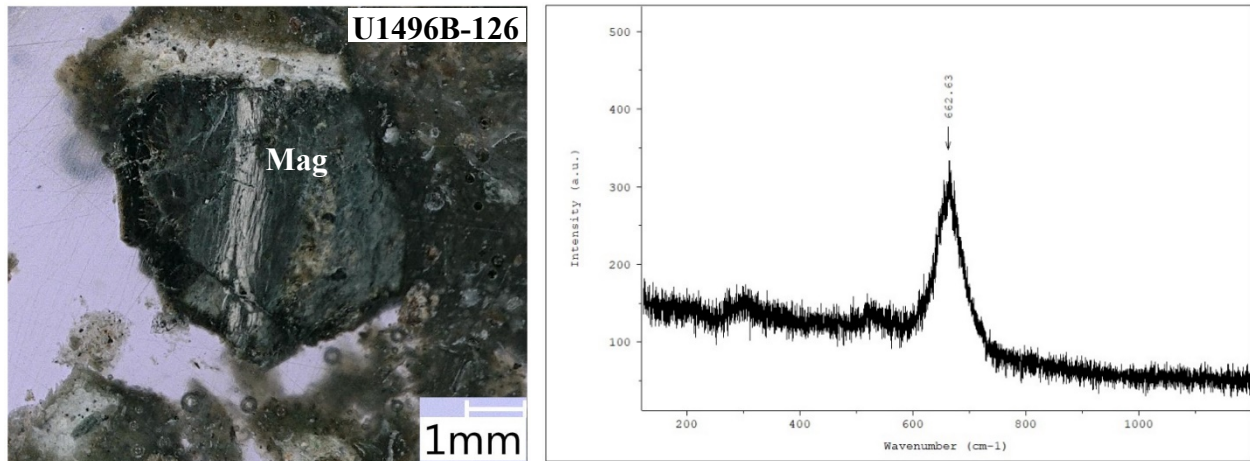
Fig. 18: Exemplarily photomicrographs of magnetite (Mag) grains from Samples U1493B-63, U1495B-89 and U1496B-126 with Raman spectra.

Analyses unveil that almost all samples contain magnetite crystals, although the grain size can greatly vary, from <1 mm to more than 5 mm. Comparison of 33 Raman spectra from magnetite single grains with databases show a characteristic main peak in the area between 660 and 670 with a second diffuse and less prominent peak between 500 and 600. It seems that variation in chemical composition can cause a shift of the peak position. Most commonly magnetite minerals show greyish-black color with metallic luster and idiomorphic rhombic-dodecahedra shape, but also fragmented and anhedral crystals could be observed.

4.2.3 Serpentine Minerals

Three polymorphs of serpentine minerals were found in samples from Asút Tesoru seamount: chrysotile, lizardite and antigorite. In many cases, XRD and Raman analyses of the cryptocrystalline mud groundmass showed a mixture of several serpentine minerals, complicating a distinct differentiation. In addition, serpentines substituted protolith minerals, resulting in bastite (after pyroxene) and mesh (after olivine) textures, partly with incomplete alteration which can lead to composite spectra.
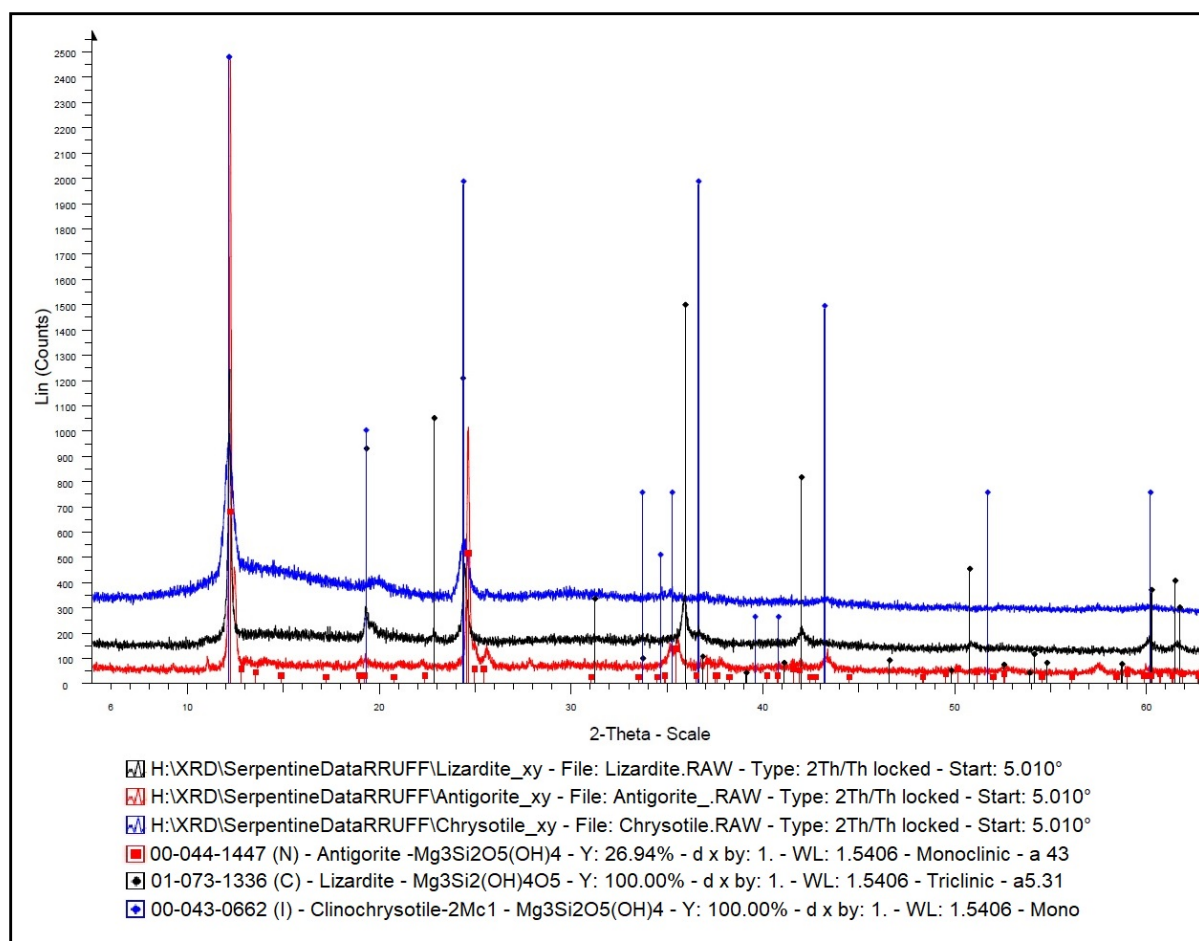
Fig. 19: Compilation of reference data from RRUFF project database (Lafuente et al., 2015) showing XRD diffractograms of chrysotile, lizardite and antigorite.
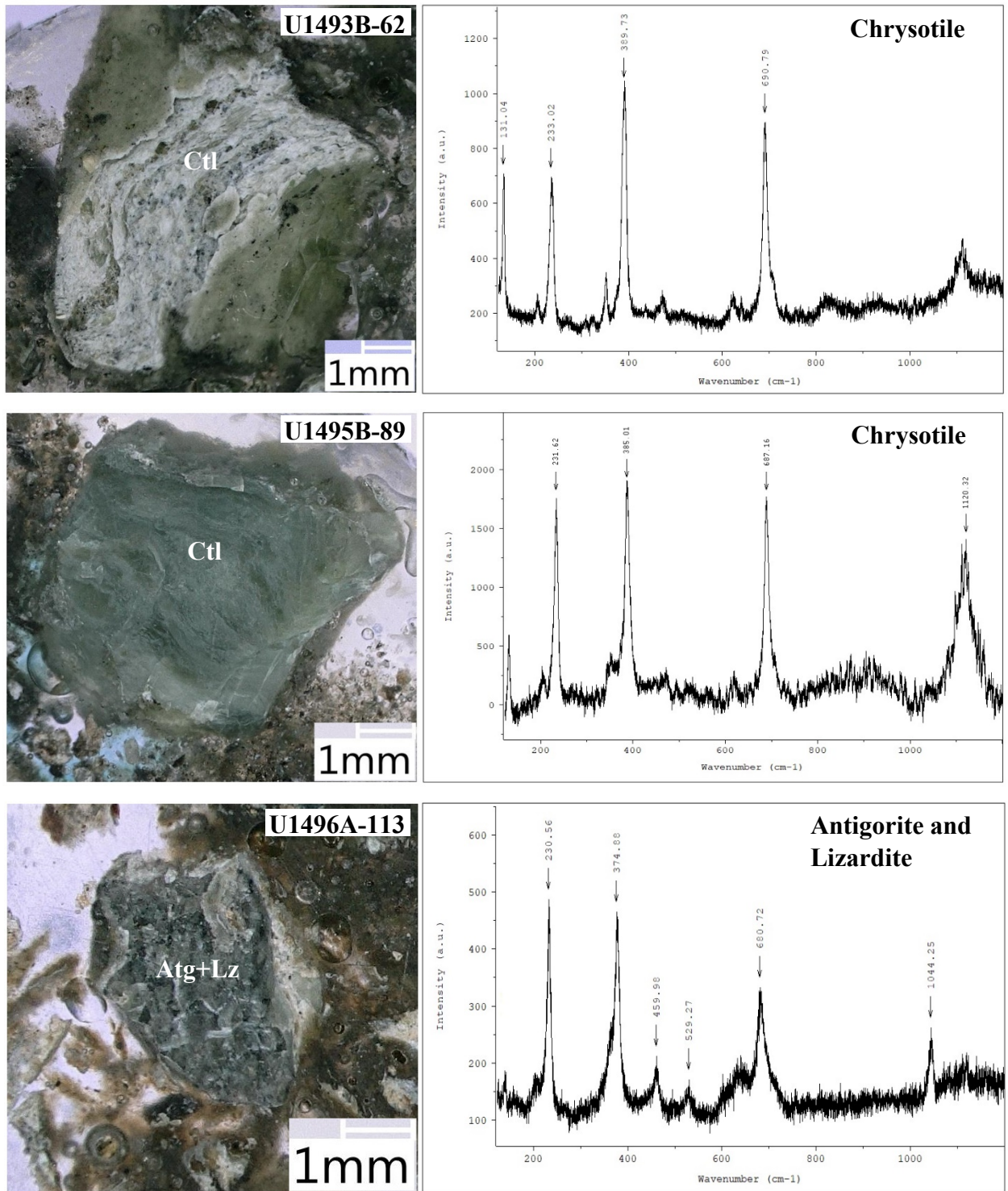
Fig. 20: Photomicrographs of Samples U1493B-62, U1495B-89 and U1496A-113 with Raman spectra of the different serpentine minerals. Mineral abbreviations: Ctl=chrysotile, Atg=antigorite, Lz=lizardite.

Sample photographs and Raman spectra are just exemplified for the great variety of phenotypes the serpentine phases can form. The analyzed serpentine minerals have main peaks around 230, 380 and 690 in common. Chrysotile has distinctive secondary peaks at around 620 and 1100, whereas lizardite shows much higher intensity at 230. Contradistinctive, antigorite has unique characteristic peaks at around 650 and 1040. Different from the idealized comparison data of the RRUFF database, Raman measurements mostly yielded mixed spectra.
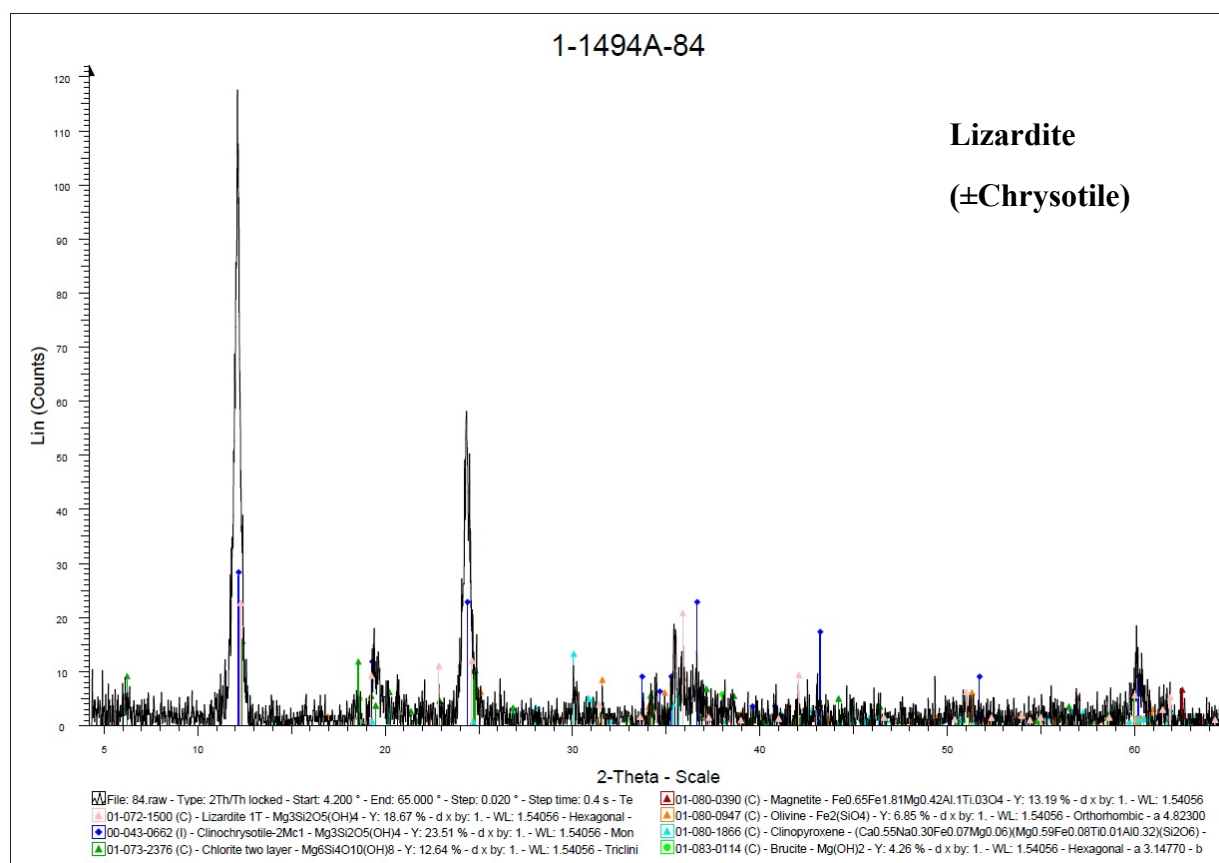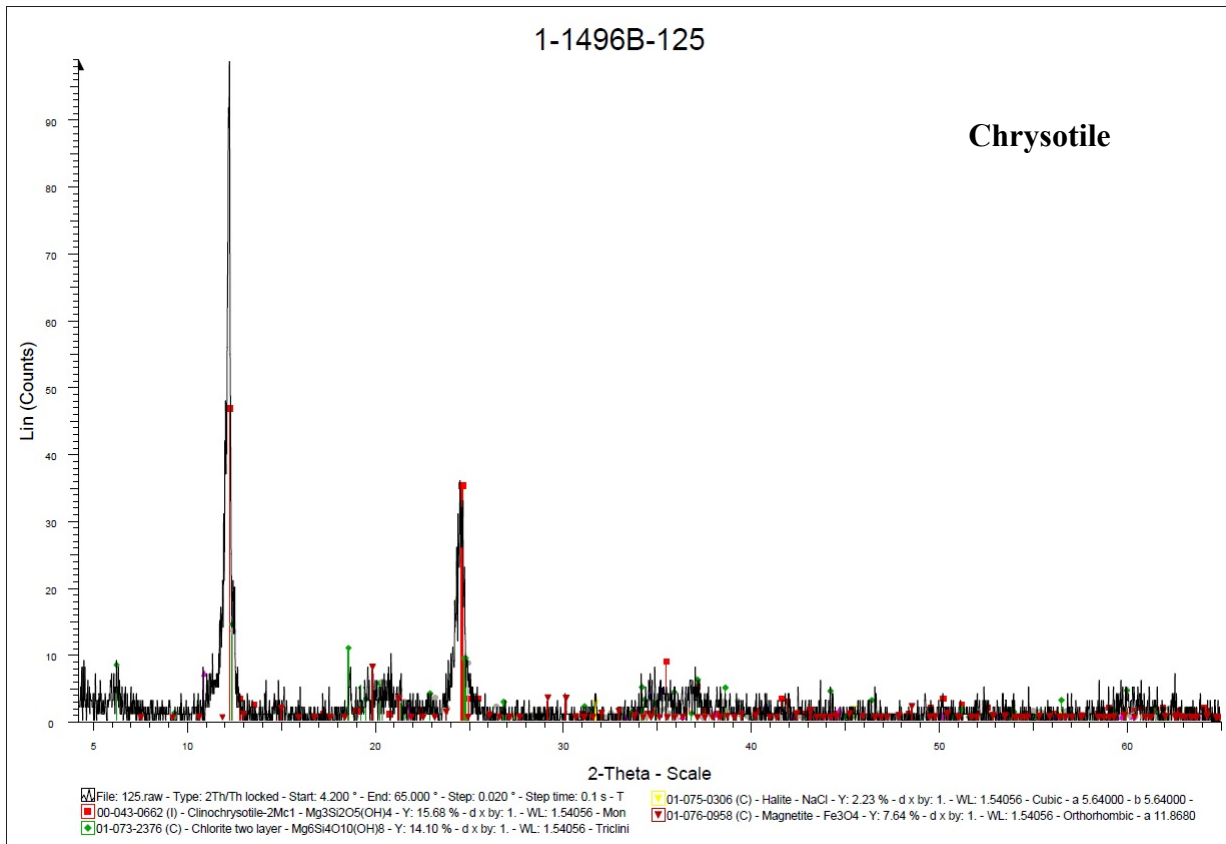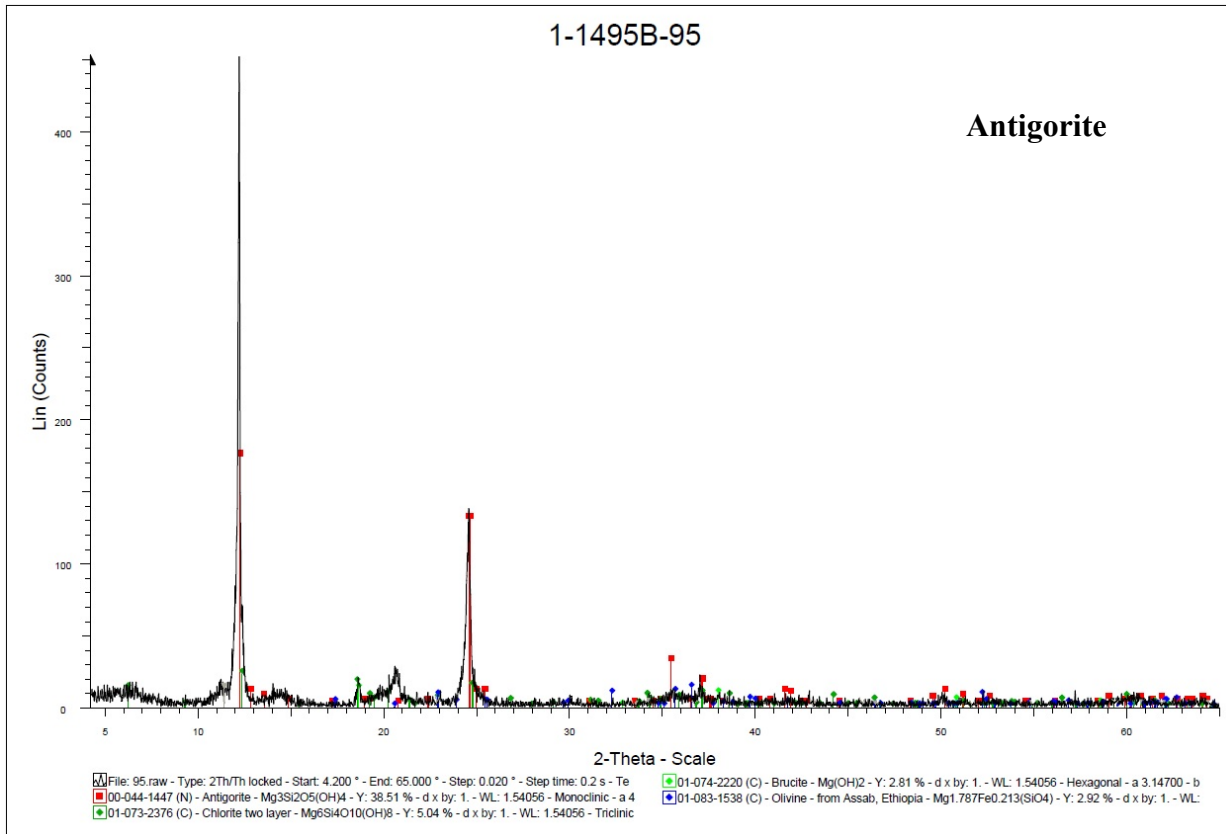
Fig. 21: XRD diffractograms are exemplary and show the varying dominance of serpentine phases in the bulk material and the subordinated concomitant mineral phases.

4.2.4 Other Phases

Iowaite
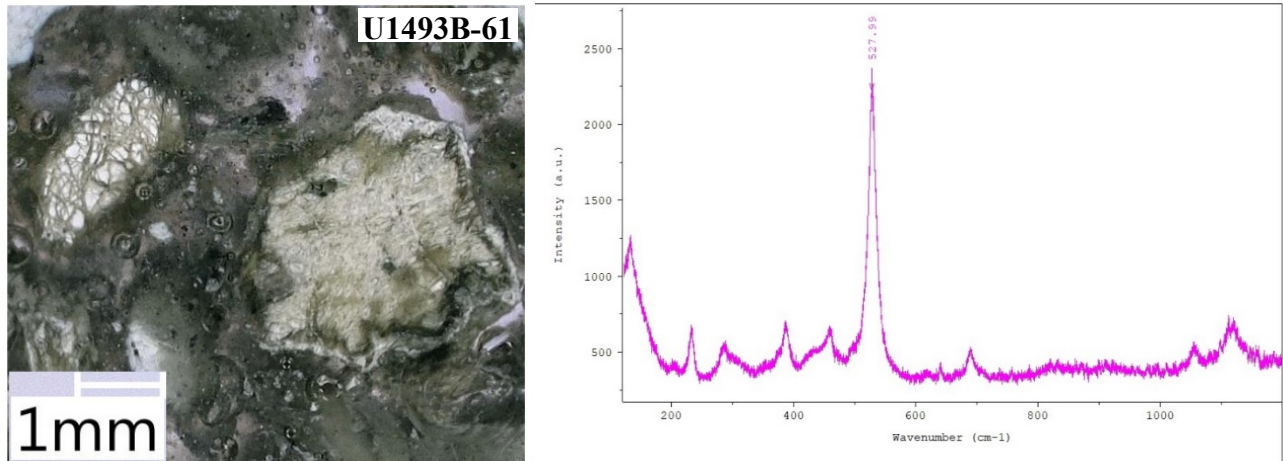
Fig. 22: Exemplarily photomicrograph of iowaite-bearing sample with Raman spectrum.

X-ray powder diffraction and Raman analysis unveiled the abundance of microcrystalline iowaite in samples from Asút Tesoru seamount. The mineral is too fine-grained for a determination by petrological microscopy, moreover mostly it is mixed with serpentine mud. Thus, the Raman spectra show a wide range of peak positions for bulk material analysis, even at high magnification and intensity. Iowaite may be evidenced at least as traces in almost all samples from the flank sites (U1493, U1494, U1495), except the samples originate from the summit site (U1496). Raman data revealed that samples U1493B-61, U1494A-74, and U1495B-89 contain almost pure phases. The most distinctive main peak is at around 525, with secondary peaks at about 280, 390 and 1060. According to Frost et al. (2005), air oxidation of iowaite can shift peaks and cause additional bands at 484 and 547.
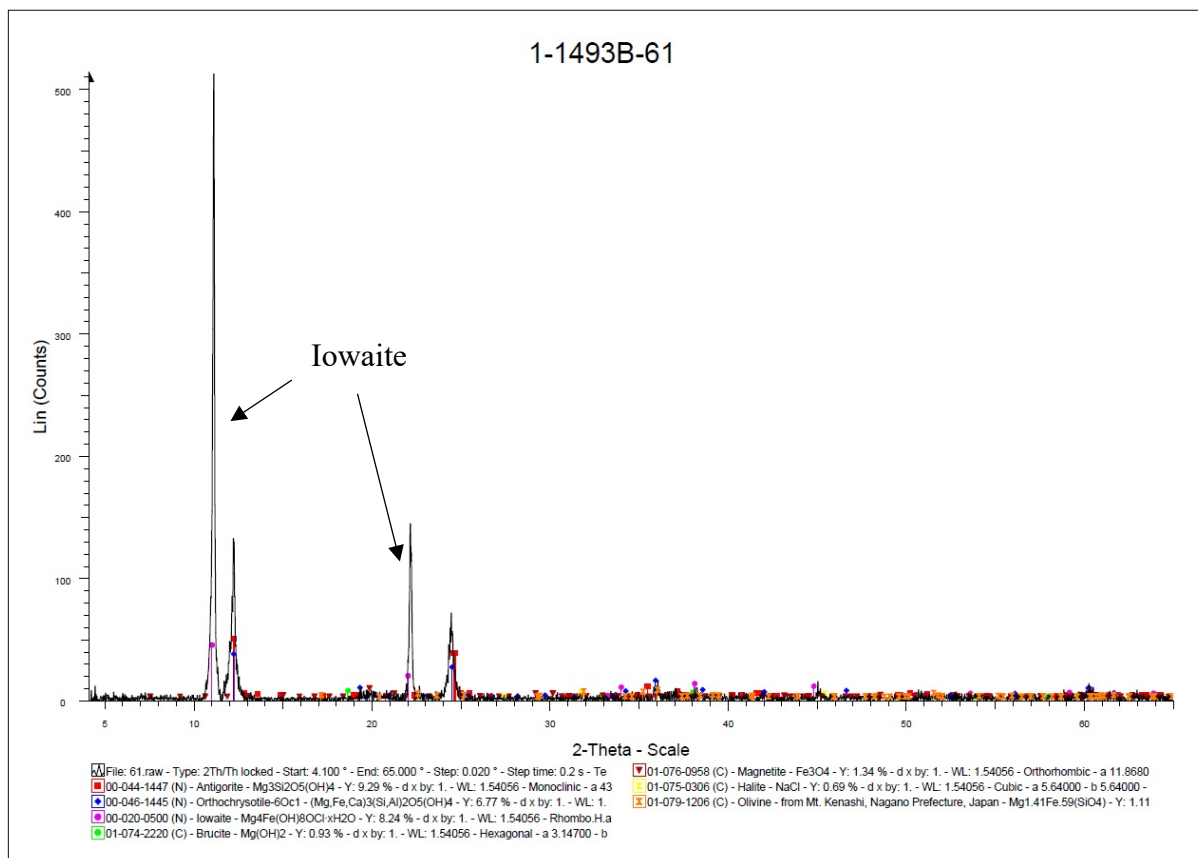
Fig. 23: XRD diffractogram of Sample U1493B-61 with marked iowaite peaks.

Powder diffraction analyses showed the occurrence of iowaite in 11 out of 18 flank samples but in none from the summit site. The mineral is abundant in material taken from the upper part of the drill core and decrease with sampling depth, according to the peak intensities of the diffractograms. This relation could be observed at samples from cores U1493B, 1494A and U1495B.

Fig. 24: Decrease in iowaite proportion with depth, peak intensity marked with black arrows.
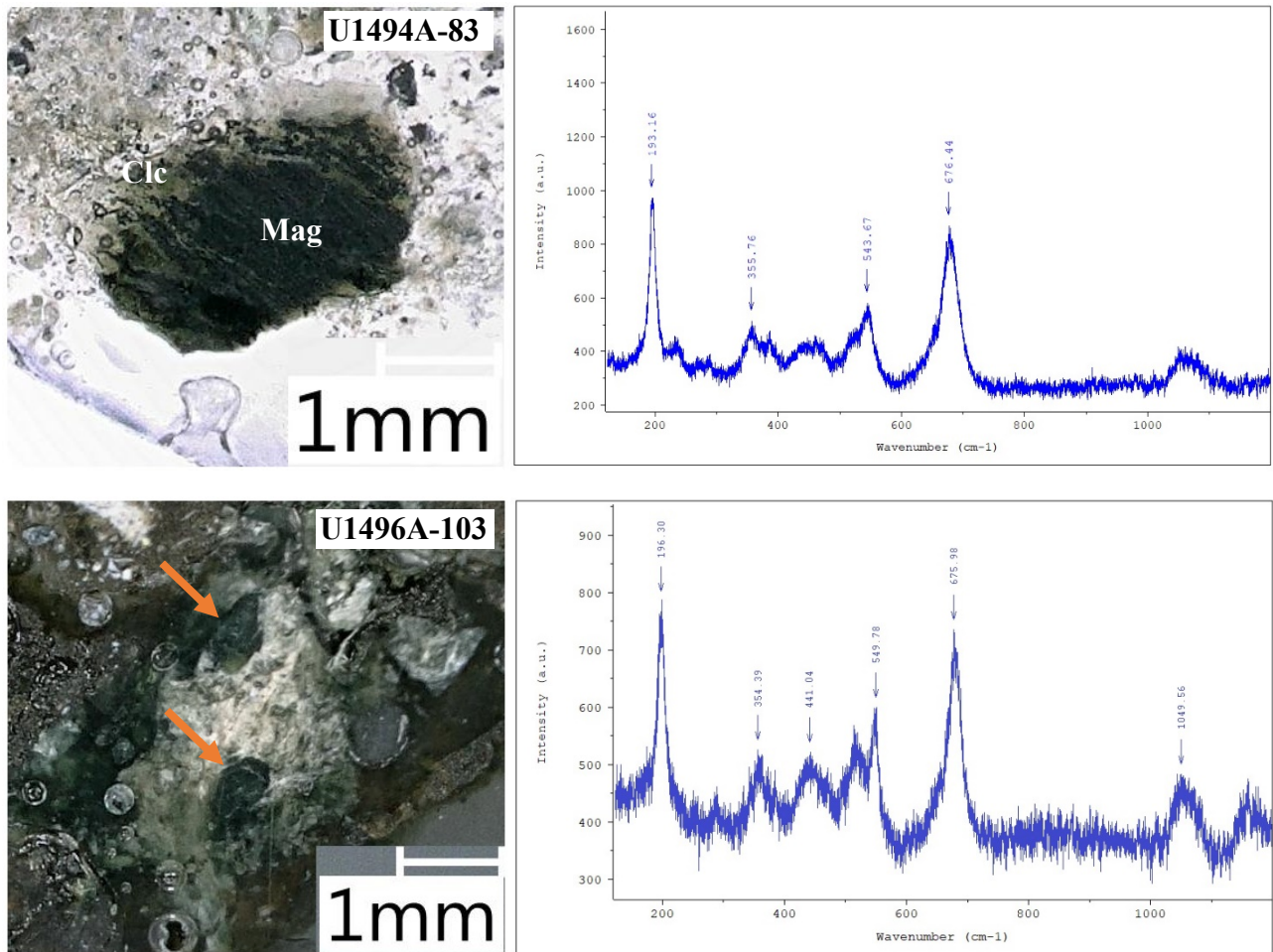
Clinochlore

Fig. 25: Photomicrographs of clinochlore (Clc) minerals with Raman spectra.

Another abundant mineral phase within most samples is clinochlore, a member of the chlorite group. Clinochlore is typically a product of hydrothermal alteration of mainly ferromagnesian mafic minerals such as amphibole, pyroxene and biotite (Strunz and Nickel, 2001).

Investigations of the samples by optical microscopy and Raman spectroscopy showed flaked crystals within the serpentine mud but also intergrowth, coatings, or the formation of pseudomorphs after protolith minerals. The mud-based dispersed single grains show prevalent idiomorphic pseudohexagonal crystal shape with blackish to olive green color and vitreous luster. Raman spectroscopy showed distinctive main peaks at around 195, 355, 545 and 670-680. In some cases, measurements of secondary clinochlore from pseudomorphs showed combined spectra with signals of the primordial mineral.

Andradite
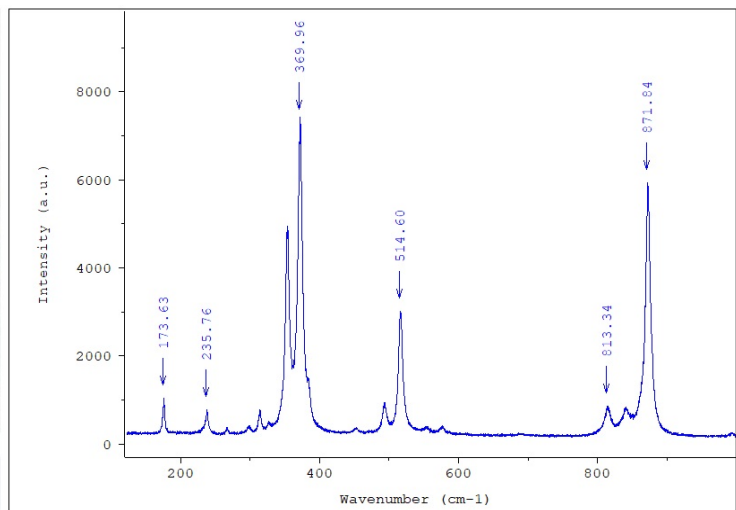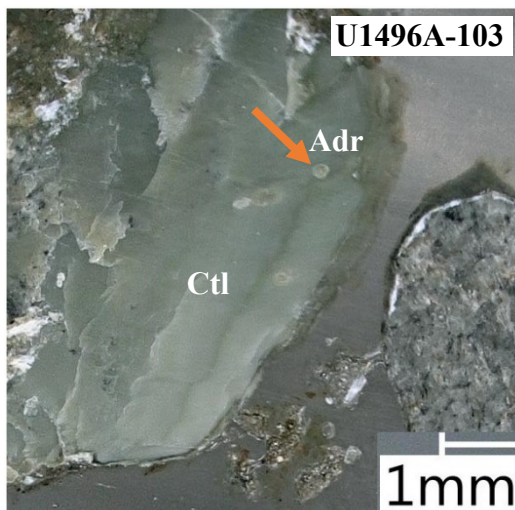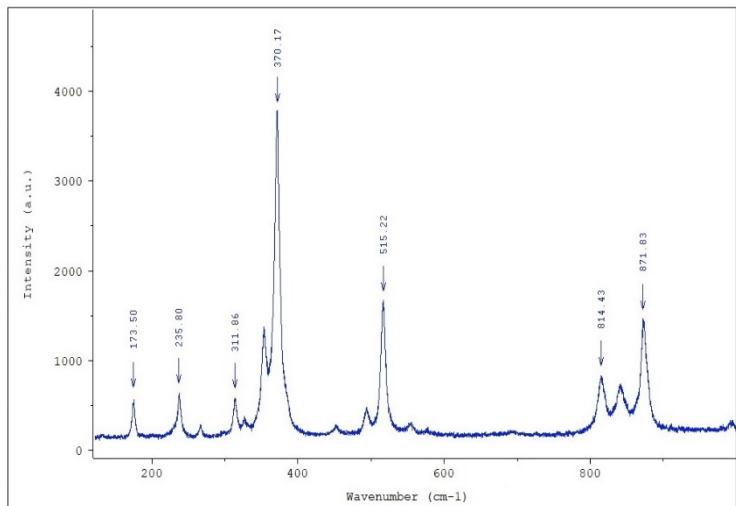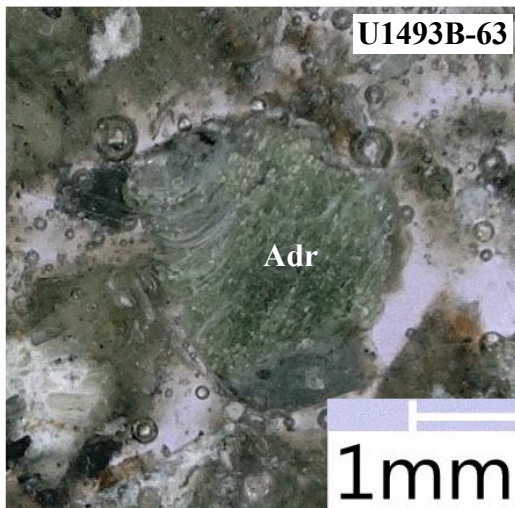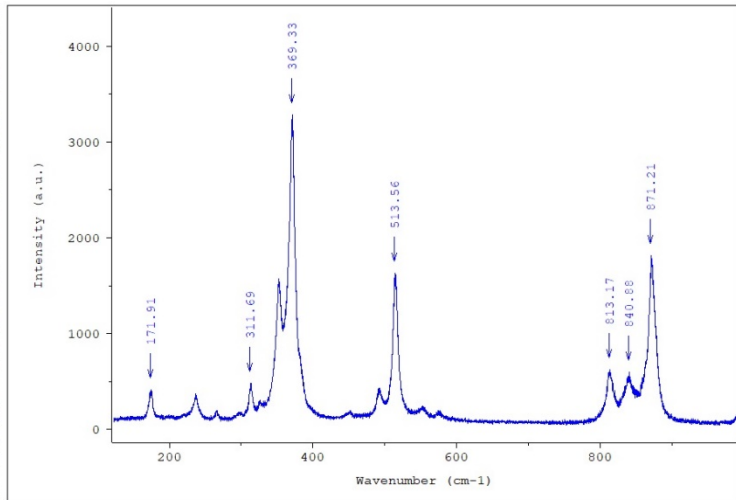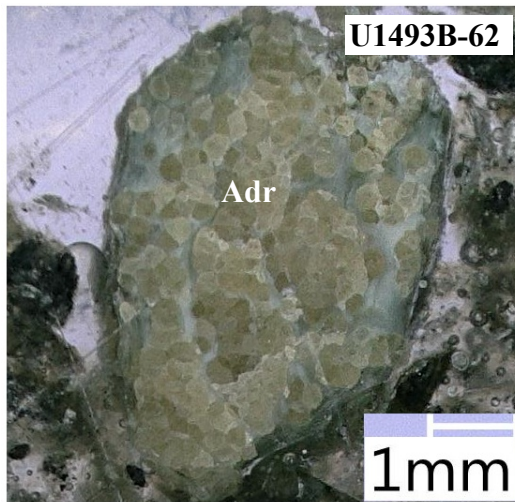
Fig. 26: Photomicrographs of Samples U1493B-62, U1493B-63 and U1496A-103 with Raman spectra of containing andradite (Adr) minerals.

In samples from drill cores U1493B (flank/bottom) and U1496A (summit) andradite was found, confirmed by optical microscope observations and Raman spectroscopy. When andradite was found in a sample, it was abounding, whereas wide sections show no indication for the mineral. In general, crystals from the summit site are smaller and scattered within the mud, minerals from the flank site mostly form aggregates, often within bastite or mesh textures. Most of the granular andradite grains are irregularly shaped and thus not bounded by any characteristic (cubic) crystal faces. All minerals show no evidence for alteration, which implies that andradite is in equilibrium with the serpentinization environment. The color varies from yellowish to dark glass green with a glassy luster (where visible).

Andradite is the calcium- and iron-rich endmember of the garnet group with the idealized formula $Ca_3Fe_2Si_3O_{12}$. A substitution of chromium causes green, ferric iron yellow coloration of the garnet, producing (theoretically) the andradite variety demantoid (Grande and Austin, 2009).

Trace Phases

Several subordinate microcrystalline phases were identified by Raman spectroscopy, commonly embedded within serpentine mud. Almost all spectra from serpentine mud indicate for the presence of brucite, likewise XRD diffractograms (see figure 21, 23, 24).
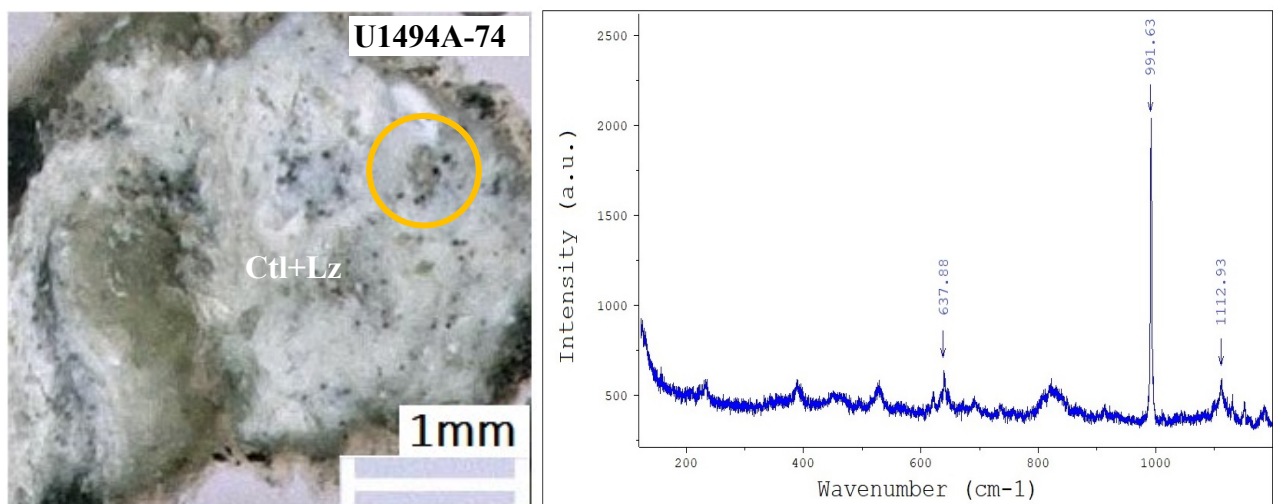
Fig. 27: Photomicrograph of Sample U1494A-74 with Raman spectrum of identified baryte crystal (orange circle). Ctl=chrysotile, Lz=lizardite.

In samples from core U1494A (74, 82) the mineral baryte could be identified, recognizable by the characteristic main peak at 991. According to the comparison data from RRUFF project database, there must be secondary less prominent peaks at around 450 and 630, here partly superimposed from serpentine mud bands.

4.2.5 Bulk Serpentine Mud and Pseudomorphs
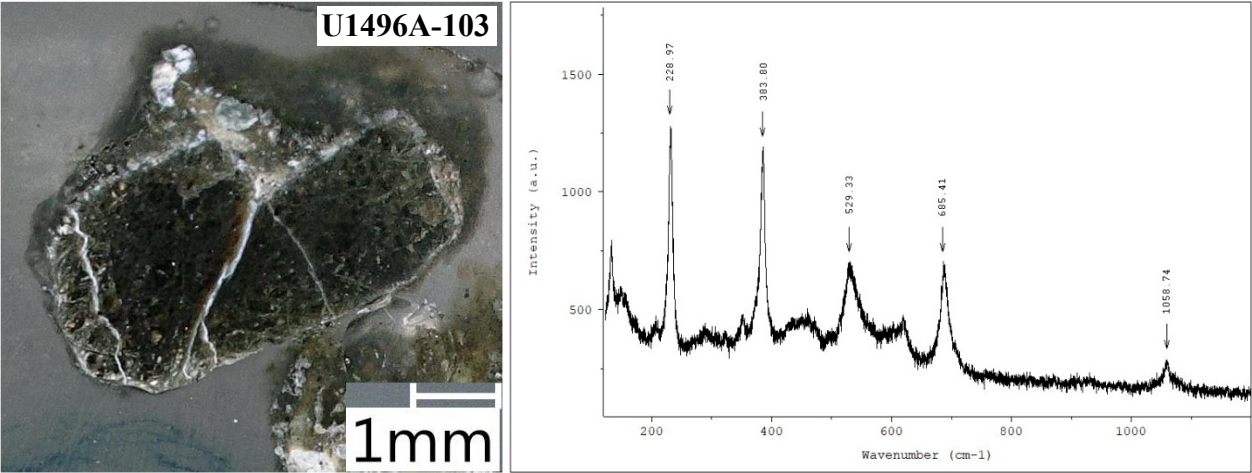
Fig. 28: Photomicrograph from Sample U1496A-103 with Raman spectrum of the pseudomorph mineral grain.
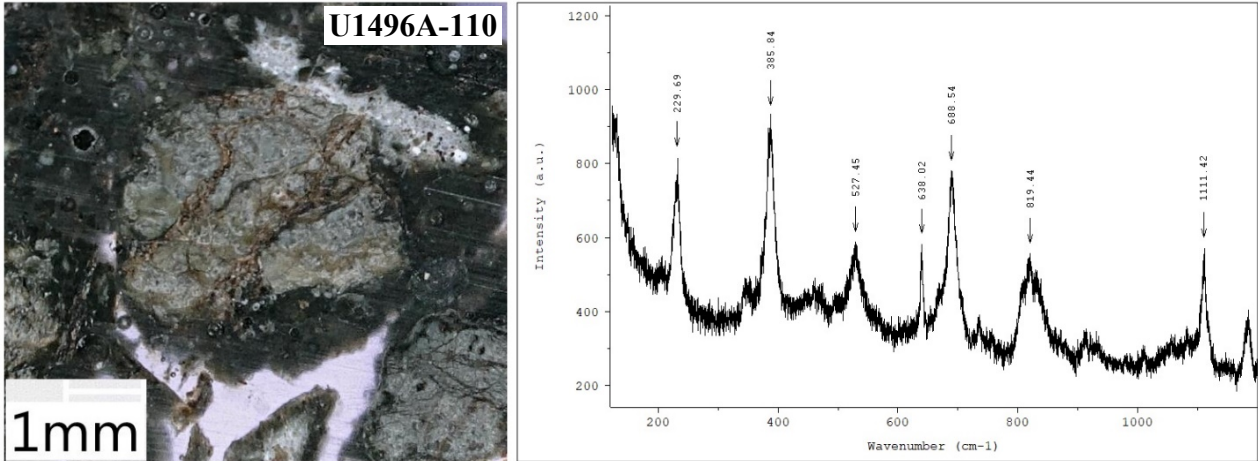
Fig. 29: Photomicrograph from Sample U1496A-110 with Raman spectrum.

Especially summit site samples (U1496A, B) contain abundant relict minerals and pseudomorphs. As can be seen from figures 28 and 29, most of the relict phases are affected from intensive chloritization and serpentinization. The original protolithic crystal shapes are preserved, whereas Raman spectra show mixed bands of secondary mineral phases. Figure 29 show exemplarily a relict olivine grain with a distinctive (olivine) band at around 820, superimposed by serpentine and chlorite mineral spectra. Example from U1496A-103 (Fig. 28) show a completely chloritized pseudomorph pyroxene grain with distinctive cleavage and crystal shape.
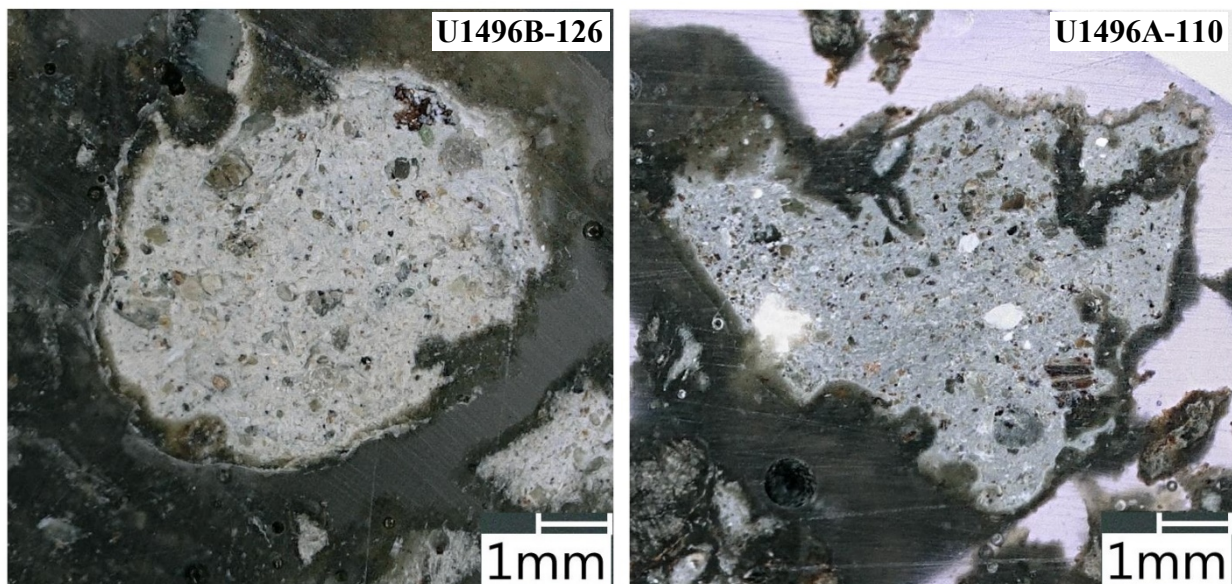
Fig. 30: Exemplarily photomicrographs of serpentine mud from Samples U1496B-126 and U1496A-110.

As apparent from figure 30, serpentine mud from the summit holes is composed of cryptocrystalline mud matrix mixed with various relict mineral fragments and hydrothermal alteration products. This "fresh" mud assemblage is indicative for summit site material, whereas mud samples from flank sites show a higher degree of serpentinization (see Fig. 20). Raman studies of the material yielded mixed spectra of primordial and secondary minerals.

4.3 Geochemistry and Mineral Chemistry

4.3.1 Whole Rock Geochemistry

To determine the bulk chemistry of the serpentine muds, seven representative samples from all drilling sites were analyzed using X-ray fluorescence analysis. An additional sample (K81-5) of medium serpentinized mantle rock, recovered by dredging during the *1981* cruise R/V Kana Keoki (KK) 81-06-26 by University of Hawaii, was also analyzed for depiction of progressive serpentinization with potentially element loss. The obtained data was compared and complemented with Expedition 366 reported and published literature data (Table 3). Diagrammed measurements include major element concentrations, displayed as oxides in weight percent (SiO_2, MgO, CaO, Al_2O_3, FeO_t, TiO_2, Na_2O, K_2O) and selected trace elements in parts per million (Ni, Cr).

Sample	Plotted*	Al2O3 (wt. %)	CaO (wt. %)	Fe2O3 (wt. %)	MgO (wt. %)	MnO (wt. %)	Na2O (wt. %)	SiO2 (wt. %)	TiO2 (wt. %)	K2O (wt. %)	Ni (ppm)	Cr (ppm)	V (ppm)	Co (ppm)	LOI	Total
1493B-5F-3W	x	0.77	0.58	8.06	45.09	0.12	0.37	43.43		18	3341.22	2990.54		125		**98.33**
1493B-9X-1W		0.76	0.06	9.93	47.48	0.2	0.02	37.77		9	3081.34	3120.45	34	115		**96.11**
1494A-1F-2W		0.17	8.75	8.36	39.67	0.09	0.46	40.64		12	2472	1603		82	18.59	**97.35**
1494A-2F-1W	x	0.49	0.64	7.95	46.58	0.09	1.04	43.94		32	2515	1987		106	17.06	**100.6**
1494A-3F-2W	x	0.62	0.81	7.62	44.87	0.09	0.57	45.04		0.02	2481	2238		100	14.96	**99.75**
1494A-6F-2W	x	0.58	0.79	7.38	45.59	0.13	0.26	44.23		5	2611	2285		101	15.34	**98.92**
1494A-9G-CC	x	0.74	0.05	7.98	44.61	0.12	0.35	45.24		11	2867	2984	36	108	14.17	**99.5**
1494A-10F-1W		0.33			42.42		0.29	47.37		25			37		14.13	**98.53**
1494A-10F-2W	x	0.97	0.07	8.59	44.82	0.14	0.22	43.97	0.0035	0.01	3186	2925	43	122	13.72	**99.4**
1495A-1F-1W		0.22	13.22	7.07	39.18	0.08	0.32	40.17		58	2667	1894			19.75	**99.71**
1495B-2F-1W	x	0.22	1.9	7.24	46.34	0.1	0.48	45.16		0	2141	2002		85	14.48	**101.3**
1495B-2F-3W	x	0.59	1.36	8.05	46.69	0.15	0.33	41.33		9	2982	2037		103	15.47	**99.01**
1495B-4F-3W	x	0.52	0.35	7.74	46.02	0.13	0.5	43.65		17	2599	2298	23	105	14.03	**99.03**
1496A-2F-4W	x	0.84	0.64	7.92	44.66	0.12	1.18	44.71	0.0246	38	2614.59	2189.66	25	102	14.07	**101.2**
1496A-4F-1W	x	1.01	0.6	7.82	45.69	0.13	1.34	45.05	0.0375	48	2496.04	2348.64	27	103	12.14	**101.8**
1496A-6F-2W		1.33	0.7	8.43	45.96	0.14	1.33	43.61	0.0984	77	2751.54	2417.49	32	105	14.92	**101.8**
1496A-6F-5W	x	0.37	0.17	8.55	46	0.13	0.89	44.24		39	2548.49	1972.11		110	15.05	**100.2**
1496A-7F-4W	x	1	0.96	7.81	45.74	0.12	0.77	45.19	0.0453	33	2543.41	2266.99		103	13.72	**101.7**
1496A-8F-4W	x	1.01	0.85	7.81	45.31	0.13	2.05	44.26	0.0391	73	2494.31	2585.51		100	16.02	**101.5**
1496A-103	x	0.86	0.67	8.22	44.45	0.118	0.99	43.26	0.05	0.04	2405	2531	26		13.89	**98.66**
1495B-95	x	0.60	0.71	8.00	45.32	0.111	0.43	42.94	0.02	0.02	2419	2614	27		14.01	**98.15**
1495B-89	x	0.63	0.86	7.75	44.72	0.102	0.26	44.15	0.02	0.01	2118	2420	28		13.56	**98.49**
1494A-81	x	0.49	0.00	8.30	45.66	0.087	0.34	43.61	0.01	0.01	2661	2759	27		13.99	**98.52**
1494A-79	x	0.69	0.48	8.39	44.62	0.094	0.38	43.85	0.01	0.02	2116	2397	27		13.82	**98.53**
1493B-63	x	0.54	0.87	7.49	44.50	0.099	0.37	44.89	0.01	0.02	1791	2111	<20		13.34	**98.79**
1493B-61	x	0.41	0.05	8.20	47.36	0.064	0.53	41.84	0.01	0.02	2492	2257	23		16.02	**98.49**
K81-5	x	0.69	2.75	8.88	42.33	0.111	0.12	43.82	0.01	0.01	2578	3083	39		11.88	**98.73**

Tab. 3: Representative bulk analyses of the serpentine muds from Asút Tesoru seamount (except K81-5). Samples in bold type are analyses from this work, others from IODP data base (2017). Major oxides in wt. %, trace elements in ppm. [*: see Fig. 32].
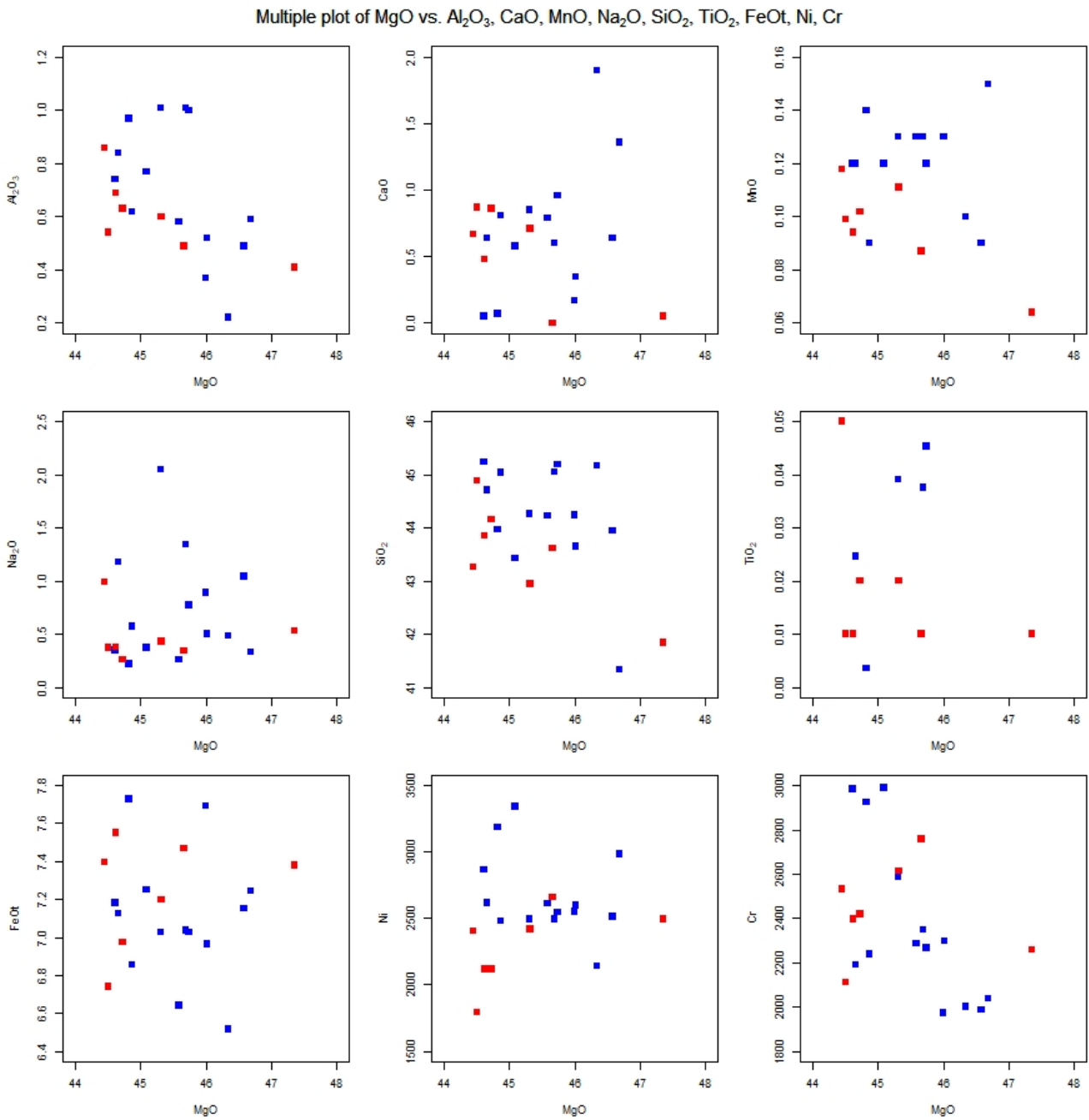
Fig. 31: Major oxides (in wt. %) plus trace elements Ni and Cr (in ppm) plotted against MgO. Red dataset represents the analyses from this study, blue the shipboard laboratory measurements (see Tab. 3) from Asút Tesoru serpentine muds.

The diagrams (Fig. 31) indicate a distinct negative trend correlation for Al2O3 and Cr and a slight positive trend for Na2O and Ni (±TiO2). The other data points do not show any trends or significant correlations, thus allow no definite conclusions. The Al2O3 content is typically a benchmark for the mantle's fertility. Commonly, depleted mantle contains between 2 and 4 wt.

% of Al$_2$O$_3$, decreasing by continuous magma production and extraction with the associated loss of clinopyroxene due to melting (Frost and Frost, 2014). Therefore, CaO and TiO$_2$ concentrations should usually follow this depleting trend, the related data plots, however, are ambiguous.

Separate diagrams of drilling sites from Asút Tesoru (see appendix) show a slightly increased value of Na$_2$O (and ±Al$_2$O$_3$) for samples from the summit site (U1496A), while others are homogeneously distributed and show no significant preferences.

Multiple plot of SiO2 vs. FeOt, Ni, Cr
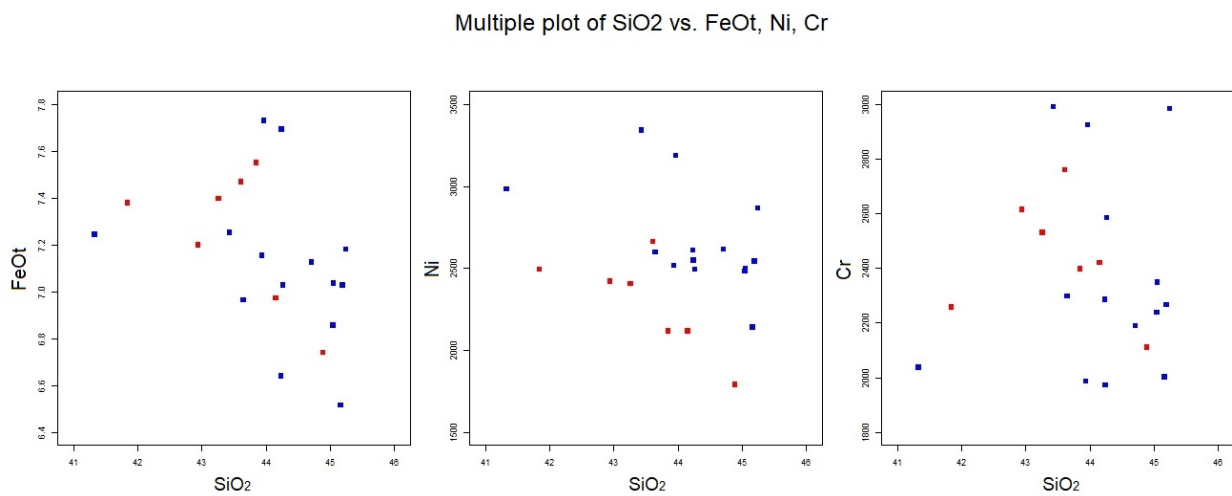
Fig. 32: Plotted data (Tab. 3) from Asút Tesoru serpentine muds, represented as FeO$_t$ (in wt. %), Ni and Cr (in ppm) versus SiO$_2$. Red dataset represents the analyses from this study, blue the shipboard laboratory measurements.

The diagrams show prominent negative trends with increasing SiO$_2$ content, combining this observation with trends versus Al$_2$O$_3$ and CaO (not displayed), coherences, especially for Cr can be obtained. Cr shows no distinctive correlation to Ca content, Fe a clear negative trend, but both rise with an increase in Al, while Mg ensues a clear negative trend. In combination with other insights this suggests that the major Cr-bearing phase is relict chromite or a magnetite solid solution. Additionally, andradite could act locally as a sink for Cr, forming an uvarovite-component.

Sample	Petrology	Colour	Al2O3 (wt.%)	CaO (wt.%)	Fe2O3 (wt.%)	MgO (wt.%)	MnO (wt.%)	Na2O (wt.%)	SiO2 (wt.%)	TiO2 (wt.%)	K2O (wt.%)	Ni (ppm)	Cr (ppm)
Mean Asút Tesoru	serp mud	red	0.664	0.639	7.95	45.459	0.113	0.65	43.999	0.0133	0	2544	2390
K81-5	serp rock	black	0.69	2.75	8.88	42.33	0.111	0.12	43.82	0.01	0.01	2578	3083
Salters & Stracke, 2004	depleted mantle	green	4.28	3.5	8.07	38.22	0.1045	0.29	44.9	0.19	0	1960	2500
McDonough & Sun, 1995	pyrolite models	blue	4.45	3.55	8.05	37.8	0.135	0.36	45	0.201	0.029	1968	2627
Allegre et al, 1995	primitive mantle	cyan	4.09	3.232	7.485	37.77	0.149	0.36	46.117	0.18	0.0337	2000	2700
Le Maitre, 1976	Dunites	magenta	1.69	1.15	12.82	39.37		0.17	40.43	0.22	0.07		
Le Maitre, 1976b	Harzburgite	yellow	2.51	3.08	5.94	36.68		0.33	43.76	0.28	0.15		
McDonough, 1991	Grt-Peridotite	grey	1.23	0.9	7.26	44.2	0.11	0.08	45.5	0.09	0.05	2122	2394

Tab. 4: Assembly of published data from literature (see references at the table) and averaged analyses from Asút Tesoru seamount (Mean Asút Tesoru, this study) and reference material (K81-5). The color specification in the table belongs to the plotted data points in figure 33.
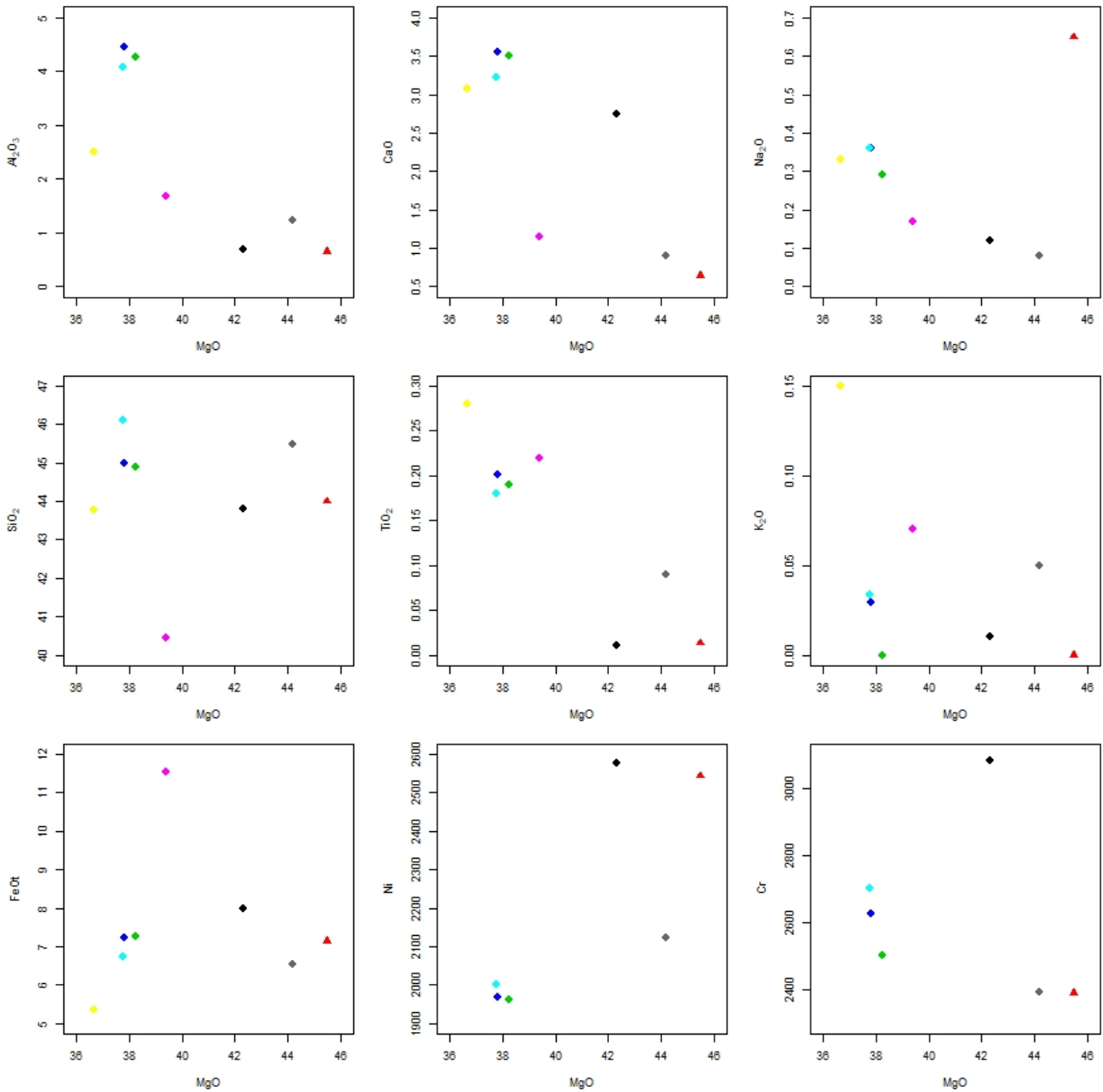
Fig. 33: Major oxides (in wt.%) with Ni and Cr (in ppm) plotted against MgO. Comparison data (see Tab. 4) originate from published literature, analyses of serpentine muds from Asút Tesoru (mean) and medium-serpentinized mantle rock as reference material (sample K81-5).

Color specification: red=Serpentine mud (Mean Asút Tesoru), black=Serpentinized rock (81-5), green=Depleted mantle, blue=Pyrolite model, cyan=Primitive mantle, magenta=Dunite, yellow=Harzburgite, grey=Grt-Peridotite.

The representative averaged value of the serpentine muds and K81-5 show a distinct negative correlation of Al_2O_3 and CaO against MgO, as was expected. Especially the discrepancy to primitive mantle rocks is apparent. In general, in comparison with unaltered lithologies the serpentine muds are depleted in most of the major oxides, including Al_2O_3, CaO, TiO_2 and K_2O, but show a significant enrichment in Na_2O.

SiO_2 and FeO_t values of the serpentine mud are in a regular range of mantle rocks and show unchanged concentrations relative to unaltered rocks, whereas the projecting phase (MgO) is much higher.

The trace elements Ni and Cr are typically enriched in unaltered mantle minerals, e.g. mantle olivine shows high Ni concentrations, while Cr is enriched in spinel, clinopyroxene and garnet. The illustrated diagrams exhibit a relatively high Ni concentration for the serpentine muds, but a negative correlation for Cr.

The analyzed medium-serpentinized reference sample K81-5 shows similar trends as the Asút Tesoru average, except for CaO, Na_2O and Cr. The MgO content is slightly lower than for serpentine mud, but higher compared to the literature datasets (except for Grt-Peridotite). The element distribution of K81-5 implies a medium grade serpentinized mantle rock chemistry.

The most analogical bulk rock chemistry compared to serpentine muds or sample K81-5 is documented in the dataset of McDonough (1991) for Garnet-Peridotite (see table 4), as apparent from figure 33.
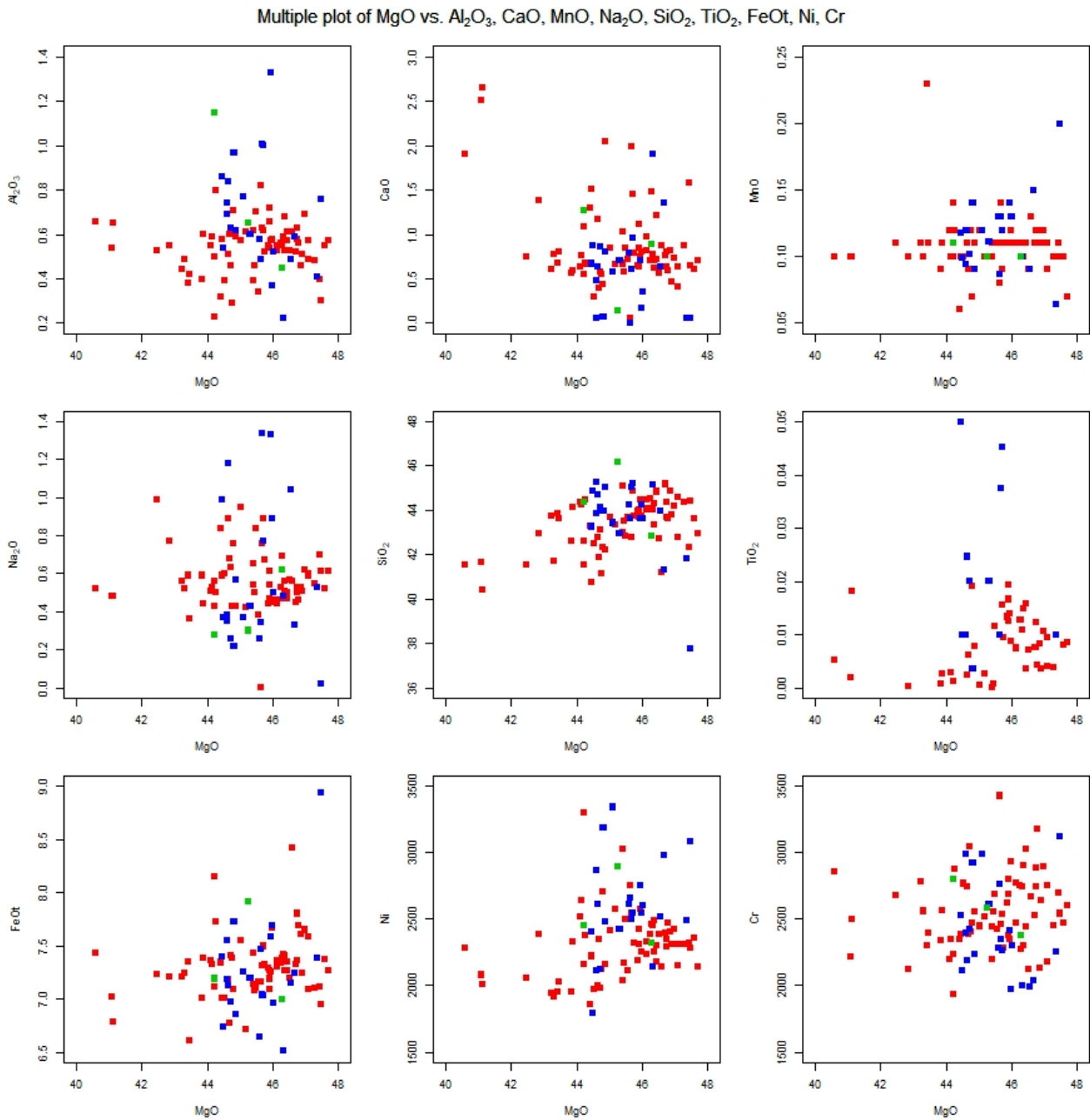
Fig. 34: Comparison of major oxides (in wt. %) with Ni and Cr (in ppm) plotted against MgO from the Expedition 366 mud volcanoes Yinazao (red), Fantangisna (green) and Asút Tesoru (blue). The analyses results are from IODP database (2017) and own measurements, accessible at appendix.

As can be seen from figure 34, oxides and trace elements from serpentine muds of the different mud volcanoes behave analogical, with slight deviations. Data from Fantanisna are rare, since only three analyses are documented. Na2O and TiO2 values from Asút Tesoru seamount show

wider scattering. A positive trend can be seen for SiO_2, FeO_t, Na_2O, Ni and Cr, while Al_2O_3 ($\pm CaO$) show a slight negative correlation to MgO.

4.3.2 Serpentine Mud Variations

For analyzing variations in chemical composition of single mineral phases within the bulk serpentine mud and especially for comparison with pseudomorphs, electron microprobe was used. The relatively low totals of the analyses are caused by the nature of serpentine minerals as these contain around 13 wt. % of water.

Sample	62_4	62_5	63_5	63_7	80_5	105_1	105_7
MgO	32.566	38.973	38.980	37.651	43.295	38.569	38.591
Na2O	0.075	0.048	0.092	0.144	0.085	0.720	0.011
SiO2	40.591	43.378	41.584	42.41	30.986	41.774	43.480
Al2O3	2.098	0.095	0.326	0.278	1.269	0.201	0.036
FeO	6.786	1.407	3.136	4.646	4.610	4.323	1.225
MnO	0.108	0.051	0.058	0.104	0.098	0.097	0.063
NiO	0.108	0.097	0.049	0.079	0.239	0.195	0.271
K2O	0.067	0.006	0.002	0.007	0.003	0.073	0.006
BaO	0.012	0.011	0	0.026	0.090	0.011	0.035
CaO	0.021	0.003	0.012	0.016	0.054	0.067	0
Cl	0.045	0.120	0.331	0.103	0.253	0.873	0.004
Cr2O3	0.822	0	0.023	0	0.765	0.011	0.035
Total	**83.299**	**84.189**	**84.593**	**85.464**	**81.752**	**86.914**	**83.757**

Cation Proportions

	62_4	62_5	63_5	63_7	80_5	105_1	105_7
MgO	2.766	3.1752	3.2127	3.0829	3.8537	3.1486	3.154
Na2O	0.0083	0.005	0.0099	0.0153	0.0099	0.0764	0.0012
SiO2	2.3127	2.3708	2.2991	2.3295	1.8502	2.2876	2.3838
Al2O3	0.1409	0.0061	0.0212	0.018	0.0893	0.013	0.0023
FeO	0.3233	0.0643	0.145	0.2134	0.2302	0.198	0.0562
MnO	0.0052	0.0024	0.0027	0.0049	0.0049	0.0045	0.0029
NiO	0.005	0.0043	0.0022	0.0035	0.0115	0.0086	0.0119
K2O	0.0049	0.0004	0.0002	0.0005	0.0002	0.0051	0.0004
BaO	0.0003	0.0002	0	0.0006	0.0021	0.0002	0.0007

CaO	0.0013	0.0001	0.0007	0.0009	0.0034	0.004	0
Cl	0.0043	0.0111	0.0309	0.0096	0.0255	0.0803	0.0004
Cr2O3	0.037	0	0.001	0	0.0361	0.0005	0.0015
SumCations	5.6092	5.6399	5.7256	5.6791	6.1172	5.8268	5.6153
XMg	0.83	0.96	0.92	0.89	0.90	0.90	0.97
Si/(Mg+Fe)	1.03	1.07	0.98	1.00	0.64	0.97	1.09

Tab. 5: Representative analyses (in wt. %) for different types of serpentine muds with cation proportions. For the calculated X_{Mg} (Mg/(Mg+Fe)), FeO_t was assumed as $Fe^{2+}O$.

Analyses from table 5 depicts the manifold manifestations of the serpentine muds. Spot 62_4 represents a bastite texture, whereas the others are exemplifying for mixed bulk serpentine mud. Values from 62_5 and 105_7 show a depletion of Fe relative to the average mud and were analyzed in the immediate vicinity of magnetite filled veins. The measurements of bastite textures reveal a different composition with lowered XMg (0.8 – 0.9), but a distinct enrichment of Al and Cr, most likely reflecting the chemical composition of the protolith mineral (pyroxene). The proportion Si/(Mg+Fe) was proposed by Schwarzenbach et al. (2015) for serpentine mineral comparison, with a value of ~0.67 indicating pure serpentine.

4.3.3 Garnet and Spinel Group Mineral Chemistry

Raman spectroscopy unveiled the occurrence of andradite (Ca-Fe garnet), magnetite (Fe-Fe spinel) and chromite (Fe-Cr spinel) as minor phases within the serpentine mud. For mineral chemistry analysis and evaluation of the endmembers of detected garnets and spinel group minerals, electron microprobe analysis (EPMA) was used. From the 27 samples, four representatives (62, 63, 80, 105) was chosen and prepared for additional investigations, with more than 450 single measurements in total.

Chromite Solid Solution
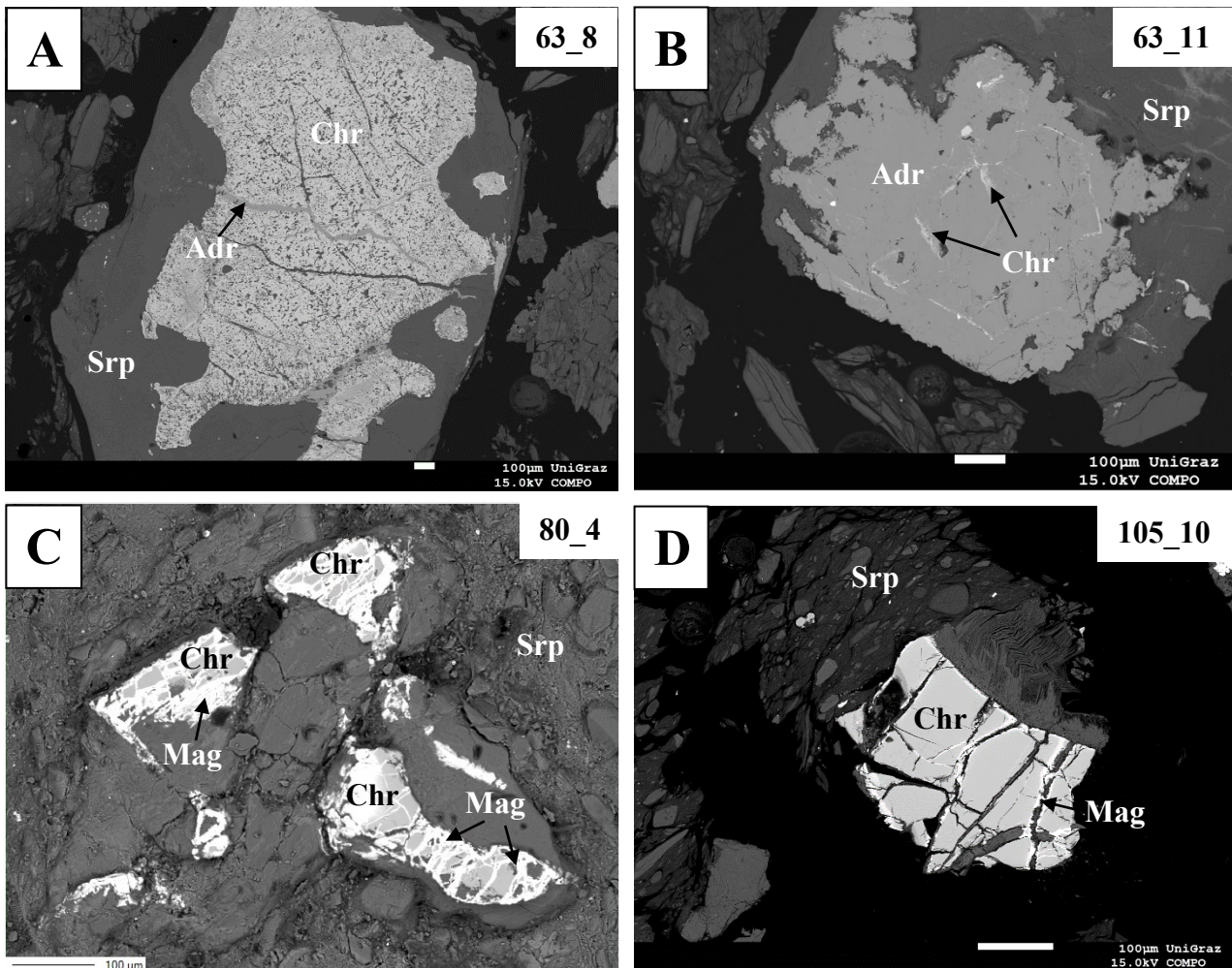
Fig. 35: Backscattered Electron (BSE) images of chromite mineral fragments. A.) Inherited mineral core bearing chromite with andradite filled veins, surrounded by serpentine rim. B.) Secondary grown andradite within a completely serpentinized mineral grain with chromite in filled veins or relict grain boundaries. C.) Relict chromite fragments with magnetite-filled cracks, surrounded by a heterogenous serpentine mud matrix. D.) Relict chromite grain with magnetite-filled cracks and conspicuous fibrous serpentine. Mineral abbreviations: Adr=Andradite, Chr=Chromite, Mag=Magnetite, Srp=Serpentine (mud).

Sample	63_3	63_8	63_11	80_4	105_2+3	105_4	105_10
SiO_2	0.03	0.01	0.02	0.01	0.03	0.07	0.01
TiO_2	0.07	0.30	0.06	0.02	0.00	0.19	0.11
Al_2O_3	27.20	2.95	23.63	27.34	17.72	6.06	20.00
Cr_2O_3	42.06	51.74	38.51	39.50	47.24	45.67	48.22
FeO	17.96	40.92	17.77	18.95	21.06	36.13	22.28
MnO	0.10	0.39	0.18	0.16	0.24	0.41	0.29
MgO	13.55	3.48	12.32	13.56	9.09	3.58	9.04
CaO	0.05	0.00	0.04	0.00	0.01	0.81	0.00
NiO	0.07	0.05	0.05	0.08	0.03	0.07	0.04
Na_2O	0.00	0.00	0.00	0.00	0.00	0.03	0.03
K_2O	0.00	0.01	0.00	0.01	0.00	0.01	0.00
Total	**101.07**	**99.84**	**92.57**	**99.62**	**95.42**	**93.01**	**100.01**

Cation Proportions

	63_3	63_8	63_11	80_4	105_2+3	105_4	105_10
Si	0.001	0	0.001	0	0.001	0.002	0
Ti	0.001	0.008	0.001	0	0	0.005	0.003
Al	0.954	0.123	0.91	0.969	0.699	0.267	0.75
Cr	0.99	1.454	0.995	0.939	1.25	1.348	1.214
Fe3	0.052	0.406	0.091	0.09	0.05	0.372	0.032
Fe2	0.395	0.81	0.394	0.386	0.54	0.756	0.561
Mn	0.002	0.012	0.005	0.004	0.007	0.013	0.008
Mg	0.601	0.184	0.6	0.608	0.453	0.199	0.429
Ca	0.002	0	0.002	0	0	0.032	0
Ni	0.002	0.001	0.001	0.002	0.001	0.002	0.001
Na	0	0	0	0	0	0.002	0.002
SumCations	3	2.998	3	2.998	3.001	2.998	3
X_{Spl}	0.288	0.012	0.275	0.296	0.160	0.028	0.163
X_{Hc}	0.190	0.051	0.181	0.188	0.190	0.106	0.213
X_{Mgf}	0.016	0.038	0.028	0.028	0.011	0.039	0.007
X_{Mag}	0.01	0.167	0.018	0.018	0.014	0.148	0.009
X_{Mgc}	0.299	0.136	0.301	0.287	0.286	0.142	0.264
X_{Chr}	0.197	0.597	0.198	0.183	0.340	0.537	0.344

Tab. 6: Representative analyses (in wt. %) for different types of spinel solid solutions with cation (per formula unit) and end-member proportions. Abbreviations: Spl=Spinel ($MgAl_2O_4$), Hc=Hercynite ($FeAl_2O_4$), Mgf=Magnesioferrite ($MgFe_2O_4$), Mag=Magnetite ($FeFe_2O_4$), Mgc=Magnesiochromite ($MgCr_2O_4$), Chr=Chromite ($FeCr_2O_4$).

The analyses from Tab. 5 show the broad diversity of spinel group solid solutions within the investigated serpentine muds, while some show a distinct spinel (senso stricto) or hercynite component with a strong enrichment in Al and Mg, others show almost none of the aforementioned. With reference to the whole rock analyses described in chapter 4.3.1 and due to the lack of other Al-containing phases, spinel must be the main Al bearing phase in the serpentine mud (see Fig. 35).

Altogether 39 analyses were made on chromite solid solution mineral grains, whereas isomorphic magnetite, as well a member of the spinel group, is separately shown. The averaged values for the measurements yield the following endmember composition:

$$\text{Spinel}_{0.20}\ \text{Hercynite}_{0.17}\ \text{Magnesioferrite}_{0.02}\ \text{Magnetite}_{0.03}\ \text{Magnesiochromite}_{0.27}\ \text{Chromite}_{0.30}$$

Furthermore, an averaged mineral formula after the general formula $(A^{2+}B^{3+}_2X^{2-}_4)$ is:

$$(Mg_{0.42}\ Fe_{0.57})\ (Al_{0.63}\ Fe_{0.17}\ Cr_{1.17})\ O_4$$

The explanatory power of the mean mineral formula, however, is limited due to the broad variability of endmembers. A noticeable feature is that almost all measured spinel (senso lato) grains comprise between 15 and 30% of a magnesiochromite component, most likely reflecting their origin from Mg-rich mantle rocks. Nevertheless, as apparent from Table 5 and the averaged endmember composition, chromite is the most dominant endmember phase.

Magnetite
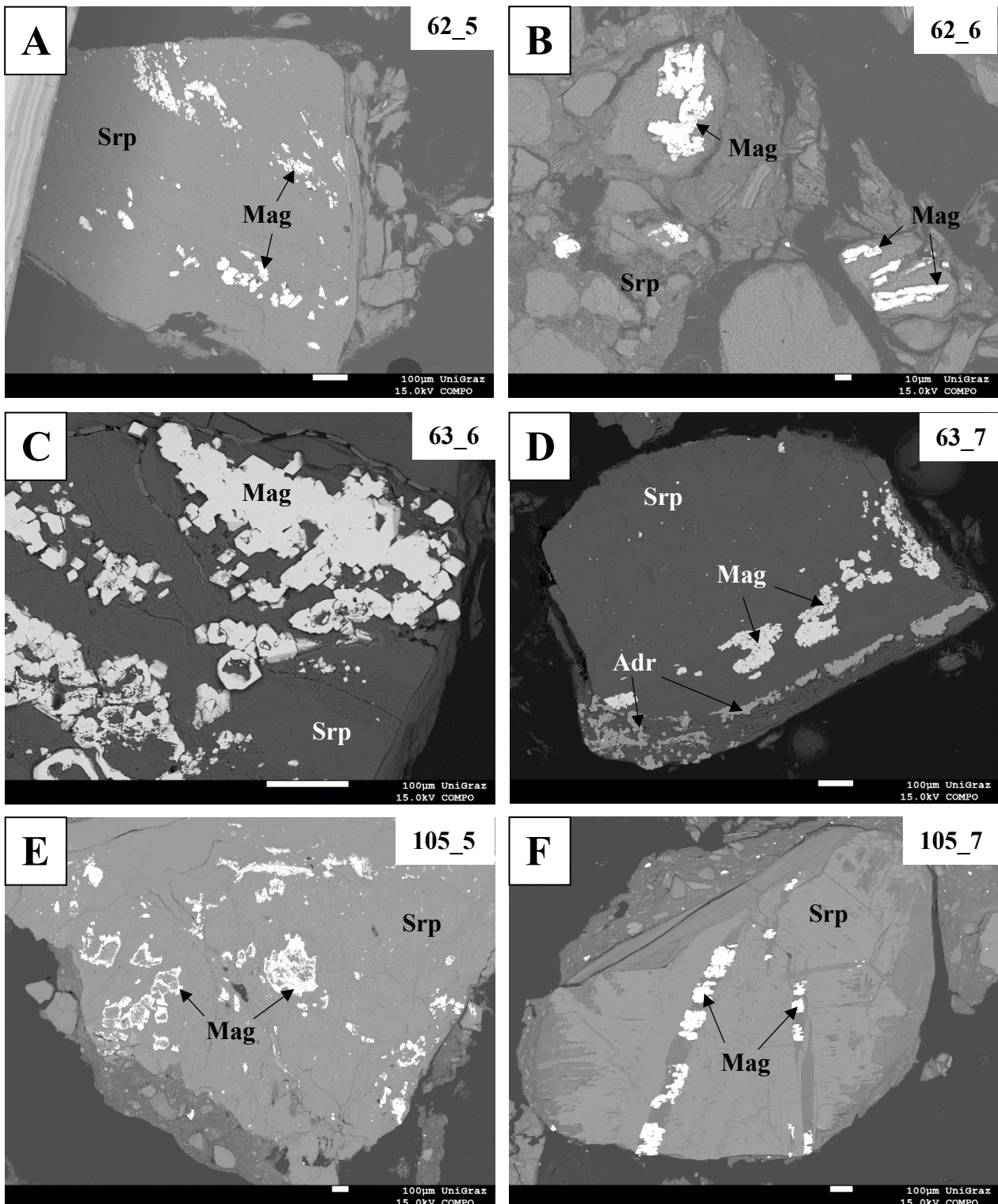
Fig. 36: Backscattered Electron (BSE) images of serpentine mud-based magnetite. A.) Completely serpentinized mineral fragment with intergrown magnetite grains. B.) Microcrystalline magnetite within a heterogenous mud matrix. C.) Aggregated idiomorphic

magnetite crystals, obviously in-situ grown. D.) Completely serpentinized relict mineral grain, rimmed by andradite and intergrown with magnetite. E.) Cr-rich magnetite rims, most likely tracing substituted protolith chromite fragments. F.) Aggregated magnetite crystals filling cracks of a serpentinized mineral grain. Mineral abbreviations: Adr=Andradite, Mag=Magnetite, Srp=Serpentinite (mud).

Magnetite could be detected in almost all samples from the Asút Tesoru seamount, although its occasional micro-crystallinity. In most cases the magnetite endmember is relatively pure with X_{Mag} from 0.9 and more, but some analyses expose solid solutions with higher proportions of isomorphic magnesioferrite and chromite (see Tab. 6), especially at spots where substitution or intergrowth after relict protolith minerals took place. As can be seen from Fig. 36, the pathway of growth mostly follows a specific pattern, suggesting that the mineral formation preferentially occurs at grain boundaries, veins, or cracks. Several analyses show various generations of magnetite crystals with different sizes and slightly modified chemical compositions. Apparent macroscopic single grains are mostly composed of aggregates of microcrystalline magnetite minerals, as BSE images unveiled.

For the evaluation of the mineral chemistry of magnetite from serpentine muds, 79 analyses were carried out at granular or aggregated magnetite, also known as ferrous-ferric oxide. Calculation of the averaged values for the measurements resulted in following endmember composition:

$$\text{Magnesioferrite}_{0.07} \text{ Magnetite}_{0.90} \text{ Chromite}_{0.02}$$

An averaged mineral formula after the general spinel group formula ($A^{2+}B^{3+}_2X^{2-}_4$) can be written as follows:

$$(\text{Mg}_{0.08} \text{ Fe}_{0.92}) (\text{Al}_{0.01} \text{ Si}_{0.05} \text{ Cr}_{0.04} \text{ Fe}_{1.85}) \text{ O}_4$$

Sample	62_3	62_5	62_6	63_5+6	63_7	80_4	105_2+3
SiO2	2.88	7.18	2.01	0.10	0.18	1.56	5.90
TiO2	0.34	0.01	0.00	0.00	0.06	0.12	0.03
Al2O3	0.00	0.13	0.03	0.02	0.00	1.73	0.08
Cr2O3	0.13	2.29	0.03	0.06	0.02	4.74	0.21
FeO	91.13	76.61	90.30	93.46	94.66	87.35	83.31
MnO	0.15	0.20	0.09	0.27	0.30	0.10	0.23
MgO	0.82	11.51	1.85	0.23	0.30	1.52	8.14
CaO	0.17	0.01	0.04	0.02	0.01	0.05	0.00
NiO	0.04	0.16	0.25	0.07	0.06	0.03	0.29
Na2O	0.03	0.03	0.20	0.05	0.00	0.02	0.07
K2O	0.00	0.01	0.02	0.00	0.00	0.00	0.01
Total	**95.69**	**98.13**	**94.83**	**94.27**	**95.59**	**97.22**	**98.26**

Cation Proportions

	62_3	62_5	62_6	63_5+6	63_7	80_4	105_2+3
Si	0.107	0.237	0.074	0.004	0.007	0.056	0.2
Ti	0.009	0	0	0	0.002	0.003	0.001
Al	0	0.005	0.001	0.001	0	0.074	0.003
Cr	0.004	0.06	0.001	0.002	0.001	0.136	0.006
Fe3	1.766	1.462	1.865	1.993	1.983	1.672	1.595
Fe2	1.054	0.656	0.93	0.972	0.98	0.969	0.765
Mn	0.005	0.006	0.003	0.009	0.01	0.003	0.007
Mg	0.045	0.567	0.102	0.013	0.017	0.082	0.411
Ca	0.007	0	0.002	0.001	0	0.002	0
Ni	0.001	0.004	0.007	0.002	0.002	0.001	0.008
Na	0.002	0.002	0.014	0.004	0	0.001	0.005
K	0	0	0.001	0	0	0	0
SumCations	3	2.999	3	3.001	3.002	2.999	3.001
X_{Hc}	0	0.002	0.001	0	0	0.036	0.001
X_{Mgf}	0.041	0.444	0.099	0.013	0.017	0.069	0.348
X_{Mag}	0.957	0.513	0.900	0.986	0.983	0.819	0.647
X_{Mgc}	0	0.018	0	0	0	0.006	0.001
X_{Chr}	0.002	0.021	0	0.001	0	0.066	0.002

Tab. 7: Representative magnetite analyses (in wt. %) with cation (per formula unit) and spinel-group endmember proportions. Abbreviations: Hc=Hercynite (FeAl2O4), Mgf=Magnesioferrite (MgFe2O4), Mag=Magnetite (FeFe2O4), Mgc=Magnesiochromite (MgCr2O4), Chr=Chromite (FeCr2O4).

Andradite
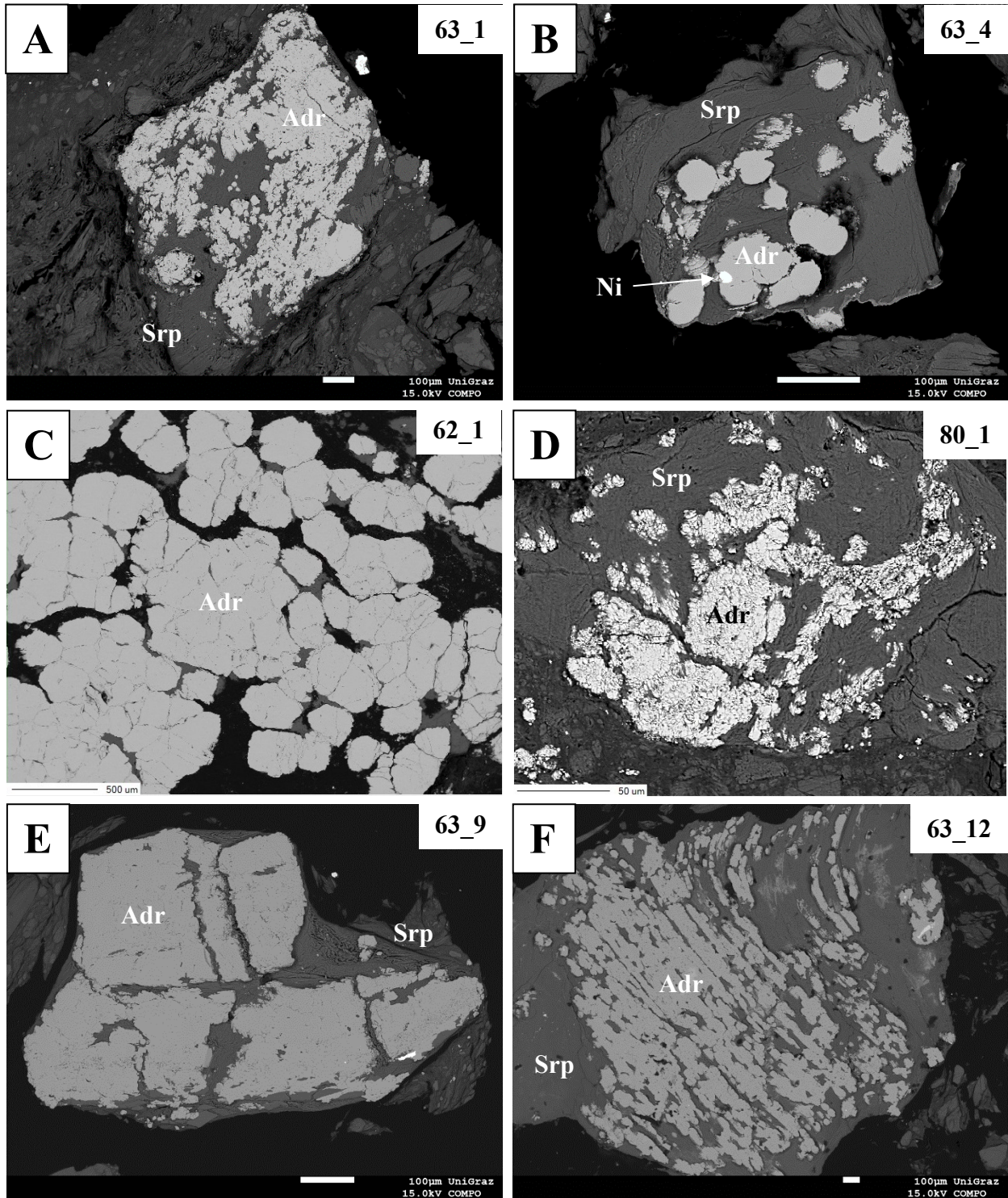
Fig. 37: Backscattered Electron (BSE) images of andradite garnets. A.) Pseudomorphic grown andradite aggregates, surrounded by microscopic serpentine debris. B.) Completely serpentinized mineral fragment with in-situ intergrown andradite crystals and Ni-alloy inclusion. C.) Enlarged section of a larger garnet grain (~5 mm), composed of numerous

aggregated bubble-like andradite crystals. D.) Disseminated microcrystalline andradite grains, showing signs of disintegration. E.) Partitioned andradite grain with relict grain boundaries at microscale, implies an initial development like image C. F.) Fibrous serpentinized mineral grain, engrossed by pseudomorphic andradite, growing in the serpentine minerals shape. Mineral abbreviations: Adr=Andradite, Ni=Nickel alloy, Srp=Serpentinite (mud).

The Electron Microprobe (EMPA) data from Tab. 7 show examples of analyses of andradite minerals within the serpentine muds. The garnets are in a certain range uniform in composition, except phases grown after relict spinel or chromite, as evident from Figure 35 A and B. These mineral phases can show elevated Cr proportions, thus forming a minor uvarovite ($Ca_3Cr_2[SiO_4]_3$) component. Conspicuously numerous andradite grains grew within completely serpentinized protolith grains, forming pseudomorphs. There is evidence to suggest that in a first stage is characterized by a scattered bubble-like anhedral garnet growth (see Fig. 37 B), forming conjugating aggregates at a progressed stage (see Fig. 37 C and F). It is apparent from the textures that the garnet growth occurs simultaneously to the serpentinization process.

Since bulk rock analyses (described in chapter 4.3.1) of the serpentine muds unveiled the low amount of CaO, and optical microscopy, Raman spectroscopy and Electron Microprobe analysis showed the lack of other Ca-bearing phases such as calcite, andradite seems to act as major sink for Ca in the system.

For the geochemical characterization of the andradite minerals, 92 analyses of single grains or aggregates were performed. An averaged mineral formula after the generalized formulation $A_3^{2+}B_2^{3+}[RO_4]_3$ can be written in the following way:

$$(Mg_{0.02}\,Ca_{3.15})\,(Al_{0.03}\,Fe_{1.94})\,[Si_{2.84}\,O_{12}]$$
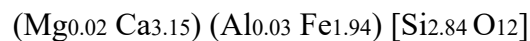
Sample	62_1	63_3	63_4	63_9	63_12	80_2	105_4
MgO	0.356	5.482	0.059	0.370	0.073	0.145	0.034
Na2O	0.012	0.074	0.00	0.00	0.00	0.058	0.034
SiO2	34.457	25.067	35.713	36.451	35.468	33.405	34.969
Al2O3	0.210	6.046	0.464	0.263	0.402	0.955	0.022
FeO	28.317	19.004	22.446	27.397	24.512	26.873	27.648
MnO	0.026	0.117	0.033	0.037	0.029	0.014	0.038
NiO	0.015	0.00	0.038	0.00	0.00	0.037	0.00
K2O	0.00	0.001	0.00	0.002	0.005	0.004	0.001
BaO	0.027	0.013	0.021	0.009	0.031	0.001	0.006
CaO	35.782	24.078	36.079	35.234	35.673	35.959	35.896
Cr2O3	0.00	18.724	5.399	0.028	3.579	0.024	0.914
TiO2	0.00	0.00	0.188	0.031	0.175	0.083	0.209
Total	**99.202**	**98.606**	**100.440**	**99.839**	**99.947**	**97.613**	**99.771**

Cation Proportions

	62_1	63_3	63_4	63_9	63_12	80_2	105_4
Mg	0.044	0.673	0.007	0.045	0.009	0.018	0.004
Na	0.002	0.012	0.000	0.000	0.000	0.009	0.005
Si	2.832	2.065	2.908	2.973	2.902	2.781	2.866
Al	0.020	0.587	0.045	0.025	0.039	0.094	0.002
Fe2	0	0	0	0	0	0	0
Fe3	1.947	1.309	1.528	1.869	1.677	1.871	1.895
Mn	0.002	0.008	0.002	0.003	0.002	0.001	0.003
Ni	0.001	0.000	0.002	0.000	0.000	0.002	0.000
K	0.000	0.000	0.000	0.000	0.001	0.000	0.000
Ba	0.001	0.000	0.001	0.000	0.001	0.000	0.000
Ca	3.151	2.125	3.148	3.079	3.127	3.208	3.152
Cr	0.000	1.220	0.348	0.002	0.232	0.002	0.059
Ti	0.000	0.000	0.012	0.002	0.011	0.005	0.013
SumCations	8.000	8.000	8.000	8.000	8.000	8.000	8.000
X_{Ca}	0.986	0.757	0.997	0.985	0.997	0.994	0.998
X_{Mg}	0.014	0.240	0.002	0.014	0.003	0.006	0.001

Tab. 8: Representative andradite analyses (in wt. %) with cation (per formula unit) proportions and calculated X_{Ca} and X_{Mg}.

4.3.4 Elemental Distribution of Garnets

For the evaluation of chemical composition variations of generic andradite garnets, elemental mapping was conducted. Compositional zonation patterns could reveal mineral growth dynamics, including periodicities and hydrothermal equilibrium conditions. Additionally, geochemical mapping could give evidence for the composition of the hydrothermal fluids from which the garnets precipitated. The elemental distribution mapping was conducted for the representative andradite garnet grains at 62_1, 63_12, 80_1 and 105_4 (see Fig. 37) for Mg, Al, Ca, Fe and Cr (plus Si for 105).

Andradite 62_1

The garnet grain displayed in Fig. 37 C (62_1) is a size larger than averaged garnets in the serpentine muds, and at a micro-scale composed of numerous aggregated andradite crystals, being faintly reminiscent of a cubic hexoctahedral habit.

The element mapping (see Fig. 38) unveiled completely homogeneous mineral grains with no core-rim relations or significant inclusions. It becomes apparent that the unzoned garnets contain almost no Al and Cr and thus no grossular (Ca-Al garnet) or uvarovite (Ca-Cr garnet) components, both theoretical solid solution endmembers. The sporadically elevated domains of Mg reflect the surrounding serpentinized material.
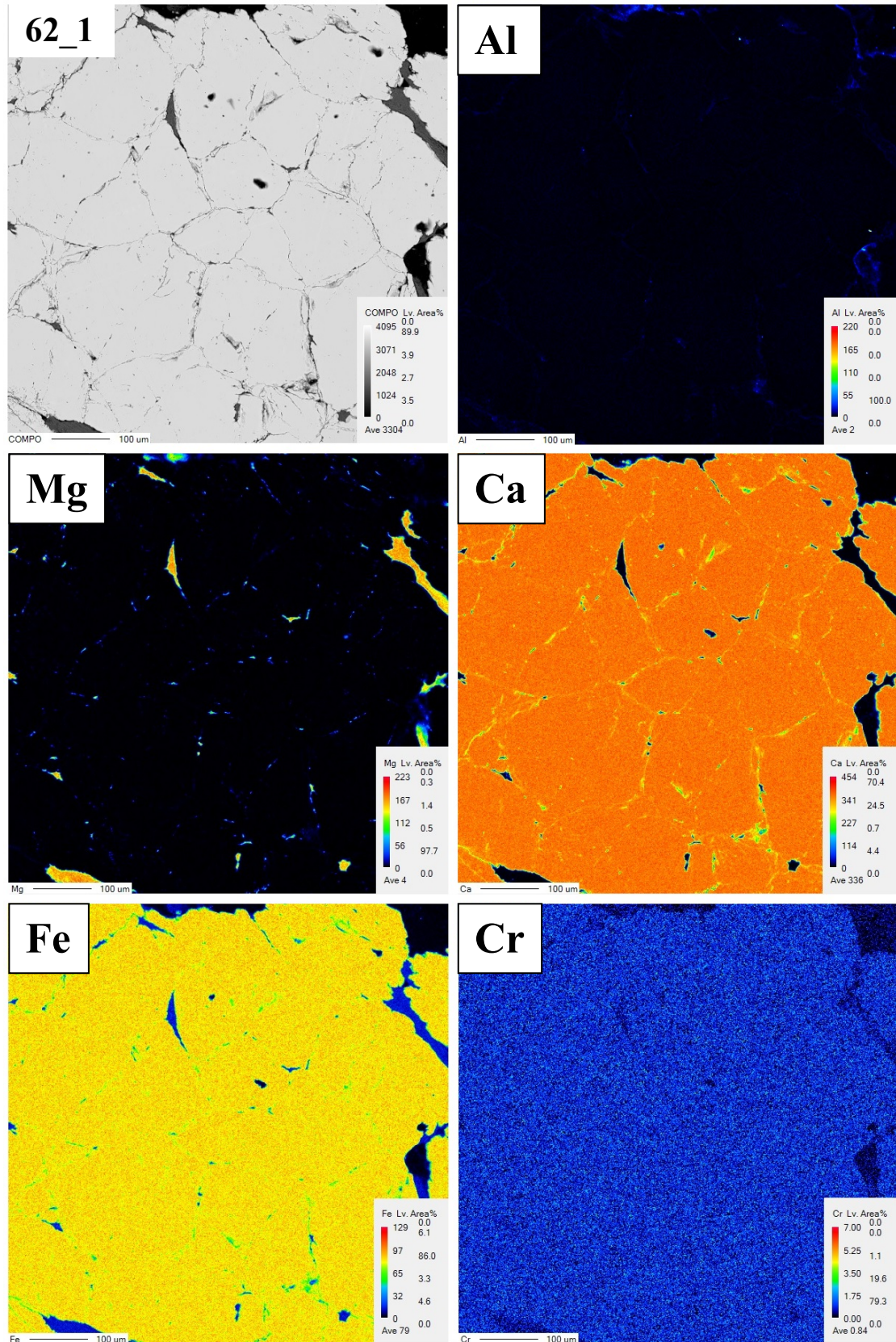
Fig. 38: Elemental distribution mapping and Backscattered Electron image of andradite garnet from sample 62 (spot 62_1) for Al, Mg, Ca, Fe and Cr.

Andradite 63_12

The andradite garnet displayed in Fig. 37 F (63_12) intergrows a fibrous serpentinized relict mineral grain, following the serpentine minerals shape (most likely fibrous chrysotile). The granular crystals coalesced with each other, as also observed at 62_1, 63_4 and others (see Fig. 37), and single grains have an isomorphic (cubic) mineral shape.

As apparent from Figure 39, the elemental distribution mapping shows a distinct zonation pattern of the garnet for Fe and Cr. In contrast to andradite 62_1, Ca is slightly lower, and Al is absent. The scattered Mg-rich areas are caused by the surrounding serpentine minerals of the groundmass matrix, which also show little amounts of Fe. The compositional variations of Fe and Cr occur between a core and a rim zone of the mineral grains, whereby the majority of the former granular garnets are intergrown, with washed-out grain boundaries due to prograde aggregation. In the core area of the garnets, Cr is enriched and decreases towards the rims, Fe behaves inversely proportional. Since garnet growth is obviously bounded on fibrous minerals, one can assume that the enriched core reflects the chemical composition of the host mineral.
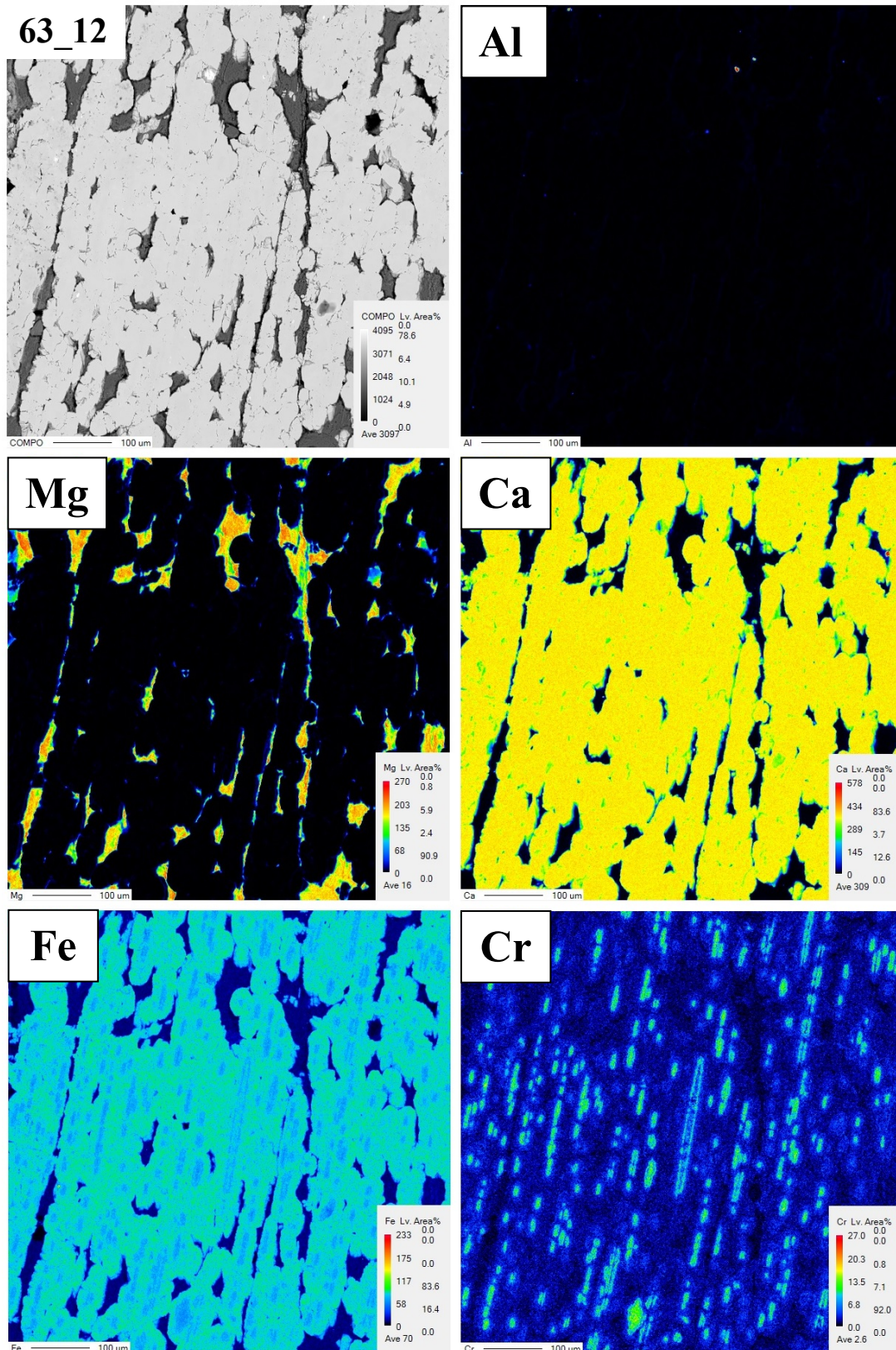
Fig. 39: Elemental distribution mapping and Backscattered Electron (BSE) image of andradite from sample 63 (garnet 63_12) for Al, Mg, Ca, Fe and Cr.

Andradite 80_1
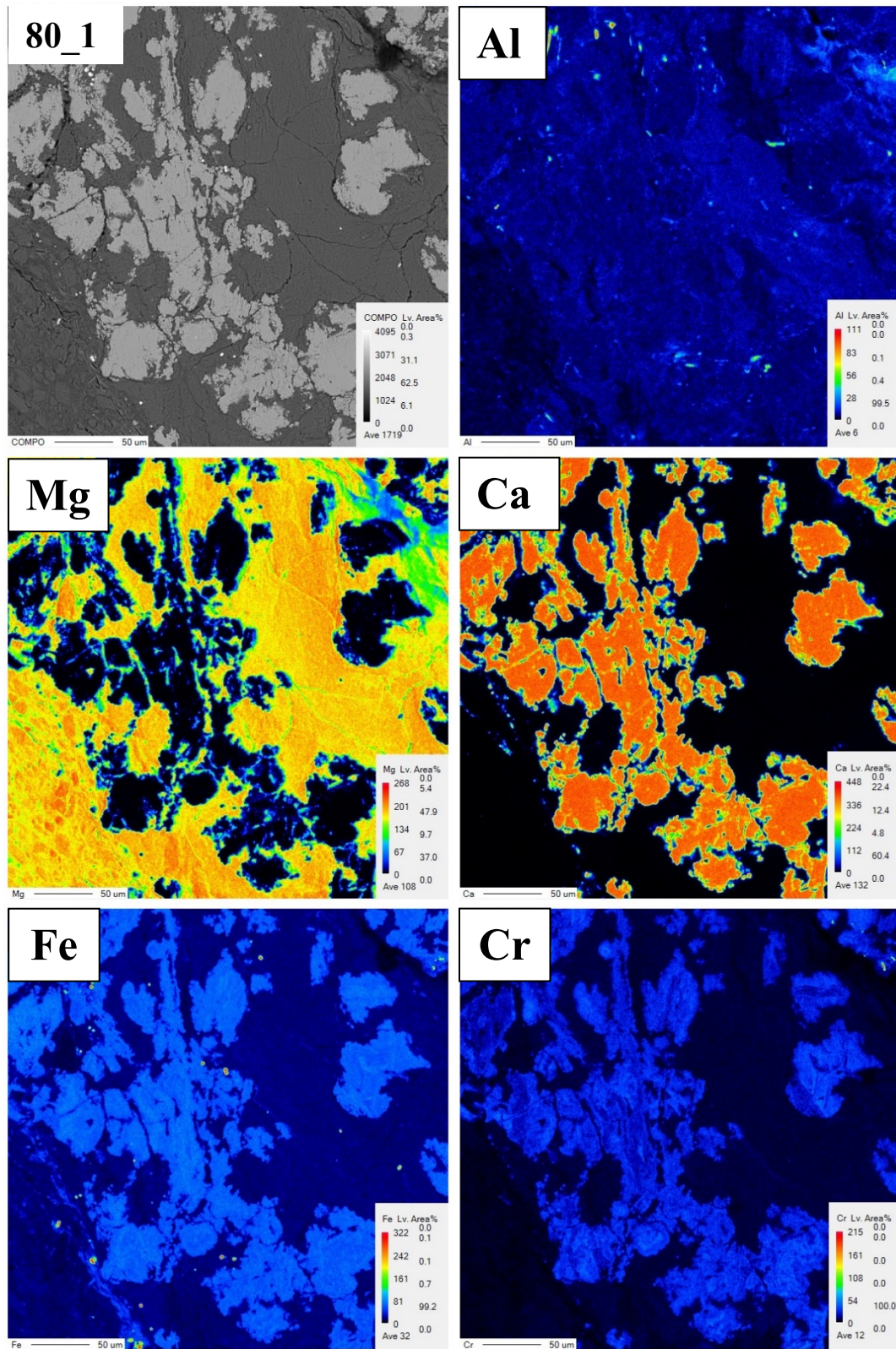
Fig. 40: Elemental distribution mapping and Backscattered Electron (BSE) image of andradite from sample U1494A-80 for Al, Mg, Ca, Fe and Cr.

As apparent from Figure 40, andradite garnet 80_1 is composed of numerous irregularly shaped segments which are not bounded by any (signified) characteristic crystal faces, what sets the garnet apart from the above described andradite aggregates (62_1, 63_12). The grains are surrounded by a microcrystalline serpentine matrix which is largely homogeneous in element composition and quite likely represents a pseudomorph. Because of the diffuse grain boundaries of the crystals it is difficult to interpret the pre-history of growth or if the current shape reflects a decomposition event. Apparently, the initial growth of the andradite took place after the complete replacement of the protolith mineral by serpentine.

In contrast to 62_1 and 63_12 garnets, this andradite shows slightly elevated Ca and Al, whereby Fe concentration is lower. The flamboyant Mg mapping mainly reflects the surrounding Mg-rich serpentine. Conspicuous is the grain edge-based decrease in Ca concentration, behaving inversely proportional to Mg. This could possibly display an increased exchange of Ca versus Mg with the serpentine matrix and led theoretically to a local pyrope (Mg-Al garnet) or knorringite (Mg-Cr garnet) component.

Andradite 105_4

Different from 80_1, garnet 105_4 is a more compact mineral grain, evidently composed of aggregated and intergrown smaller andradite grains (see Fig. 41 BSE image). The garnets form idiomorphic crystal faces with a roughly dodecahedral grain shape. The garnet is obviously broken through in the middle, exposing its aggregated structure. As apparent from Cr mapping, the andradite grain contains an inclusion of chromite. Si content conforms to the surrounding serpentine mud, while Al is absent except for the aforementioned spinel. As might have been expected, Ca is higher compared to the previously described garnets and Fe concentration ranges between those of 80_1 and 63_12.

The Cr distribution show a zonation-like pattern, originating from measurement interferences and do not reflect a fluctuation in chemical composition. Electron Microprobe single mineral analyses of the aggregated garnets yielded Cr concentrations of <1 wt. %.
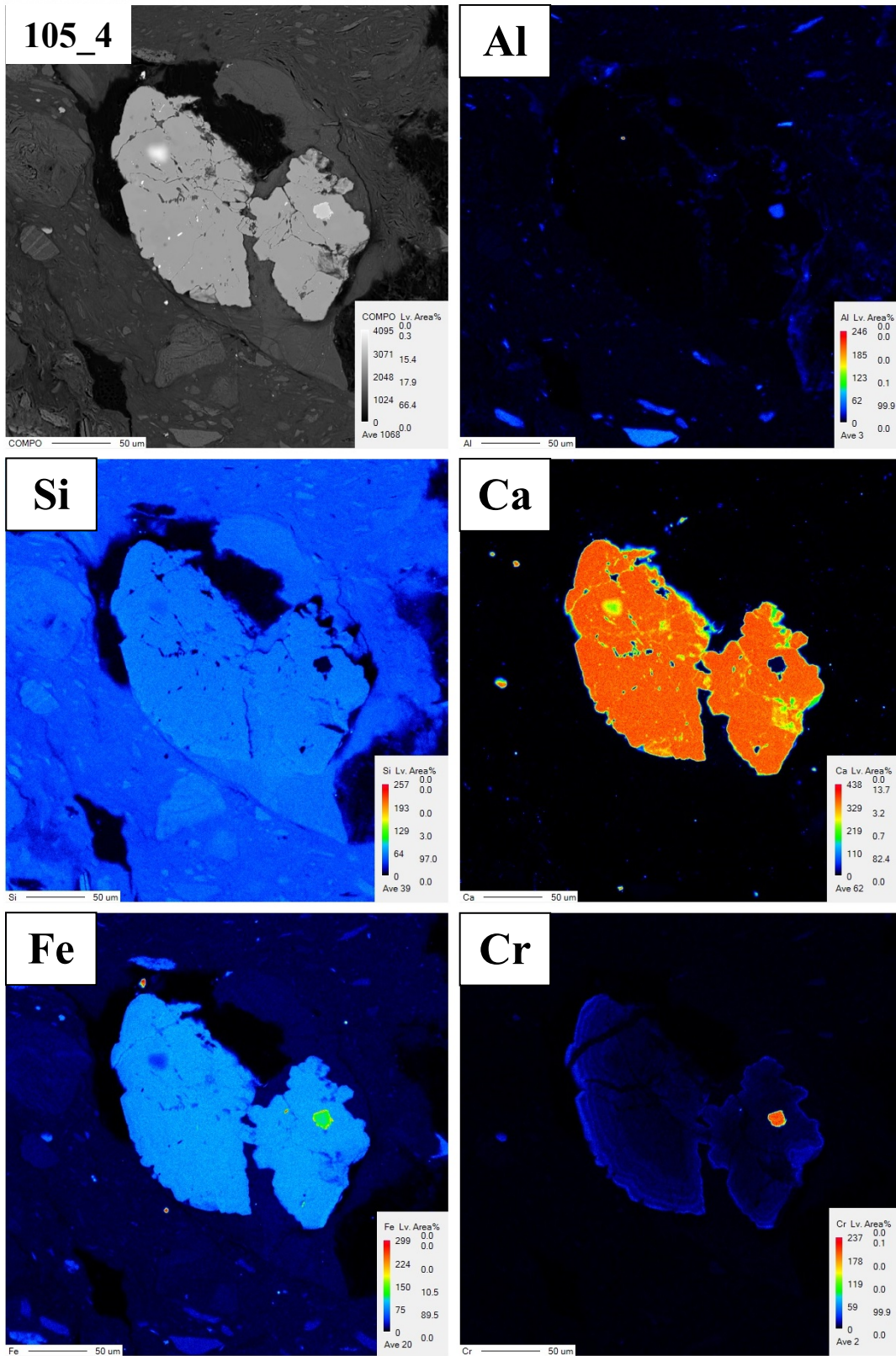
Fig. 41: Elemental distribution mapping and Backscattered Electron (BSE) image of andradite garnet with chromite inclusion from sample U1496A-105 for Al, Si, Ca, Fe and Cr.

5. Discussion

5.1 Serpentine Minerals

The serpentine muds examined in this study commonly show a mixture of the three polymorphic serpentine phases antigorite, lizardite and chrysotile, with varying dominance of a respective phase, dependent on the relative position within the mud volcano. Furthermore, two aspects must be separated: The cryptocrystalline bulk and the bastite/mesh composition. The bulk serpentine mud is primarily composed of chrysotile with subordinate lizardite at all sites. Bastite and mesh pseudomorphs from the summit site contain antigorite and lizardite as major phases, whereas similar textures from flank sites show lizardite and chrysotile as dominant mineral phases. Nevertheless, it is obvious that a complete conversion of antigorite with distance to the eruption center at the summit site takes place, reflecting the steady transformation processes the muds are exposed to. These observations correspond with recent insights of Debret et al. (2019), who posited a temperature range of 200 to about 400°C for a transition of antigorite to lizardite. Studies from Schwartz et al. (2013) unveiled a dominance of lizardite and chrysotile with instability of antigorite below 300°C in mesh textures, and an initial replacement of lizardite by antigorite between 320 and 390°C, whereas at temperatures above 390°C and HP conditions, antigorite is the most stable phase. Therefore, one can assume that the primordial antigorite-producing serpentinization conditions reach at least about 300°C, although the low-grade serpentines chrysotile and lizardite are the main bulk varieties. Once erupted, serpentine muds have undergone continuous changes, recognizable on the slightly different minerology of summit versus flank site samples. While summit muds show a relatively "fresh" assemblage with relict mineral fragments and bastite/mesh bound antigorite-lizardite mixture, flank sampled muds suggest a replacement of primordial antigorite by lizardite and chrysotile, and an ongoing degradation of relict minerals, expressed by a general increased grade of serpentinization of the muds. These relations correspond with the observations of Schwartz et al. (2013) and have been also accompanied by a change in color, especially within the upper few meters of the muds. On the one hand, the respective color reflects the conditions (oxidizing/reducing), on the other hand the minerology of the muds, e.g. content of chlorite, iowaite or Fe-oxides.

5.2 Iowaite

As described above, an evolution of the mud from summit to flank sites takes place, which includes the formation of cryptocrystalline iowaite. While at summit site samples (U1496) no iowaite could be detected, it is abundant at the upper sections of the flank sites (U1493 to U1495), as apparent from Figure 23. Since a dependency of the sampling depth could be observed (see Fig. 24), it is obvious that the secondary formation of iowaite after serpentine is bound on the availability and thus penetration depth of seawater. Within this "mixing zone", a term introduced by Mottl et al. (2004), seawater is providing Cl to the residual alkaline pore fluids, being essential for the formation of iowaite ($Mg_6Fe_2(OH)_{16} Cl_2.4H_2O$) from serpentine, as described by Braithwaite et al. (1994). Furthermore, it has been showed that iowaite can form a blue-green color, which may be co-responsible for the bluish-green tinge of the flank site muds. The replacement of brucite by iowaite, as reported by Bach et al. (2004), could not be ascertained, due to the microcrystalline nature of the phases in the mud. The dried, unprepared sample material evolved a yellowish surface coating over time, according to Braithwaite et al. (1994) caused by a decomposition of iowaite to isostructural pyroaurite (carbonate-analogue of iowaite) under exposure to atmospheric oxygen.

5.3 Andradite

Andradite garnet is found commonly as intergrowths mostly in pseudomorphic serpentine minerals or after chromite.

The geometry and the crystal shapes of the intergrowths suggests that they were formed as a result of reactive fluid flow in a porous medium, in good agreement with the insights of Beard and Hopkinson (2000). Although andradite occurs at almost all sites, specific enriched horizons could be observed (e.g. U1493B-63), potentially indicative for zones of elevated permeability with increased hydrothermal fluid flux. This implies Ca-metasomatism (Rodingitization), although fluids from Asút Tesoru are generally depleted in dissolved Ca, as described by Hulme et al. (2010). Frost and Beard (2007) showed that the breakdown of clinopyroxene can theoretically directly lead to andradite (see reaction 13), but the intergrowth of andradite with serpentine minerals show a formation subsequent to serpentinization. The most probable reaction path for the low temperature formation of andradite garnets are decarbonization

reactions (see reaction 14) as introduced by Taylor and Liou (1978), which also could lead to the carbonate chimney precipitating high-CO_2 fluids observed at the Asút Tesoru seamount (Fryer et al., 2018). Albers et al. (2019) showed a carbonization of peridotites from the Mariana forearc within an oxic environment at an early stage of the subduction. During progressing subduction, a formation of andradite garnets from carbonates is highly probable, since the environment at depth changes towards highly reducing and alkaline, indicated by accompanying Ni-alloys (see Fig. 37B) and emphasized by the geochemical models of Palandri and Reed (2003). A sufficient fluid availability and thus a certain permeability had to be ensured to obtain the obviously steady mineral growth, since no signs of disintegration could be detected. Because the mineral shapes are roughly cubic, and no deformation textures are visible, a low stress environment during crystallization can be assumed.

Inferentially, the above-mentioned andradite minerals are most likely formed from carbonates with a mostly homogenous chemical composition and almost pure andradite endmembers (XCa ~0.99).

Garnets inherited from chromite show a different mineral geometry and a more heterogenous elemental chemistry (from XCa ~0.75) with increased Al and Cr content (e.g. 63_3) and thus a minor uvarovite and grossular component. These minerals are microcrystalline and usually show intergrowth and transitions with the primordial chromite, making their distinction difficult.

In general, andradite garnets are minor phases within the serpentine muds and do not significantly affect the bulk chemical composition of the serpentine muds. Nevertheless, since calcium carbonates are just sparely present in the muds, andradite might be the main Ca-bearing phase in the system.

5.4 Magnetite

At almost all sampled serpentine muds from Asút Tesoru, magnetite could be detected, either as single grains within the mud or as oriented aggregated intergrowths in pseudomorphs or relict minerals (e.g. chromite spinel). In most cases magnetite is relatively pure with XMag 0.9 and above, some of the analyses, however, expose solid solutions with higher proportions of isomorphic magnesioferrite (up to XMgf ~0.44) and chromite, especially at spots where recrystallization of relict chromite spinel or intergrowth with serpentine minerals took place. Since it is obvious from microscopic and electron microprobe analyses that magnetite formation follows serpentinization, it may be accepted that mineral growth is an in-situ process.

This is in good agreement with the assumptions from Toft et al. (1990), who posited a multi-stage serpentinization process with no early formation of magnetite and thus a decoupled hydration of peridotite and formation of magnetite. Palandri and Reed (2003) suspected a breakdown of Fe-rich brucite by increased silica activity for triggering the formation of magnetite. In the case of Asút Tesoru serpentine muds, this seems highly improbable due to the extreme sensibility of andradite (and brucite) to high silica activities (Frost, 1985), making the garnet a reliable indicator for low silica activities, as suggested by Frost and Beard (2007). In addition, Frost and Beard (2007) described the assemblage brucite + andradite as indicative for low temperature (<225°C) serpentinization. Combining these insights with the observed idiomorphic magnetite crystals, which are indicative for growth in an almost stress-free environment, a late formation of the bulk magnetite could be concluded. The most probable reaction path for the formation of magnetite is the oxidation of the Fe component of serpentine ($Fe_3SiO_2O_5(OH)_4$, reaction 10), as proposed from Frost and Beard (2007). The process-related extracted silica could be bound by the buffering reaction of brucite (reaction 12), which forms serpentine from brucite with aqueous silica, and causes such a low silica activity that andradite could remain in equilibrium. In agreement with these observations, Oufi et al. (2002) showed that the Fe content of serpentine minerals decreases as the formation of secondary magnetite increases with progressive serpentinization.

In conclusion, magnetite from Asút Tesoru seamount formed form serpentine as secondary phase during a later stage of serpentinization with low silica activities and at lower temperature and pressure conditions. The observed directional euhedral growth of magnetite crystals is most likely bound on channelways for fluids, providing the oxygen necessary for the formation of magnetite.

5.5 Mobilization of Chromium

Since Cr zonation patterns of in-situ grown andradite garnets and chromite/magnesiochromite component of secondary formed magnetite are discerned, it is obvious that a certain mobilization of Cr occurred. The main mineralogical source of Cr at Asút Tesoru is provided by Cr-spinel ($FeCr_2O_4$), but the mineral is considered as hardly soluble and thus alteration-resistant. According to the work of Oze et al. (2016), the metastable occurrence of hydrogen peroxide (H_2O_2) could potentially oxidize Cr(III) in chromite and produce aqueous Cr(VI). The H_2O_2 production in fluids is coupled to elevated $H_{2(aq)}$ concentrations with ultrabasic pH (>10), reacting with relatively anoxic water, as verified by Foustoukos et al. (2011). Additionally, Foustoukos argued the possible formation of H_2O_2 in low-temperature hydrothermal systems (<125°C) as being related to serpentinization environments.

The formation of magnetite during later stages of serpentinization is coupled to the production of hydrogen, whereby the oxygen necessary for the process is extracted from decomposition of water, making serpentinites to the most reducing environments on Earth (e.g. Bach et al., 2006; Evans, 2008; Frost and Frost, 2014). Hulme et al. (2010) showed that upwelling pore waters of Mariana serpentine mud volcanoes are extremely alkaline with high pH values (~12). Combining aforementioned insights with observed data, it is highly probable that metastable production of H_2O_2 with subsequent oxidation of chromite-bound Cr(III) to Cr(VI) occurred at the Asút Tesoru serpentinization system. Experiments of Oze et al. (2016) showed that the production of hydrogen peroxide is pH dependent and increasing H_2O_2 increases Cr concentration in fluids.

The reduction of dissolved Cr(VI) is attributable to the formation of compatible minerals, e.g. magnetite (Oze et al., 2016). This would explain the detected trace chromite and magnesiochromite component in the secondary grown magnetite crystals. In combination with these observations, this could be the explanation of the alternating Cr concentrations of the andradite garnets, whereby the rarely encountered zonation patterns may reflect a fluctuation in pH (and H_2O_2) and thus in dissolved Cr. On the supposition that the formation of magnetite caused the necessary conditions for the formation of hydrogen peroxide, it can be assumed that andradite formation occurs subsequently and under lower hydrothermal conditions. Additionally, it is conceivable that an initial andradite growth from carbonates occurs during ascent of the mud and reconvenes after the eruption under influence of upwelling slightly Cr-

enriched fluids, what possibly would be an explanation for the core-rim relations and the found incongruent garnets.

These assumptions are consistent with the observations of Hulme et al. (2010) who reported mobilized Cr in pore waters at the upper sediment section of Asút Tesoru seamount.

5.6 Bulk Mud Element Variations

The massive accumulation of Na_2O in the bulk serpentine mud relative to (ultra-) mafic rocks (see Fig. 33) is most likely linked to hydrothermal alteration processes, since large ion lithophile (LIL) elements are easily soluble (due to low binding strength) and thus indicative for fluid phases. During the interaction of seawater with hot ultramafic rocks, K_2O (and CaO, respectively) goes preferentially into the fluid phase, whereas Na_2O is removed and incorporated in the solid phase (Stumm and Morgan, 1996). Compared to ultramafic rocks, MgO concentration of the mud is much higher, most likely a reflection of the enrichment and dominance of Mg-rich minerals (e.g. serpentine, brucite) in the material and a relative loss of other major elements. The elevated Ni concentration of the serpentine muds possibly stems from an incorporation in serpentine minerals or Fe-Ni-alloys (e.g. awaruite) after olivine.

The element variations most likely reflect the various distances from the trench axis (see Fig. 6), and thus different depths to the slab with distinct serpentinization states and metamorphic conditions, as described by Hulme et al. (2010) or Ryan et al. (2017).

6. Conclusions

This study provides new insights into processes during and after peridotite serpentinization at Asút Tesoru serpentine mud volcano. As a result of detailed mineralogical investigations, geochemical analyses and calculations, several conclusions could be made.

The bulk serpentine muds from Asút Tesoru are composed of a mixture of cryptocrystalline chrysotile and lizardite, whereas mesh and ±bastite textures of the summit site (U1496) are commonly composed of antigorite and lizardite. Since the muds undergo steadily transformation processes, antigorite is replaced by lizardite, accompanied by a general increase of serpentinization grade towards flank sites. The emergence of antigorite leads to the conclusion that the serpentinization temperature must have reached at least 300°C.

The average bulk serpentine muds show a chemical composition with XMg >0.9 and an enrichment in iron (between 3 – 5 wt. %), whereas bastite textures reveal a lowered XMg (0.8 – 0.9) and a distinct increase of Al and Cr, most likely reflecting the chemical composition of the protolith pyroxene.

The ongoing evolution of the serpentine mud includes the formation of cryptocrystalline iowaite within the upper section of the mud deposits. Mineralogical investigations showed that the post-eruptive mineral is bound on the penetration depth of seawater and occurs just at the flank sites (U1493 to U1495) of the mud volcano. Iowaite could also be co-responsible for the bluish-green tinge of flank site samples.

Andradite garnet is found commonly as intergrowths mostly in pseudomorphic serpentines (XCa >0.9) or chromite (XCa ~0.75), which is indicative for a formation subsequent to serpentinization. This leads to the inference that at least two growth periods must have formed the garnets. The assumption is supported by variances in chemical compositions, occasional expressed as zonation patterns with core-rim relations. The crystal habits and shapes of the aggregating intergrowths suggests a formation as a result of reactive fluid flow in a porous medium, in good agreement with the insights of Beard and Hopkinson (2000). The most probable reaction path for the initial low-temperature formation of andradite garnets are decarbonization reactions during the ascent of the mud mélange, which also could lead to the formation of carbonate chimneys precipitating from high-CO_2 fluids observed at Asút Tesoru seamount. It is conceivable that crystal growth resume after eruption, bound on upwelling

hydrothermal fluids with changed chemical composition. This would be an explanation for the occasional found core-rim relations, the incongruent garnets, and the aggregated idiomorphic andradite garnets, obviously grown in equilibrium under low-stress conditions. The detected garnets inherited from chromite are commonly microcrystalline and discernable by an increased Al and Cr concentration.

Andradite acts as a reliable indicator for low silica activities of the system, underpinned by the found assemblage andradite + brucite, on their part indicative for serpentinization temperatures below 225°C, as ascertained by Frost and Beard (2007). Furthermore, inclusions of Ni-alloys suggest a highly reducing environment. However, since calcium carbonates are just sparely found in the unaltered ("fresh") muds, andradite might be the main Ca sink in the system.

Secondary magnetite and relict chromite are observed members of the spinel mineral group. Averaged magnetite is relatively pure with XMag 0.9 and above, whereas chromite exposes manifold solid solutions with a dominant chromite endmember:

Spinel $_{0.20}$ Hercynite $_{0.17}$ Magnesioferrite $_{0.02}$ Magnetite $_{0.03}$ Magnesiochromite $_{0.27}$ Chromite $_{0.30}$

Investigations showed that the crystallization of magnetite most likely occurs at low silica activities by the extraction of Fe-bearing serpentine, producing highly reducing environments:

$$\text{Fe-Serpentine} + H_2O = \text{Magnetite} + SiO_{2(aq)} + H_2$$
$$Fe_3Si_2O_5(OH)_4 \qquad\qquad Fe_3O_4$$
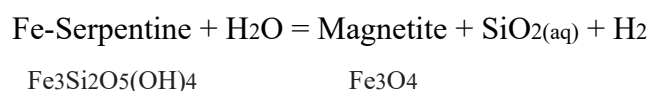
The reaction path is consistent with the observations summarized by Frost and Beard (2007). The process-related extracted silica could be bound by the buffering reaction brucite + SiO_{2aq} = serpentine, which retain a low silica activity and enables andradite to stay in equilibrium. All indications are that the secondary formation of magnetite occurs during a later stage of serpentinization with lowered silica activities and at lower temperature and pressure conditions. The observed directional euhedral growth of magnetite crystals is most likely bound on channelways for fluids, providing the oxygen necessary for the formation of magnetite.

Signs of disintegration of chromite and occasional Cr zonation patterns in andradite garnets imply a mobilization of Cr in fluids. Since previous studies from Foustoukos et al. (2011) posited a temperature (<125°C) and pH (>10) dependency for the oxidation of bound Cr(III) to dissolved Cr(VI), one can assume that the Cr-enriched garnets reflect a later stage of the

serpentinization process with higher Cr concentration in the fluid, subsequent to magnetite crystallization.

The general modal mineralogy of the serpentine mud from Asút Tesoru can be summarized as: serpentine + brucite + magnetite ± iowaite ± chlorite ± chromite. In summary mineral habits and assemblages, and chemical compositions reflect different stages and conditions of the serpentinization and mud evolution, both pre- and post-eruptive. Analyses of major element compositions imply a non-fertile mantle as most probable protolith, although an isochemical emergence of the mud is very unlikely.

7. References

Abers G. A., 1996. Plate structure and the origin of double seismic zones. American Geophysical Union Geophysical Monograph Series, Vol. 96, 223-228. https://doi.org/10.1029/GM096p0223

Albers G. A., Bach W., Klein F., Menzies C. D., Lucassen F., Teagle D. A. H., 2019. Fluid-rock interactions in the shallow Mariana forearc: carbon cycling and redox conditions. Solid Earth, Vol. 10, 907-930. https://doi.org/10.5194/se-10-907-2019

Allégre C. J., Poirier J.-P., Humler E., Hofmann A. W., 1995. The chemical composition of the Earth. Earth and Planetary Science Letters, Vol. 134(3-4), 515-526. https://doi.org/10.1016/0012-821X(95)00123-T

Arculus R. J., Ishizuka O., Bogus K. et al., 2015. A record of spontaneous subduction initiation in the Izu-Bonin-Mariana arc. Nature Geoscience, Vol. 8, 728-733. https://doi.org/10.1038/ngeo2515

Bach W., Garrido C. J., Paulick H., Harvey J., Rosner M., 2004. Seawater-peridotite interactions: First insights from ODP Leg 209, MAR 15°N. Geochemistry, Geophysics, Geosystems, Vol. 5(9). https://doi.org/10.1029/2004GC000744

Bach W., Paulick H., Garrido C. J., Ildefonse B., Meurer W. P., Humphris S. E., 2006. Unraveling the sequence of serpentinization reactions: petrography, mineral chemistry, and petrophysics of serpentinites from MAR 15°N (ODP Leg 209, Site 1274). Geophysical Research Letters, Vol. 33(13). https://doi.org/10.1029/2006GL025681

Beard J. S., Hopkinson L., 2000. A fossil, serpentinization-related hydrothermal vent, Ocean Drilling Program Leg 173, Site 1083 (Iberia Abyssal Plain): Some aspects of mineral and fluid chemistry. Journal of Geophyysical Research: Solid Earth, Vol. 105(B7), 16527-16539. https://doi.org/10.1029/2000JB900073

Biagioni C., Pasero M., 2014. The systematics of the spinel-type minerals: An overview. American Mineralogist, Vol. 99(7), 1254-1264. https://doi.org/10.2138/am.2014.4816

Bird P., 2003. An updated digital model of plate boundaries. Geochemistry, Geophysics, Geosystems, Vol. 4(3). https://doi.org/10.1029/2001GC000252

Bloomer S. H., 1983. Distribution and origin of igneous rocks from the landward slopes of the Mariana Trench: Implications for its structure and evolution. Journal of Geophysical Research: Solid Earth, Vol. 88(B9), 7411-7428. https://doi.org/10.1029/JB088iB09p07411

Bostock M. G., Hyndman R. D., Rondenay S., Peacock S. M., 2002. An inverted continental Moho and serpentinization of the forearc mantle. Nature, Vol. 417, 536-538. https://doi.org/10.1038/417536a

Braithwaite R. S. W., Dunn P. J., Pritchard R. G., Paar W. H., 1994. Iowaite, a re-investigation. Mineralogical Magazine, Vol. 58(390), 79-85.

Chavagnac V., Monnin C., Ceuleneer G., Boulart C., Hoareau G., 2013. Characterization of hyperalkaline fluids produced by low-temperature serpentinization of mantle peridotites in the Oman and Ligurian ophiolites. Geochemistry, Geophysics, Geosystems, Vol. 14(7), 2496-2522. https://doi.org/10.1002/ggge.20147

Cotter C. H., 1965. The physical geography of the oceans. The Bodley Head Ltd., ISBN: 9780370003498.

Cosca M., Arculus R. J., Pearce J., Mitchell J. G., 1998. ^{40}Ar/^{39}Ar and K–Ar geochronological age constraints for the inception and early evolution of the Izu–Bonin–Mariana arc system. Island Arc, Vol. 7(3), 579-595. https://doi.org/10.1111/j.1440-1738.1998.00211.x

Dachs E., 1998. PET: petrological elementary tools for mathematica. Computers & Geosciences, Vol. 34(3), 219-235. https://doi.org/10.1016/S0098-3004(97)00141-6

Debret B., Albers E., Walter B., Price R., Barnes J.-D., Beunon H., Facq S., Gillikin D.-P, Mattielli N., Williams H., 2019. Shallow forearc mantle dynamics and geochemistry: New insights form Expedition 366. Lithos, Vol.326-327, 230-245. https://doi.org/10.1016/j.lithos.2018.10.038

Deschamps F., Guillot S., Godard M., Chauvel C., Andreani M., Hattori K., 2010. In situ characterization of serpentinites from forearc mantle wedges: Timing of serpentinization and

behavior of fluid-mobile elements in subduction zones. Chemical Geology, Vol. 269(3-4), 262-277. https://doi.org/10.1016/j.chemgeo.2009.10.002

Domanik K. J., Holloway J. R., 1996. The stability and composition of phengite muscovite and associated phases from 5.5 to 11 GPa: Implications for deeply subducted sediments. Geochimica et Cosmochimica Acta. Vol. 60(21), 4133-4150. https://doi.org/10.1016/S0016-7037(96)00241-4

Embley R. W., Baker E. T., Butterfield D. A., Chadwick Jr. W. W., Lupton J. E., Resing J. A., De Ronde C. E., Nakamura K., Tunnicliffe V., Dower J. F., Mergle S. G., 2007. Exploring the Submarine Ring of Fire: Mariana Arc-Western Pacific. Oceanography, Vol. 20(4), 68-79. https://www.jstor.org/stable/24860145

Evans B. W., 2008. Control of the Products of Serpentinization by the Fe-Mg Exchange Potential of Olivine and Orthopyroxene. Journal of Petrology, Vol. 49(10), 1873-1887. https://doi.org/10.1093/petrology/egn050

Ferracutti G. R., Gargiulo F. M., Ganuza L. M., Bjerg E. A., Castro S. M., 2015. Determination of the spinel group end-members based on electron microprobe analyses. Miner Petrol, Vol. 109, 153-160. https://doi.org/10.1007/s00710-014-0363-1

Foustoukos D. I., Houghton J. L., Seyfried W. E., Sievert S. M., Cody G. D., 2011. Kinetics of H2–O2–H2O redox equilibria and formation of metastable H2O2 under low temperature hydrothermal conditions. Geochimica et Cosmochimica Acta, Vol. 75(6), 1594-1607. https://doi.org/10.1016/j.gca.2010.12.020

Frost R. B., 1985. On the Stability of Sulfides, Oxides, and Native Metals in Serpentine. Journal of Petrology, Vol. 26(1), 31-63. https://doi.org/10.1093/petrology/26.1.31

Frost R. B., Abebajo M. O., Erickson K. L., 2005. Raman spectroscopy of synthetic and natural iowaite. Spectrochimica Acta Part A: Molecular and Biomolecular Spectroscopy, Vol. 61(4), 613-620. https://doi.org/10.1016/j.saa.2004.05.015

Frost R. B., Beard J. S., 2007. On Silica Activity and Serpentinization. Journal of Petrology, Vol. 48(7), 1351-1368. https://doi.org/10.1093/petrology/egm021

Frost R. B., Evans K. A., Swapp S. M., Beard J. S., Mothersole F. E., 2013. The process of serpentinization in dunite from New Caledonia. Lithos, Vol 178, 24-39. https://doi.org/10.1016/j.lithos.2013.02.002

Frost R. B., Frost C. D., 2014. Essentials of Igneous and Metamorphic Petrology. Second Edition, Cambridge University Press, ISBN: 978-1108482511.

Fryer P., Fryer G. J., 1987. Origins of Nonvolcanic Seamounts in a Forearc Environment. Seamounts, Islands, and Atolls, Vol. 43. https://doi.org/10.1029/GM043p0061

Fryer P., 1992. Mud volcanoes of the Marianas. Scientific American, Vol. 266(2), 46-53. https://www.jstor.org/stable/24938939

Fryer P., Mottl M. J., 1992. Lithology, Minerology, and Origin of Serpentinite Muds recovered from Conical and Torishima Forearc Seamounts: Results of Leg 125 Drilling. Proceedings of the Ocean Drilling Program, Scientific Results, Vol. 125.

Fryer P., Mottl M., Johnson L., Haggerty J., Phipps S., Maekawa H., 1995. Serpentine Bodies in the Forearcs of Western Pacific Convergent Margins: Origin and Associated Fluids. Geophysical Monograph, Vol. 88, 259-275.

Fryer P., 1996. Evolution of the Mariana Convergent Plate Margin System. Reviews of Geophysics, Vol. 34(1), 89-125. https://doi.org/10.1029/95RG03476

Fryer P., Wheat G., Williams T., and the Expedition 366 Scientists, 2017. Expedition 366 Preliminary Report: Mariana Convergent Margin and South Chamorro Seamount. International Ocean Discovery Program. https://doi.org/10.14379/iodp.pr.366.2017

Fryer P., Wheat C. G., Williams T., and the Expedition 366 Scientists, 2018. Sites U1493, U1494, and U1495. Proceedings of the International Ocean Discovery Program, Vol. 366. https://doi.org/10.14379/iodp.proc.366.106.2018

Fryer P., Wheat C. G., Williams T., and the Expedition 366 Scientists, 2018. Site U1496. Proceedings of the International Ocean Discovery Program, Vol. 366. https://doi.org/10.14379/iodp.proc.366.107.2018

Fryer P., Wheat C. G., Williams T., and the Expedition 366 Scientists, 2018. Expedition 366 summary. Proceedings of the International Ocean Discovery Program, Vol. 366. https://doi.org/10.14379/iodp.proc.366.101.2018

Fryer P., Wheat G. C., Williams T., Kelley C., Johnson K., Ryan J., Kurz W., Shervais J., Albers E., Bekins B., Debret B., Deng J., Dong Y., Eickenbusch P., Frery E., Ichiyama Y., Johnsston R., Kevorkian R., Magalhaes V., Mantovanelli S., Meanpace W., Menzies C., Michibayashi K., Moyer C., Mullane K., Park J., Price R., Sissmann O., Suzuki S., Taki K., Walter B., Zhang R., Amon D., Glickson D., Pomponi S., 2020. Mariana serpentine mud volcanism exhumes subducted seamount materials: implications for the origin of life. Phil. Transactions Royal Society A, Vol. 378: 20180425. https://doi.org/10.1098/rsta.2018.0425

Grande L., Augustyn A., 2009. Gems and Gemstones: Timeless Natural Beauty of the Mineral World. University of Chicago Press, ISBN: 978-0226305110.

Harry D. L., Ferguson J. F., 1991. Bounding the state of stress at oceanic convergent zones. Tectonophysics, Vol. 187(1-3), 305-314. https://doi.org/10.1016/0040-1951(91)90426-S

Hilde T. W. C. Uyeda S., Kroenke L., 1977. Evolution of the western pacific and its margin. Tectonophysics, Vol. 38(1-2), 145-152. https://doi.org/10.1016/0040-1951(77)90205-0

Hulme S. M., Wheat G. C., Fryer P., Mottl M., 2010. Pore water chemistry of the Mariana serpentinite mu volcanoes: A window to the seismogenic zone. Geochemistry, Geophysics, Geosystems, Vol. 11(1). https://doi.org/10.1029/2009GC002674

Hussong D. M., LaTraille S. L., 1980. Crustal structure across the Mariana island arc. Geophysical Monograph Series, Vol. 23, 209-221.

Janecky D. R., Seyfried W. E., 1985. Hydrothermal serpentinization of peridotite within the oceanic crust: Experimental investigations of mineralogy and major element chemistry. Geochimica et Cosmochimica Acta, Vol. 50(7), 1357-1378. https://doi.org/10.1016/0016-7037(86)90311-X

Janoušek V., Farrow C. M., Erban V., 2006. Interpretation of Whole-rock Geochemical Data in Igneous Geochemistry: Introducing Geochemical Data Toolkit (GCDkit). Journal of Petrology, Vol. 47(6), 1255-1259. https://doi.org/10.1093/petrology/egl013

Karig D. E., 1971. Structural History of the Mariana Island Arc System. GSA Bulletin, Vol 82(2), 323-344. https://doi.org/10.1130/0016-7606(1971)82[323:SHOTMI]2.0.CO;2

Kelley D. S., Karson J. A., Blackman D. K., Früh-Green G., Butterfield D. A., Lilley M. D., Olson E. J., Schrenk M. O., Roe K. K., Lebon G. T., Rivizzigno P., AT3-60 Shipboard Party, 2001. An off-axis hydrothermal vent field near the Mid-Atlantic Ridge at 30°N. Nature, Vol. 412, 145-149. https://doi.org/10.1038/35084000

Kelts K. R., 1998. Components in Lake Sediments: Smear Slide Identifications. Limnogeology in Spain: A tribute to Kerry Kelts, Blas L. Valero-Garcés, ISIN: 9788400081645.

Klemperer S. L., Fouch M. J., Stern R. J., 2003. An overview of the Izu-Bonin-Mariana Subduction Factory. Geophysical Monograph, Vol. 138, 175-222.

Klein F., Bach W., Jöns N., McCollom T., Moskowitz B., Berquó T., 2009. Iron partioningg and hydrogen generation during serpentinization of abyssal peridotites from 15°N on the Mid-Atlantic Ridge. Geochimica et Cosmochimica Acta, Vol. 73(22), 6868-6893. https://doi.org/10.1016/j.gca.2009.08.021

Lachenbruch A. H., 1980. Frictional heating, fluid pressure, and the resistance to fault motion. Ournal of Geophsical Research: Solid Earth, Vol. 85(B11), 6097-6112. https://doi.org/10.1029/JB085iB11p06097

Lafuente B., Downs R. T., Yang H., Stone N., 2015. The power of databases: the RRUFF project. Highlights in Mineralogical Crystallography, 1-30, ISBN: 978-3110417043.

Lallemand S., 1995. High rates of arc consumption by subduction processes: Some consequences. Geology, Vol. 23(6), 551-554. https://doi.org/10.1130/00917613(1995)023<0551:HROACB>2.3.CO;2

Lallemand S., 2016. Philippine Sea Plate inception, evolution, and consumption with special emphasis on the early stages of Izu-Bonin-Mariana subduction. Progress in Earth and Planetary Science, Vol. 3(15). https://doi.org/10.1186/s40645-016-0085-6

Le Maitre R. W., 1976. The Chemical Variability of some Common Igneous Rocks. Journal of Petrology, Vol. 17(4), 589-598. https://doi.org/10.1093/petrology/17.4.589

Ludwig K. A., Kelley D. S., Butterfield D. A., Nelson B. K., Früh-Green G., 2006. Formation and evolution of carbonate chimneys at the Lost City Hydrothermal Field. Geochimica et Cosmochimica Acta, Vol. 70(14), 3625-3645. https://doi.org/10.1016/j.gca.2006.04.016

Marsaglia K., Milliken K., Doran L., 2013. Smear slides of marine mud for IODP core description, Volume I. Part 1: Methodology and atlas of siliciclastic and volcanogenic components. IODP Technical Note 1. https://doi.org/10.2204/iodp.tn.1.2013

Marsaglia K., Milliken K., Leckie R. M., Tentori D., Doran L., 2015. IODP Smear Slide Digital Reference for Sediment Analysis of Marine Mud. Part 2: Methodology and Atlas of Biogenic Components. IODP Technical Note 2. https://doi.org/10.14379/iodp.tn.2.2015

Mazzullo J., Graham A. G., 1988. Handbook for Shipboard Sedimentologists. Ocean Drilling Program, Technical Note No. 8.

McDonough W. F., 1991. Partial melting of subducted oceanic crust and isolation of its residual eclogitic lithology. Phil. Transactions of the Royal Society A, Vol. 335, 407-418. https://doi.org/10.1098/rsta.1991.0055

McDonough W. F., Sun S., 1995. The composition of the Earth. Chemical Geology, Vol. 120(3-4), 223-253. https://doi.org/10.1016/0009-2541(94)00140-4

Menapace W., Tangunan D., Maas M., Williams T., Kopf A., 2019. Rheology and Biostratigraphy of the Mariana Serpentine Muds Unravel Mud Volcano Evolution. Journal of Geophysical Research: Solid Earth, Vol. 124(11), 10752-10776. https://doi.org/10.1029/2019JB018265

Moody J. B., 1976. Serpentinization: a review. Lithos, Vol. 9(2), 125-138. https://doi.org/10.1016/0024-4937(76)90030-X

Morrow C. A., Moore D. E., Lockner D. A., Bekins B. A., 2019. Data report: permeability, porosity, and frictional strength of core samples from IODP Expedition 366 in the Mariana forearc. Proceedings of the IODP, Vol. 366. https://doi.org/10.14379/iodp.proc.366.202.2019

Mottl M. J., Wheat G. C., Fryer P., Gharib J., Martin J. B., 2004. Chemistry of springs across the Mariana forearc shows progressive devolatilization of the subducting plate. Geochimica et Cosmochimica Acta, Vol 68(13), 4915-1933. https://doi.org/10.1016/j.gca.2004.05.037

Nagaya T., Walker A. M., Wookey J., Wallis S. R., Ishii K., Kendall J. M., 2016. Seismic evidence for flow in the hydrated mantle wedge of the Ryukyu subduction zone. Scientific Reports, Vol. 6: 29981. https://doi.org/10.1038/srep29981

Oakley A. J., Taylor B., Fryer P., Moore G. F., Goodliffe A. M., Morgan J. K., 2007. Emplacement, growth, and gravitational deformation of serpentinite seamounts on the Mariana forearc. Geophysical Journal International, Vol. 170(2), 615-634. https://doi.org/10.1111/j.1365-246X.2007.03451.x

Oakley A. J., 2008. A multi-channel seismic and bathymetric investigation on the central Mariana convergent margin. (Dissertation), ProQuest Dissertations and Theses, Diss. Abstracts International, Vol. 70(2B), 906.

Oakley A. J., Taylor B., Moore G. F., 2008. Pacific Plate subduction beneath the central Mariana and Izu-Bonin fore arcs: New insights from an old margin. Geochemistry, Geophsics, Geosystems, Vol. 9(6). https://doi.org/10.1029/2007GC001820

O'Hanley D. S., 1991. Fault-Related Phenomena Associated with Hydration and Serpentine Recrystallization during Serpentinization. Canadian Mineralogist, Vol. 29, 21-35.

Onuki H., Yoshida T., Nedachi M., 1981. Electron probe study of Ti-rich Hydroandradites in the Sanbagawa metamorphic rocks. Journal of Japanese Assoc. Mineralogy, Petrology, Geology, Vol. 76, 239-247.

Oufi O., Cannat M., Horen H., 2002. Magnetic properties of variably serpentinized abyssal peridotites. Journal of Geophysical Research: Solid Earth, Vol. 107(B5), 3-19. https://doi.org/10.1029/2001JB000549

Oze C., Fendorf S., Bird D. K., Coleman R. G., 2004. Chromium geochemistry in serpentinized ultramafic rocks and serpentine soils from the Franciscan complex of California. American Journal of Science, Vol. 304(1), 67-101. https://doi.org/10.2475/ajs.304.1.67

Oze C., Sleep N. H., Coleman R. G., Fendorf S., 2013. Anoxic oxidation of chromium. Geology, Vol. 44(7), 543-546. https://doi.org/10.1130/G37844.1

Palandri J. L., Reed M. H., 2004. Geochemical models of metasomatism in ultramafic systems: serpentinization, rodingitization, and sea floor carbonate chimney production. Geochimica et Cosmochimica Acta, Vol. 68(5), 1115-1133. https://doi.org/10.1016/j.gca.2003.08.006

Pälike H., Lyle M. W., Zeebe R. E., 2012. A Cenozoic record of the equatorial Pacific carbonate compensation depth. Nature, Vol. 488, 609-614. https://doi.org/10.1038/nature11360

Pearce J. A., Barker P. F., Edwards S. J., Parkinson I. J., Leat P. T., 2000. Geochemistry and tectonic significance of peridotites from the South Sandwich arc-basin system, South Atlantic. Contributions Mineral Petrol, Vol. 139, 36-53.

Pfeifer H. R., 1977. A model for fluids in metamorphosed ultramafic rocks. Observations at surface and subsurface conditions (high pH spring waters). Schweiz. Mineralogisch-Petrographische Mitteilungen, Vol. 57(3), 361-396.

Pokrovsky O. S., Schott J., 2000. Kinematics and mechanism of forsterite dissolution at 25°C and pH from 1 to 12. Geochimica et Cosmochimica Acta, Vol. 64(19), 3313-3325. https://doi.org/10.1016/S0016-7037(00)00434-8

Pytkowicz R. M., 1970. Geochimica et Cosmochimica Acta, Vol. 34(7), 836-839. https://doi.org/10.1016/0016-7037(70)90034-7

Ranero C. R., Morgan P. J., McIntosh K., Reichert C., 2003. Bending-related faulting and mantle serpentinization at the Middle America trench. Nature, Vol. 425, 367-373. https://doi.org/10.1038/nature01961

Ranero C. R., Sallarés V., 2004. Geophysical evidence for hydration of the crust and mantle on the Nazca plate during bending at the north Chile trench. Geology, Vol. 32(7), 549-552. https://doi.org/10.1130/G20379.1

Ryan J. G., Johnston R. M., Menzies C. D., Price R. E., Sissmann O., Fryer P., Wheat G., and Expedition 366 Scientific Party, 2017. Compositional Variability in Serpentinite Solids, IODP

Insights into a Developing Subduction Channel. School of Geosciences Faculty and Staff Publications, 1118. https://scholarcommons.usf.edu/geo_facpub/1118

Salters V. J. M., Stracke A., 2004. Composition of the depleted mantle. Geochemistry, Geophysics, Geosystems, Vol. 5(5). https://doi.org/10.1029/2003GC000597

Schmidt M. W., Poli S., 1998. Experimentally based water budgets for dehydrating slabs and consequences for arc magma generation. Earth and Planetary Science Letters, Vol. 163(1-4), 361-379. https://doi.org/10.1016/S0012-821X(98)00142-3

Schwartz S., Guillot S., Reynard B., Lafay R., Debret B., Nicollet C., Lanari P., Auzende A. L., 2013. Pressure-temperature estimates of the lizardite/antigorite transition in high pressure serpentinites. Lithos, Vol. 178, 197-210. https://doi.org/10.1016/j.lithos.2012.11.023

Schwarzenbach E. M., Caddick M. J., Beard J. S., Bodnar R. J., 2016. Serpentinization, element transfer, and the progressive development of zoning in veins: evidence from a partially serpentinized harzburgite. Contributions to Mineralogy and Petrology, Vol. 171(5). https://doi.org/10.1007/s00410-015-1219-3

Scott R., Kroenke L., 1980. Evolution of back arc spreading and arc volcanism in the Philippine Sea: Interpretation of Leg 59 DSDP results. Geophysical Monograph Series, Vol. 23, 283-291. https://doi.org/10.1029/GM023p0283

Sibson R. H., 1982. Fault zone models, heat flow, and the depth distribution of earthquakes in the continental crust of the United States. Bulletin of the Seismological Society of America, Vol. 72(1), 151-163.

Siivola J., Schmid R., 2007. 12. List of Mineral Abbreviations. Recommendations by the IUGS Subcommission on the Systematics of Metamorphic Rocks: Web version 01.02.07. http://minsoc.ru/FilesBase/paper_12.pdf

Sleep N. H., Meiborn A., Fridriksson T., Coleman R. G., Bird D. K., 2004. H2-rich fluids from serpentinization: Geochemical and biotic implications. Proceedings of the National Academy of Sciences, Vol. 101(35), 12818-12823. https://doi.org/10.1073/pnas.0405289101

Stern R. J., Bloomer S. H., 1992. Subduction zone infancy: Examples from the Eocene Izu-Bonin-Mariana and Jurassic California arcs. GSA Bulletin, Vol. 104(12), 1621-1636. https://doi.org/10.1130/0016-7606(1992)104<1621:SZIEFT>2.3.CO;2

Stern R. J., Smoot C. N., 1998. A bathymetric overview of the Mariana forearc. Island Arc, Vol. 7(3), 525-540. https://doi.org/10.1111/j.1440-1738.1998.00208.x

Strunz H., Nickel E., 2001. Strunz Mineralogical Tables: Ninth Edition. E. Nägele u. Obermiller, Stuttgart, ISBN: 978-3510651887.

Stumm W., Morgan J. J., 1996. Aquatic Geochemistry: Chemical Equilibria and Rates in Natural Waters, Third Edition. Environmental Science and Technology, Wiley-Interscience Publication, ISBN: 0-471-51184-6.

Suzuki S., Kuenen G., Schipper K., Van der Velde S., Ishii S., Wu A., Sorokin D., Tenney A., Meng X., Morrill P., Kamagata Y., Muyzer G., Nealson K., 2014. Physiological and genomic features of highly alkaliphilic hydrogen-utilizing Betaproteobacteria from a continental serpentinizing site. Nature communications, Vol. 5(3900). https://doi.org/10.1038/ncomms4900

Tarling M. S., Smith S. A. F., Scott J. M., 2019. Fluid overpressure from chemical reactions in serpentinite within the source region of deep episodic tremor. Nature Geoscience, Vol. 12, 1034-1042. https://doi.org/10.1038/s41561-019-0470-z

Taylor B., 1992. Rifting and the volcanic-tectonic evolution of the Izu-Bonin-Mariana arc. Proceedings of the ODP, Scientific Results, Vol. 126(42), 627-651.

Taylor B., Liou J., 1978. The low-temperature stability of andradite in C-O-H fluids. American Mineralogist, Vol. 63(3-4), 378-393.

Toft P. B., Arkani-Hamed J., Haggerty S. E., 1990. The effects of serpentinization on density and magnetic susceptibility: a petrophysical model. Physics of the Earth and Planetary Interiors, Vol. 65(1-2), 137-157. https://doi.org/10.1016/0031-9201(90)90082-9

Wenner D. B., Taylor Jr. H. P.,1971. Temperatures of serpentinization of ultramafic rocks based on O18/O16 fractionation between coexisting serpentine and magnetite. Contributions fo Mineralogy and Petrology, Vol. 32, 165-185. https://doi.org/10.1007/BF00643332

Wenner D. B., Taylor Jr. H. P.,1973. Oxygen and hydrogen isotope studies of the serpentinization of ultramafic rocks in oceanic environments and continental ophiolite complexes. American Journal of Science, Vol. 273(3), 207-239. https://doi.org/10.2475/ajs.273.3.207

Wheat G. C., Fryer P., Fisher A. T., Hulme S., Jannasch H., Mottl M., Becker K., 2008. Borehole observations of fluid flow from South Chamorro Seamount, an active serpentinite mud volcano in the Mariana forearc. Earth and Planetary Science Letters, Vol. 267(3-4), 401-409. https://doi.org/10.1016/j.epsl.2007.11.057

Wunder B., Schreyer W., 1997. Antigorite: High-pressure stability in the system MgO-SiO2-H2O (MSH). Lithos, Vol. 41(1-3), 213-227. https://doi.org/10.1016/S0024-4937(97)82013-0

Appendix

Appendix A (4.3.2 Whole Rock Geochemistry): Plotted data (Tab. 3) of serpentine muds from Asút Tesoru seamount, categorized after sites. Combined dataset of own measurements and IODP datasets (2017). Major oxides in wt. %, trace elements (Ni, Cr) in ppm. Green: U1493; blue: U1494; red: U1495; grey: U1496.

Multiple plot of MgO vs. Al_2O_3, CaO, MnO, Na_2O, SiO_2, TiO_2, FeOt, Ni, Cr
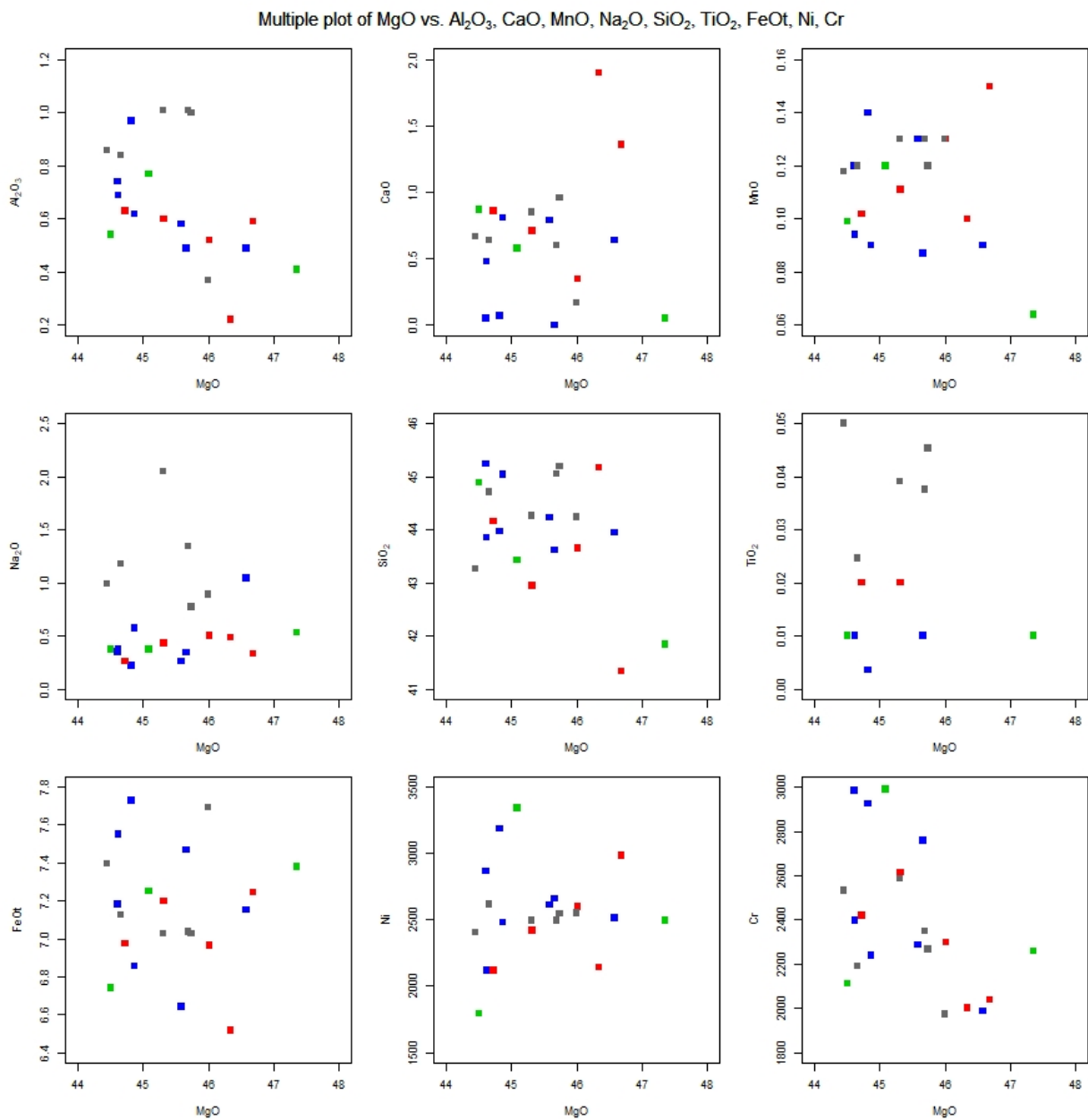
Appendix B (4.3.2 Whole Rock Geochemistry): Combined dataset (plotted Fig. 34) of serpentine muds from the Expedition 366 mud volcanoes Yinazao (formerly Blue Moon), Asút Tesoru and Fantangisna. Analyses from own measurements (in bold type) and IODP datasets (2017).

Sample	Locality	Al2O3 (wt.%)	CaO (wt.%)	Fe2O3(wt.%)	MgO (wt.%)	MnO (wt.%)	Na2O (wt.%)	SiO2 (wt.%)	TiO2 (wt.%)	K2O (wt.%)	Ni (ppm)	Cr (ppm)	V (ppm)	Sr (ppm)	Ba (ppm)	Sc (ppm)	Co (ppm)
U1492A-1H-3W	Blue Moon	0.82	0.05	7.96	45.66	0.08	0	43.69		47	2751	3426	44	4		12	134
U1492A-1H-3W-2	Blue Moon	0.32	1.3	8.16	44.43	0.06	0.84	43.27		32	1859	2345	27	278		7	49
U1492A-1H-4W	Blue Moon	0.71	0.44	7.88	44.79	0.07	0.76	42.33	0.0191	35	2709	2475	47	11		7	0
U1492A-2H-6W	Blue Moon	0.6	0.4	7.53	44.69	0.09	0.68	41.86	0.0062		2346	2384	13	15		7	95
U1492A-2H-7W	Blue Moon	0.39	0.3	7.79	44.53	0.1	0.6	42.49		22	1975	2767	27	19	1	7	100
U1492A-2H-CC	Blue Moon	0.4	0.56	7.79	43.83	0.09	0.59	42.62	0.0007	104	1956	2343	29	20		7	99
U1492A-3F-2W	Blue Moon	0.49	0.41	8.43	47.09	0.09	0.6	42.77	0.0041		2314	2756	36	323	9	8	106
U1492A-3F-3W	Blue Moon	0.68	0.62	8.08	46.38	0.1	0.56	43.34			2250	2906	48	484	7	8	101
U1492A-4F-CC	Blue Moon	0.51	0.46	8.05	46.9	0.11	0.51	43.8	0.0036		2306	2636	33	549	6	7	100
U1492A-4F-2W	Blue Moon	0.53	0.56	8	46.53	0.09	0.57	42.7	0.0071		2387	2120	24	736	3	8	108
U1492A-5F-3W	Blue Moon	0.63	0.64	8.67	46.77	0.12	0.53	43.71	0.0122		2346	2882	43	513	8	8	107
U1492A-6F-1W	Blue Moon	0.69	0.73	8.5	47	0.12	0.62	44.19	0.0106		2425	2890	40	589	9	8	109
U1492A-7F-2W	Blue Moon	0.57	0.63	7.88	47.11	0.11	0.59	44.57	0.0094		2150	2176	34	1290	20	7	97
U1492A-8F-1W	Blue Moon	0.7	0.84	7.89	45.51	0.11	0.84	42.83	0.0115		2500	2683	22	696	11	8	103
U1492A-9F-3W	Blue Moon	0.57	0.72	8.17	46.46	0.11	0.5	44.85	0.0035	17	2180	3027	30	454	4	8	103
U1492A-9F-3W-2	Blue Moon	0.72	0.85	7.88	45.92	0.11	0.47	43.68	0.0166		2419	2801	38	722	10	8	106
U1492B-1H-1W	Blue Moon	0.46	0.58	8.23	44.72	0.12	0.63	43.11		19	1977	3041	37	294	2	7	103
U1492B1H-6W	Blue Moon	0.5	0.54	8.17	48.73	0.07	0.57	43.81		31	2272	2878		18			
U1492B-1H-6W-2	Blue Moon	0.57	0.71	8.08	47.7	0.07	0.61	42.94	0.0084		2145	2605	41	26	5	8	97
U1492B-2F-1W	Blue Moon	0.55	0.61	8.19	47.61	0.1	0.52	43.65	0.0079		2356	2468	36	61	7	7	108
U1492B-2F-3W	Blue Moon	0.29	0.55	8.2	44.78	0.12	0.43	41.12		7	2118	2405	27	292	1	7	105
U1492B-3F-2W	Blue Moon	0.32	0.8	8.37	48.47	0.12	0.47	44.62		4	2473	2421	27	569	3		105
U1492B-3F-CC	Blue Moon	0.55	0.65	8.1	45.88	0.11	0.44	43.97	0.0133		2189	2624	34	323	3	7	119
U1492B-4F-1W	Blue Moon	0.54	0.64	8.07	45.91	0.11	0.54	44.03	0.0124		2314	2683		138		7	115

Sample	Name																
U1492B-4F-2W	Blue Moon	0.46	0.82	8.45	46.89	0.12	0.53	44.86	0.0083		2408	2136	32	368	4	7	116
U1492B-4F-4W	Blue Moon	0.56	0.7	8.15	46.25	0.11	0.53	44.52	0.0128		2390	2756	34	429	3	7	112
U1492B-4F-4W-2	Blue Moon	0.59	0.78	8.24	46.35	0.11	0.47	44.04	0.0108		2452	2743		446	3	8	118
U1492B-5F-2W	Blue Moon	0.58	0.81	8.52	45.99	0.12	0.46	43.72	0.0087		2258	2934	36	839	3	7	112
U1492B-5F-2W-2	Blue Moon	0.52	0.76	8.14	46.72	0.11	0.45	45.18	0.0075		2391	2531	34	328	3	7	117
U1492B-6F-2W-3	Blue Moon	0.53	0.82	8.18	46.15	0.11	0.44	44.05	0.0075		2234	2769	34	376	2	7	114
U1492B-6F-4W	Blue Moon	0.61	0.66	7.46	45.19	0.1	0.42	43.35	0.0025		2575	2518		926		8	93
U1492B-7F-4W	Blue Moon	0.56	0.59	8.54	46.79	0.12	0.46	43.64	0.0042		2473	3172	35	395	5	7	109
U1492B-8F-1W	Blue Moon	0.57	0.75	8.06	45.95	0.11	0.45	44.48	0.0139		2574	2344	35	513	3	8	111
U1492B-9F-3W	Blue Moon	0.34	0.72	7.96	45.58	0.11	0.38	43.71		4	2110	2421		213	1	7	101
U1492B-10F-2W	Blue Moon	0.58	0.81	8.18	46.74	0.11	0.5	44.36	0.0075		2293	2741	34	211	4	8	118
U1492B-10F-3W	Blue Moon	0.55	0.97	8.11	46.16	0.11	0.46	44.45	0.0072		2326	2473	34	562	9	7	116
U1492B-12F-1W	Blue Moon	0.53	0.7	8.23	46.37	0.11	0.51	44.33	0.0148		2492	2301	32	711	5	7	112
U1492B-13F-CC	Blue Moon	0.61	1.22	8.07	46.45	0.11	0.47	44.79	0.0157		2297	2444	35	242	6	7	118
U1492B13F-2W	Blue Moon	0.59	2.05	7.62	44.87	0.11	0.43	42.21	0.0078		2162	2553	33	327	3	7	119
U1492C-1H-2W	Blue Moon	0.62	1.45	8.33	45.74	0.09	0.89	44.87	0.0156		2546	2533	36	32		8	110
U1492C-3F-1W	Blue Moon	0.52	0.79	8.14	45.77	0.11	0.67	43.76	0.0094		2324	2285	34		20	7	115
U1492C-3F-2W	Blue Moon	0.4	1.58	7.91	47.45	0.11	0.7	42.35		14	2320	2693	28	659	7		99
U1492C-4F-2W	Blue Moon	0.66	1.12	7.99	45.93	0.11	0.61	43.75	0.0194		2308	2376	35	564	7	7	119
U1492C-4F-3W	Blue Moon	0.58	1.51	7.79	44.45	0.1	0.59	40.75			2221	2383	35	434	6	7	111
U1492C-5F-2W	Blue Moon	0.55	1.48	8.21	46.28	0.11	0.69	44.08	0.0127		2459	2272	34	984	15	7	116
U1492C-5F-2W-2	Blue Moon	0.63	1.99	8.13	45.67	0.14	0.76	42.8			2546	2457	35	812	13	8	109
U1492C-6F-2W	Blue Moon	0.54	2.51	7.8	41.07	0.1	0.48	41.63	0.0019		2080	2213		827	11		
U1492C-6F-3W	Blue Moon	0.66	1.9	8.26	40.6	0.1	0.52	41.55	0.0052		2286	2858		434		7	
U1492C-8F-3W	Blue Moon	0.5	1.08	7.9	44.22	0.1	0.56	42.6	0.0012		2161	2239		1123			
U1492C-8F-3W-2	Blue Moon	0.65	2.65	7.54	41.13	0.1	0.48	40.39	0.0182		2012	2500		395			
U1492C-10X-CC	Blue Moon	0.55	1.39	8.01	42.85	0.1	0.77	42.97	0.0003		2385	2126		420	5		
U1492C-11F-2W	Blue Moon	0.59	0.76	8.14	44.14	0.1	0.53	44.24	0.0028		2637	2352		259		7	
U1492C-11F-3W	Blue Moon	0.39	1.03	7.93	45.41	0.1	0.54	42.98		6	2041	2199	29	372	4	7	101
U1492C-12F-1W	Blue Moon	0.38	0.68	8.17	43.41	0.23	0.59	43.87		9	1955	2304	29	244	2	7	102
U1492C-13F-2W	Blue Moon	0.48	0.87	7.89	47.31	0.1	0.55	44.35	0.0038	0.02	2313	2452	30	303	2		98

Sample	Name																
U1492C-14F-3W	Blue Moon	0.23	0.55	9.05	44.22	0.14	0.43	41.53		59	3302	1934	26	592	4	7	120
U1492C-15F-1W	Blue Moon	0.53	0.75	8.03	42.45	0.11	0.99	41.51			2052	2680		481		7	
U1492C-16F-1W	Blue Moon	0.57	0.85	8.39	45.03	0.12	0.95	43.68	0.0004		2413	2447		370		7	
U1492C-17F-CC	Blue Moon	0.6	0.59	8.2	43.88	0.11	0.44	44.11	0.0027		2330	2568		394		7	
U1492C-18F-1W	Blue Moon	0.8	0.67	8.58	44.25	0.12	0.5	44.48			2380	2872		365		9	
U1492C-19F-1W	Blue Moon	0.61	0.88	9.36	46.59	0.13	0.56	41.22		136	2144	2666	32	582	6	7	106
U1492C-20F-1W	Blue Moon	0.49	0.77	8.05	43.3	0.1	0.52	41.69			1916	2560	29	42		7	104
U1492C-21F-2W	Blue Moon	0.3	0.65	7.72	47.49	0.1	0.61	44.4		27	2280	2541		102	2		107
U1492C-22F-2W	Blue Moon	0.55	0.63	8.18	44.11	0.12	0.51	44.35			2519	2200		216		7	
U1492C-23F-1W	Blue Moon	0.62	0.67	8.26	45.41	0.11	0.65	45.12	0.0001		3027	2446		848	10	7	
U1492C-24F-1W	Blue Moon	0.44	0.6	8.01	43.22	0.11	0.56	43.75		16	1943	2783	29	451		7	102
U1492C-26F-1W	Blue Moon	0.51	1.17	7.98	44.64	0.11	0.89	42.76	0.0024		2000	2745	27	113	15	8	103
U1492C-29X-CC	Blue Moon	0.42	0.81	7.34	43.47	0.11	0.36	43.6		19	2032	2394	28	29		7	100
U1492C-30X-CC	Blue Moon	0.46	0.58	7.86	45.44	0.11	0.5	43.52	0.0007	112	2169	2557	30	27	2	7	100
1493B-5F-3W	Asut Tesoru	0.77	0.58	8.06	45.09	0.12	0.37	43.43		18	3341	2990			1	8	125
1493B-9X-1W	Asut Tesoru	0.76	0.06	9.93	47.48	0.2	0.02	37.77		9	3081	3120	34			7	115
1494A-2F-1W	Asut Tesoru	0.49	0.64	7.95	46.58	0.09	1.04	43.94		32	2515	1987					
1494A-3F-2W	Asut Tesoru	0.62	0.81	7.62	44.87	0.09	0.57	45.04		0.02	2481	2238					
1494A-6F-2W	Asut Tesoru	0.58	0.79	7.38	45.59	0.13	0.26	44.23		5	2611	2285					
1494A-9G-CC	Asut Tesoru	0.74	0.05	7.98	44.61	0.12	0.35	45.24		11	2867	2984	36				
1494A-10F-2W	Asut Tesoru	0.97	0.07	8.59	44.82	0.14	0.22	43.97	0.0035	0.01	3186	2925	43				
1495B-2F-1W	Asut Tesoru	0.22	1.9	7.24	46.34	0.1	0.48	45.16			2141	2002					
1495B-2F-3W	Asut Tesoru	0.59	1.36	8.05	46.69	0.15	0.33	41.33		9	2982	2037					
1495B-4F-3W	Asut Tesoru	0.52	0.35	7.74	46.02	0.13	0.5	43.65		17	2599	2298	23				
1496A-2F-4W	Asut Tesoru	0.84	0.64	7.92	44.66	0.12	1.18	44.71	0.0246	38	2614	2189	25				
1496A-4F-1W	Asut Tesoru	1.01	0.6	7.82	45.69	0.13	1.34	45.05	0.0375	48	2496	2348	27				
1496A-6F-2W	Asut Tesoru	1.33	0.7	8.43	45.96	0.14	1.33	43.61		77	2751	2417	32				
1496A-6F-5W	Asut Tesoru	0.37	0.17	8.55	46	0.13	0.89	44.24		39	2548	1972					
1496A-7F-4W	Asut Tesoru	1	0.96	7.81	45.74	0.12	0.77	45.19	0.0453	33	2543	2266					
1496A-103	Asut Tesoru	0.86	0.67	8.22	44.45	0.118	0.99	43.26	0.05	0.04	2405	2531	26				
1495B-95	Asut Tesoru	0.60	0.71	8.00	45.32	0.111	0.43	42.94	0.02	0.02	2419	2614	27				

1495B-89	Asut Tesoru	0.63	0.86	7.75	44.72	0.102	0.26	44.15	0.02	0.01	2118	2420	28				
1494A-81	Asut Tesoru	0.49	0.00	8.30	45.66	0.087	0.34	43.61	0.01	0.01	2661	2759	27				
1494A-79	Asut Tesoru	0.69	0.48	8.39	44.62	0.094	0.38	43.85	0.01	0.02	2116	2397	27				
1493B-63	Asut Tesoru	0.54	0.87	7.49	44.50	0.099	0.37	44.89	0.01	0.02	1791	2111	<20				
1493B-61	Asut Tesoru	0.41	0.05	8.20	47.36	0.064	0.53	41.84	0.01	0.02	2492	2257	23				
U1497A-5F-3W	Fantangisna	1.15	1.27	7.99	44.24	0.11	0.28	44.38		13	2448	2804	37	11	1	9	102
U1497A-6F-1W	Fantangisna	0.65	0.14	8.8	45.26	0.1	0.3	46.18		12	2895	2581	30	22		8	126
U1497B-3F-1W	Fantangisna	0.45	0.89	7.77	46.28	0.1	0.62	42.81		26	2321	2377		13	4	5	99